UNIVERSITY OF CAPE TOWN
IYUNIVESITHI YASEKAPA • UNIVERSITEIT VAN KAAPSTAD

Numerical Modelling of Hydrodynamics, Gas Dispersion and Mass Transfer in an Autoclave

by

Harish Appa

Thesis Presented for the Degree of

DOCTOR OF PHILOSOPHY

in the Department of Chemical Engineering

UNIVERSITY OF CAPE TOWN

September 2012

minerals to metals
DEPARTMENT OF CHEMICAL ENGINEERING

Centre for Minerals Research

Acknowledgements

I would like to thank my supervisors, Prof. D.A. Deglon and Prof. C.J. Meyer for giving me the opportunity to do a PhD at UCT and for their support, guidance as well as patience over the years.

The support and help of Prof. Jean-Paul Franzidis is sincerely acknowledged.

The funding and support from the Minerals to Metals Initiative (MtM), Centre for Minerals Research (CMR), Centre for Research in Computational and Applied Mechanics (CERECAM), the NRF through the SARChI Chair in Minerals Beneficiation as well as Anglo American Platinum are gratefully acknowledged.

Thank you to Mr. Joachim Macke, Mr. Peter Dobias and Mr. Bill Randall for their assistance in the construction of the experimental autoclave rig.

The help of Mr. Graham Inggs dealing with all the software and computer hardware issues is acknowledged.

I would also like to thank Pam Messina of Impressive Design for facilitating the making of the perspex autoclave vessel.

I am grateful to Kimleigh Chemicals SA (PTY) Ltd for providing the copper sulphate used for the experimental work.

The help of Mr. Eugene Christiaan Joubert with the PIV facility at the University of Stellenbosch is sincerely acknowledged.

Thank you to the staff in the Department of Mechanical and Chemical Engineering at UCT for their valuable assistance.

I would also like to thank all my colleagues for their help over the last few years.

I would like to express my gratitude to my friends Jean-Paul, Vanessa, Case, Aashika, Neelan and Traci for their support and critical advice.

A special thanks to my parents and my sister for their encouragement and moral support over the years.

I thank Lord Ganesh for leading me to the completion of this work.

Publications

Journal Publications

Appa, H., Deglon, D., Meyer, C., (2012), Numerical modelling of hydrodynamics and gas dispersion in an autoclave. Hydrometallurgy. (Accepted for publication)

Appa, H., Deglon, D., Meyer, C., (2012), Numerical modelling of mass transfer in an autoclave. Hydrometallurgy. (Submitted for publication)

Conference Presentations and Journal Publications

Appa, H., Deglon, D., Meyer, C., (2011), Numerical modelling of an autoclave, 8^{th} International Conference on Computational Fluid Dynamics in the Oil & Gas, Metallurgical and Process Industries, SINTEF/NTNU, Trondheim, Norway.

Appa, H., Deglon, D., Meyer, C., (2010), The numerical modelling of hydrodynamics, gas dispersion and mass transfer in an autoclave, Mineral Processing 2010, Cape Town, South Africa.

Appa, H., Deglon, D., Meyer, C., (2011), The numerical modelling of an industrial autoclave, Mineral Processing 2011, Cape Town, South Africa.

I hereby certify that the work embodied in this thesis is the result of original research and has not been submitted for another degree at any other university or institution.

Harish Appa
September 2012

Abstract

Introduction: Autoclaves are widely used in the mining industry, particularly in the leaching circuit for extraction of base metals such as nickel and copper. The kinetics for the reactions can be controlled by gas-liquid mass transfer, k_La, which is highly influenced by hydrodynamics and gas dispersion. Gas-liquid mass transfer is commonly determined from empirical correlations based on power requirement and volume of the vessel as well as superficial gas velocity. However, these correlations are sensitive to the geometry of both vessel and impeller as well as operating conditions. Even though, these correlations can be used to estimate k_La, they do not provide information about local mass transfer, such as, how it is distributed in the vessel.

Computational Fluid Dynamics (CFD), a numerical tool, provides the means to predict fluid phenomena in greater detail. Both local and global information about the fluid flow can be obtained using CFD. There have been numerous studies on leaching and leach chemistry in autoclaves. However, only a few have used CFD to predict hydrodynamics in autoclaves and to the author's knowledge there have been no published work on the numerical modelling of gas dispersion and mass transfer in autoclaves. Even though CFD provides the tool to predict different flow phenomena, the models have to be validated to provide a degree of confidence in the predictions. To this end, the objective of this thesis is to use CFD models, validated against experimental data to predict hydrodynamics, gas dispersion and mass transfer in an autoclave. The models will be able to provide a better understanding of the different flow phenomena and illustrate key features in the autoclave. Furthermore, the models will show the effect of operating conditions on hydrodynamics, gas dispersion and mass transfer. These predictions will provide the basis to develop better and more accurate models to analyse full scale autoclaves.

Experimental: A 60 l pilot-scale vessel based on the first compartment of an 80 m^3 Sherritt Gordon horizontal autoclave was used for this study. The first compartment was geometrically scaled down and had a capacity of 60 l. Hydrodynamics was characterised in terms of velocity flow field as well as power. PIV measurements were conducted to determine the velocity flow field and power draw was determined from a load cell, which measured the torque experienced by the motor. Gas dispersion was characterised in terms of bubble size, which was measured using the Anglo American Platinum bubble sizer. Mass transfer measurements were made to determine k_La using a dissolved oxygen probe. An experimental programme was designed, such that the study was carried out over a range of

impeller speeds (varying between 150 and 395 rpm), at two gas flow-rates (4.37 and 7.8 $lmin^{-1}$) and three temperatures (25, 50 and 70°C). In addition to water and in order to mimic the fluid in an industrial autoclave a synthetic leach liquor composed of sulphuric acid, nickel and copper was used.

Numerical: The geometry of the CFD model was based on the pilot-scale vessel and a full 3-D model was used. Initially a single phase model was developed. For this model agitation was simulated with both Multiple Reference Frames (MRF) and sliding mesh models. The MRF model was used to start-up the calculations and the sliding mesh model to complete the simulation. The turbulent flow regime was simulated with the standard k-ε model.

The gas-liquid system was simulated with the Euler-Euler model and the discrete method was used to solve for the population balance equations. Agitation was simulated using a similar method as the single phase simulations. The dispersed k-ε model was used to simulate the turbulent flow.

Gas-liquid mass transfer coefficient, k_La was simulated by separately determining a, which was obtained from the population balance model and k_L, calculated using variants of the penetration model.

Hydrodynamics: Hydrodynamics showed that the power and velocity flow field was well-predicted with the standard k-ε turbulence model and the sliding mesh model. The simulation was also able to reproduce an atypical flow at the impeller discharge region. The horizontal jet leaving the impeller, which is normally observed in stirred tanks with a radial impeller is not reproduced. The flow in the impeller stream was found to have a downward inflection. The global flow field is asymmetrical as a result of the geometry of the vessel and impeller. The double-loop structure, one below and one above the impeller, changes to a more or less single-loop structure, with the disappearance of the lower recirculation loop, at high impeller speeds.

Gas dispersion: Gas dispersion results showed that the gas-liquid system was well predicted with the Euler-Euler model coupled with the discrete method, which was used to solve for the population balance model equations. Gas distribution predicted was found to be poor primarily due to the flow pattern. Most of the gas was trapped below the impeller as well as in the recirculation loops. There were large regions of the vessel with practically no gas. The overall gas hold-up was low, below 1%, because of the low superficial gas velocities used. The local bubble size was heterogeneously distributed, with smaller bubbles

close to the impeller and larger bubbles in the rest of the vessel. The variation in bubble size with impeller speed was small and the system was found to be mainly controlled by coalescence. Changes in fluid properties had a small effect on bubble size, decreasing in a synthetic leach liquor.

Mass transfer: The results showed that the gas-liquid mass transfer coefficient, k_La, was accurately predicted with a bubble size distribution and the eddy cell model. The mass transfer distribution in the vessel was qualitatively poor, with large regions of practically no mass transfer. k_La was highest in the impeller region. k_La increased with impeller speed, gas flow-rate and temperature. The difference in k_La values between water and the synthetic leach liquor was marginal. Furthermore, a correlation, based on the pilot-scale autoclave, was developed to estimate k_La. The correlation comprised of an additional parameter to account for the difference in temperature.

Conclusion: The research study, predicted fundamental fluid flows in a pilot-scale autoclave accurately, showing both expected and unexpected features. It also provided a better understanding of various hydrodynamics, gas dispersion and mass transfer features. The findings and the model developed can be used as a basis to develop more detailed models to predict the flow phenomena in full scale autoclaves.

Contents

List of Figures

List of Tables

Nomenclature

Symbols

$\overline{u}_i$	Averaged velocity components (ms^{-1})
$\vec{a}$	Acceleration (ms^{-2})
$\vec{F}_q$	External body force (N)
$\vec{F}_{lift,q}$	Lift force (N)
$\vec{R}_{pq}$	Interaction force between phase p and q (N)
$\vec{v}_{pq}$	Interphase velocity (ms^{-1})
a	Superficial area per unit volume (m^{-1})
B_l	Lever Arm (m)
B_r	Birth rate ($m^{-3}s^{-1}$)
C	Concentration (kgm^{-3}) or model parameter (-)
C^*	Saturation concentration (kgm^{-3})
C_D	Drag coefficient (-)
D_c	Vessel inner diameter (m)
D_l	Diffusivity of gas in liquid (m^2s^{-1})
d_p	Diameter of bubble of phase p (m)
D_r	Death rate ($m^{-3}s^{-1}$)
d_{32}	Sauter mean diameter (m)
F	Force (N)
F	Model constant (-)
f	Drag function (-)
g	Gravitational acceleration (ms^{-2})
$G_{k,q}$	Production of turbulent kinetic energy ($kgm^{-1}s^{-3}$)
I	Unit tensor (-)
J	Mass transfer flux ($molm^2s^{-1}$)
k	Turbulent kinetic energy per unit mass (Jkg^{-1})
k_L	Mass transfer coefficient (ms^{-1})
K_{pq}	Inter-phase momentum coefficient ($kgm^{-3}s^{-1}$)
k_q	Turbulent kinematic viscosity (m^2s^{-1})
m	Mass (kg)
N	Stirrer speed (s^{-1})
n	Drop size (m) or number density (m^{-3})
p	Pressure (Pa)
P_g	Gassed power consumption (W)

R_A	Radius of solute (m)
Re	Reynolds number (-)
t	Time (s)
U	Superficial gas velocity (ms^{-1})
u_i'	Fluctuating velocity components (ms^{-1})
u_i	Velocity components (ms^{-1})
V	Volume (m^3)
T	Temperature (K)

Greek Letters

α	Volume fraction (-)
δ	Film thickness (m)
λ	Bulk viscosity ($kgm^{-1}s^{-1}$)
μ	Viscosity ($kgm^{-1}s^{-1}$)
ω	Angular velocity ($rads^{-1}$)
$\overline{\overline{\tau}}$	Stress tensor ($kgm^{-1}s^{-2}$)
$\overline{\tau}_w$	Average wall shear stress (Pa)
ϕ	Gas hold-up (-)
ρ	Density (kgm^{-3})
τ_e	Exposure time (s)
τ_p	Particulate relaxation time (s)
θ	Exposure time (s)
ε	Turbulent energy dissipation rate (m^2s^{-3})

Subscripts

dr	Drift
G	Gas
L	Liquid
p	Phase p
t	Turbulent

Acronyms

AAPBS	Anglo American Platinum Bubble Sizer
AAS	Atomic Absorption Spectroscopy
BDM	Bubble Density Model
BMR	Base Metal Refinery
BSD	Bubble Size distribution
CFD	Computational Fluid Dynamics
CSP	Capillary Suction Probe

DI	Digital Imaging
DO	Dissolved Oxygen
DPB	Discritised Population Balance
DPM	Dynamic Pressure-step Method
GOM	Gassing-Out Dynamic Method
LDA	Laser Doppler Anemometry
LDV	Laser Doppler Velocimetry
LES	Large Eddy Simulation
MRF	Multi-Reference Frames
MUSIGs	Multi Size Groups
NCM	Nickel Copper Matte
PBM	Population Balance Model
PD	Product-Difference
PDA	Phase Doppler Anemometry
PDE	Partial Differential Equation
PIV	Particle Image Velocimetry
PSD	Particle Size Distribution
QMOM	Quadrature Methods of Moments
QUICK	Quadratic Upstream Interpolation for Convective kinetics
RANS	Reynolds Averaged Navier-Stokes
RMBR	Rustenberg Base Metal Refiners
RNG	Renormalization Group
SLL	Synthetic Leach Liquor
SM	Sliding Mesh
SMM	Standard Method of Moments
SOM	Sulphite Oxidation Method
UDF	User Defined Function

1 Introduction

1.1 Overview

Autoclaves are pressure vessels which are operated at elevated temperatures and pressures. They are in the form of cylinders and usually have end caps in a hemispherical shape. With the harsh operating conditions the wall of the vessel experiences high stresses. The geometry of the vessel provides the strength required to support those conditions. There is a wide range of applications for autoclaves; for example they are used for polymerisation of composite materials for the aeronautical industry, vulcanisation of rubber and for pressure leaching in the mining industry.

Autoclaves are used in the leaching circuit in the mining industry (Nicolle et al., 2009; Roux et al., 2009). The leaching process entails the removal of metallic species and non-metallic species by dissolving them away from solids in an aqueous solution. This requires operating conditions with a high pressure and temperature in an acidic environment. The ability to withstand those conditions makes autoclaves suitable vessels for this process. One common application is leaching of Nickel-Copper Matte (NCM) on Base Metal Refineries (BMR) in the Platinum Group Metal (PGM) industry.

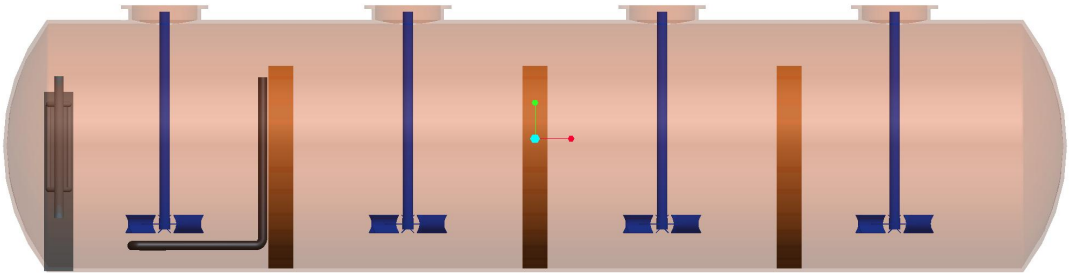

Figure 1.1: Typical industrial autoclave

There are three stages in the BMR process; copper removal, primary leach and secondary leach. Autoclaves are used in the last two stages. Figure 1.1 shows the front view of a Sherritt Gordon horizontal autoclave used in the acid leach process. The vessel is divided into four compartments by vertical weir walls. Each compartment is agitated by an impeller and has two baffles, one on each side of the vessel. The feed into the autoclave depends on the leaching stage; primary or secondary. For the latter, the feed is comprised of a primary leach residue, copper spent and plant spillages. Oxygen is also fed into the

compartments for oxidation of metals and to remove excess heat from highly exothermic reactions. The reactor is operated at a pressure and a temperature that are maintained at 1000 kPa and 140-145°C respectively.

There are various chemical reactions that occur in the leaching stage and gas-liquid mass transfer can be a rate-limiting factor (Crundwell, 1995; Tatterson, 1991; Jakobsen, 2008). For this reason gas-liquid mass transfer has been one of the many factors used to optimise the design and operations of autoclaves. Empirical mass transfer correlations are usually used in the design of the vessels and their optimisation. However, these correlations are known to be strongly dependent on geometry of the reactor, type of impeller and operating conditions. This is mainly because of their impact on hydrodynamics and gas dispersion, which consequently control mass transfer in the system.

Hydrodynamics in mixing vessels is quite complex where both micro and macro phenomena are affected by geometry of the vessel and operating conditions. Based on numerical and experimental research studies on stirred tanks, which mainly focused on flow patterns, velocity flow field, turbulent parameters, it can be seen that the hydrodynamic characteristics of mixing reactors are important. For example, the flow pattern in a baffled cylindrical vessel with a radial impeller, such as a Rushton turbine produces two recirculation loops, one below and one above the impeller. The absence of baffles and position of the impeller can lead to formation of surface vortex. Close to the impeller, velocity and turbulent kinetic energy are higher and dissipate in the regions away from the impeller. These are important to understand as they affect gas dispersion.

The motion of bubbles in a mixing vessel is dominated by the flow pattern of the liquid phase. The gas distribution in stirred tanks is non-homogeneous, with high accumulation in the recirculation loops and close to the impeller tip. The spatial bubble size distribution depends on a complex interaction between gas hold-up, local turbulence and local bubble size.

Mass transfer in turn is highly influenced by the inherent hydrodynamics and gas dispersion. In mixing vessels, the gas-liquid mass transfer coefficient, k_La, is high close to the impeller and in the recirculation loops. That is, higher in regions where the bubble size is small and/or gas hold-up is high.

Therefore, is it important to understand the various phenomena. Computational Fluid Dynamics (CFD), a powerful tool to numerically model fluid flows, can be used to investigate the above-mentioned phenomena. It provides detailed information, which cannot

always be obtained by experimental means, to better understand fluid flows. This technique has been widely used to model stirred tanks. However, due to the complexity of the fluid flow in mixing vessels there is still ongoing research work, even experimental studies to validate the CFD models, to enhance predictions.

1.2 Objectives

Understanding mass transfer in autoclaves is important. It can be rate limiting in the various chemical reactions occurring in the vessel and a thorough understanding of the underlying hydrodynamics and gas dispersion is also required as they both control mass transfer. So far, mass transfer has been estimated using power law correlations, which are known to be dependent on the geometry of the vessel as well as operating conditions. There have also been a variety of studies on leaching and leach chemistry in autoclaves (Georgiou and Papangelakis, 2004; Lamya, 2007). However, few studies have focused on investigating the three phenomena in autoclaves and even fewer have developed computational models. Therefore, the aim of the project was to develop a CFD model, validated against experimental data, to predict hydrodynamics, gas dispersion and mass transfer in a pilot-scale autoclave. The latter was based on the first compartment of an 80 m^3 Sherritt Gordon horizontal autoclave. Figure 1.2 shows the pilot-scale autoclave used for this study.

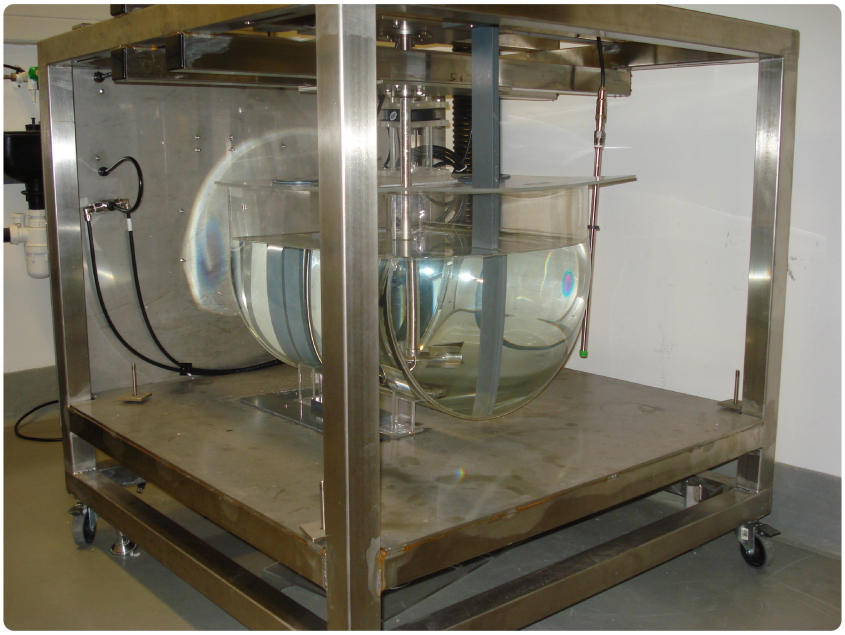

Figure 1.2: Autoclave experimental rig

1.3 Scope of Thesis

The first phase of the research focused on the development of a single phase CFD model, for which water was used. The single phase models were validated with experimental data, in terms of power draw and velocity field. Then, two different gas-liquid systems were investigated; water and synthetic leach liquor. Both were sparged with oxygen gas. The composition of the synthetic leach liquor was based on the solution used at the RMBR plant. Gas-liquid systems were investigated over a range of operating conditions and this is further discussed in Chapter 3. However, due to the complexity of the multiphase system, the liquid phase was modelled as a single phase 'pseudo-liquid'. The numerical predictions for the gas-liquid systems were validated in terms of experimentally determined power input and gas-liquid mass transfer data. The influence of agitation, gas flow-rate and fluid properties on the volumetric mass transfer coefficient were also investigated.

1.4 Structure of Thesis

The thesis begins with a review of published research work which is presented in Chapter 2. Chapter 3 describes the experimental programme and experimental techniques used. This is followed by Chapter 4 where the numerical approach used to model the single phase and multiphase system is discussed. The results and discussion are presented in Chapter 5. The conclusions drawn and recommendations for future work are reported in Chapter 6.

2 Literature Review

A review of numerical and experimental techniques used to model various flow phenomena in mixing vessels are presented in this chapter. The latter is divided into five main sections; leaching in autoclaves, numerical modelling of fluid flow, hydrodynamics, gas dispersion, mass transfer and summary. The first two sections give an overview of leaching in autoclaves and numerical techniques used to model fluid flow in mixing vessels. The hydrodynamics, gas dispersion and mass transfer sections are presented in Sections 2.3, 2.4 and 2.5 respectively. Each section covers the theory describing the respective phenomenon and numerical as well as experimental techniques used for their investigation. Finally a summary of the literature review is presented in Section 2.6.

2.1 Leaching in Autoclaves

2.1.1 Autoclaves

An autoclave generally is a pressure vessel that operates at high temperature and pressure. The autoclave is widely used in the leaching stage of the hydrometallurgical process. Figure 2.1 shows a horizontal acid leach autoclave with six compartments.

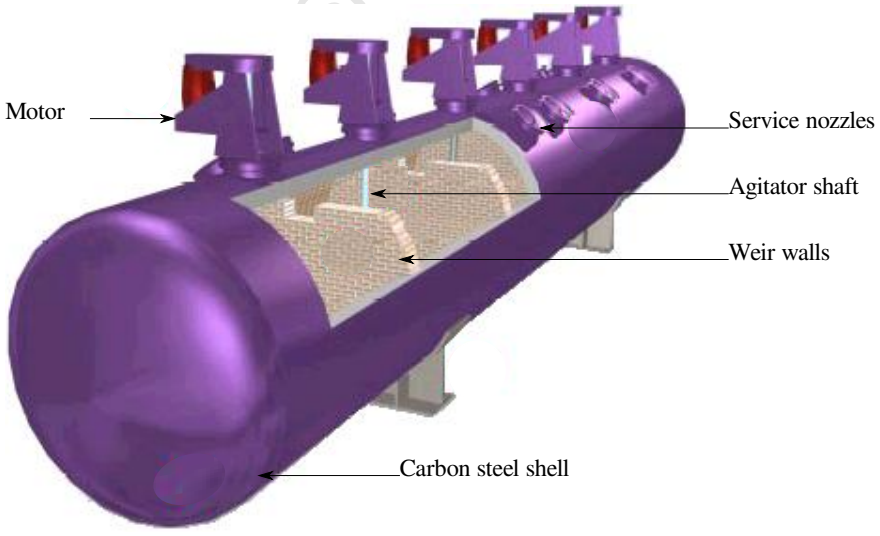

Figure 2.1: Schematic of a horizontal acid leach autoclave (METSOC, 2011)

The cylindrical shape of the autoclave is mainly to withstand the harsh operating conditions experienced by the vessel. The latter also has a carbon steel shell and is brick lined to withstand a highly acidic environment. The vessel is normally divided into compartments,

varying mostly between four and six, by weir walls. The system is agitated by an impeller in each compartment which is powered by a motor via an agitator shaft. The vessels are also equipped with service nozzles found on the side.

2.1.2 Nickel Copper Matte

Autoclaves are used in two main stages on the Base Metal Refinery plant; in the primary and secondary leaching circuit. The primary leach is to ensure maximum nickel extraction, normally greater than 75%. The main objectives of secondary leach are to complete extraction of nickel (>99%) and copper (>97%) from the Nickel Copper Matte (NCM) (Petersen, 2007). The primary leach residue, copper spent and plant spillages are mixed to form the feed for the secondary leach. Each compartment is agitated and sparged with oxygen gas. The system is operated at a pressure of 1000 kPa and temperature varying between 140 and 145°C. There are two leaching periods, slurry mixing and oxidation of the leach. These are explained by equations 2.1 to 2.7. All metals in the form of re-precipitated hydroxides or basic sulphates dissolve the copper, by reactions 2.1, and iron or nickel where present (Petersen, 2007). During the oxidation phase, covellite is oxidised (2.3) or decomposed to elemental sulphur. The reaction for copper and iron are given by equations 2.6-2.7.

During a slurry mixing phase sulphates rapidly dissolve, consuming acid.

$$Cu_3(OH)_4SO_4 + 4H^+ \rightarrow 3Cu^{2+} + SO_4^{2-} + 4H_2O \quad (2.1)$$

$$Ni_3(OH)_4SO_4 + 4H^+ \rightarrow 3Ni^{2+} + SO_4^{2-} + 4H_2O \quad (2.2)$$

During an oxidation phase the major copper reactions are:

$$Cu_9S_5 + 8H^+ + 2O_2 \rightarrow 5CuS + 4Cu^{2+} + 4H_2O \quad (2.3)$$

$$CuS + 2O_2 \rightarrow Cu^{2+} + SO_4^{2-} \quad (2.4)$$

Nickel reaction is:

$$Ni_3S_4 + 7.5O_2 + H_2O \rightarrow 3Ni^{2+} + 4SO_4^{2-} + 2H^+ \quad (2.5)$$

The high temperature oxidised environment leads to a precipitation of iron:

$$3Fe^{3+} + Na^+ + 2SO_4^{2-} + 6H_2O \rightarrow Na[FE_3(OH)_6(SO)_4)_2] + 6H^+(\uparrow \text{acid}, \downarrow \text{T}) \quad (2.6)$$

$$2Fe^{3+} + 3H_2O \rightarrow 4Fe_2O_3 + 6H^+(\downarrow \text{acid}, \uparrow \text{T}) \quad (2.7)$$

The chemical reactions are governed by the operating conditions. Often the reactions can be broken down into a number of steps and the overall rate of the reaction can be determined by the speed of the different reaction steps. The slowest step in a multi-step

reaction controls the overall rate of reaction and is referred to as the rate-determining step. In hydrometallurgy where oxygen gas, which is poorly soluble in water, is commonly used; gas-liquid mass transfer can be a rate limiting step. Thus, besides the effect of operating conditions, an understanding of gas-liquid mass transfer is also crucial.

2.2 Numerical Modelling of Fluid Flow

The commercial code ANSYS Fluent 13 (ANSYS, 2010) was used for this research work. The code uses a finite volume method to solve the governing equations. This section starts with an overview of the finite volume method, covering governing equations as well as the turbulence models and discretisation schemes used for the numerical modelling of mixing vessels. Then, a description of multiphase models and population balance models used to simulate gas-liquid systems are presented. This is followed by a review of previous research works.

2.2.1 Finite Volume Method

2.2.1.1 Governing equations

The governing equations of fluid flow represent mathematical statements of the conservation laws of physics (Versteeg and Malalasekera, 1995). The conservation equations are given by equations for mass (continuity) and momentum (Navier-Stokes). These are time-averaged to yield Reynolds averaged Navier-Stokes equations. The equations of motion are timed-averaged for a turbulent flow. The energy equation is solved for flows involving heat transfer or compressibility.

Continuity equation

The equation for conservation of mass, or continuity, is given by:

$$\frac{\partial \rho}{\partial t} + \nabla \cdot (\rho \vec{v}) = S_m \tag{2.8}$$

where S_m is the mass added to the continuous phase from the dispersed second phase and any user-defined sources

Navier-Stokes equation

The Navier-Stokes equations, which describe the conservation of momentum, are given by:

$$\frac{\partial (\rho \vec{v})}{\partial t} + \nabla \cdot (\rho \vec{v} \vec{v}) = -\nabla p + \nabla \cdot \left(\overline{\overline{\tau}}\right) + \rho \vec{g} + \vec{F} \tag{2.9}$$

where p is the static pressure

$\overline{\overline{\tau}}$ is the stress tensor
$\rho\vec{g}$ is the gravitational body force
$\vec{F}$ are the external body forces

It relates the sum of a convective acceleration and a local acceleration to the sum of the pressure gradient, a viscosity term and a term for external body forces.

The stress tensor is given by

$$\overline{\overline{\tau}} = \mu\left[\left(\nabla\vec{v} + \nabla\vec{v}^T\right) - \frac{2}{3}\nabla\cdot\vec{v}I\right] \tag{2.10}$$

where μ is the molecular viscosity
I is a unit tensor

Time averaging
This method decomposes solution variables in the form of instantaneous (exact) Navier-Stokes equations into the mean (time-averaged) and fluctuating components.

Thus, the velocity components are given by:

$$u_i = \overline{u}_i + u_i' \tag{2.11}$$

where $\overline{u}_i$ and u_i' are the mean and fluctuating components (i = 1,2,3).

Similar equations are used for other scalar quantities such as pressure, energy, species concentration. The time averaged equations are substituted into the instantaneous continuity and the momentum equations yields:

$$\frac{\partial\rho}{\partial t} + \frac{\partial}{\partial x_i}\left(\rho\overline{u}_i\right) = 0 \tag{2.12}$$

and

$$\frac{\partial\left(\rho\overline{u_i}\right)}{\partial t} + \frac{\partial\left(\rho\overline{u_i u_j}\right)}{\partial x_j} = -\frac{\partial p}{\partial x_i} + \frac{\partial}{\partial x_j}\left[\mu\left(\frac{\partial\overline{u_i}}{\partial x_j} + \frac{\partial\overline{u_j}}{\partial x_i} - \frac{2}{3}\delta_{ij}\frac{\partial\overline{u_l}}{\partial x_l}\right)\right] + \frac{\partial}{\partial x_j}\left(-\rho\overline{u_i'u_j'}\right) \tag{2.13}$$

Equation 2.12 and 2.13 are known as the Reynolds-averaged Navier-Stokes (RANS) equations. Additional terms,$-\rho\overline{u_i'u_j'}$, known as the Reynolds stresses now appear in Equation 2.13. These must be modelled to close the RANS equations.

2.2.1.2 Discretisation schemes

Equations of motion do not have analytical solutions and have to be solved numerically by discretising the problem domain. Discretisation is a process by which a closed-form

mathematical expression is approximated to a system of algebraic expressions. The accuracy and ability to physically model a system is partly dictated by the discretisation scheme and has three fundamental properties; conservativeness, boundedness and transportiveness (Versteeg and Malalasekera, 1995). They also ensure stability of flow regimes. The accuracy of a numerical solution depends on how close discretised equations represent PDE's (Ranade et al., 1989). Some of the commonly used schemes are briefly discussed below.

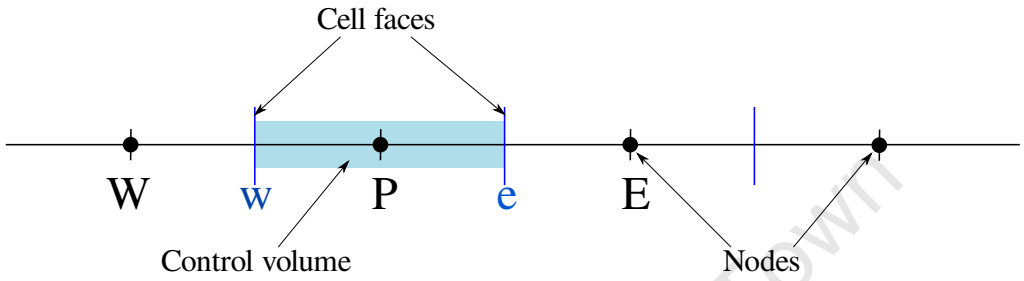

Figure 2.2: One-dimensional domain

Before discretisation the first step in the finite volume method is grid generation. Figure 2.2 shows a one-dimensional domain divided into control volumes. Each node is surrounded by a control volume or cell, as shown in Figure 2.2 with node P. The faces of control volumes are placed mid-way between adjacent nodes.

The central differencing scheme linearly interpolates the transported variable between adjacent nodes to compute a cell face value. This method does not take flow directionality into consideration and thus is only stable for diffusion-dominated low Reynolds number flows or if the mesh is fine. This inadequacy is treated in the upwind differencing scheme, where convected value at a cell face is set to be equal to the value at an upstream node. However, if the flow is not perpendicular to the grid, the upwind scheme results in a 'diffusion-like' appearance error, known as numerical or false diffusion. Higher order schemes and/or finer grid resolution reduces numerical diffusion errors. The Quadratic Upstream Interpolation for Convective Kinetics (QUICK) scheme uses a three-point upstream-weighted quadratic interpolation to compute cell face values. The QUICK scheme is more accurate on structured grids where unique upstream faces and cells can be identified.

2.2.1.3 Turbulence modelling

Various turbulence models are available to predict complex hydrodynamic features in mixing vessels. The appropriateness of a turbulence model is dependent on the system and the accuracy one wants to achieve. Turbulent flows are characterised by fluctuating velocities. Two modelling approaches are commonly used; the Reynolds Averaged Navier-Stokes

(RANS) and the Large Eddy Simulation (LES). With the latter, small-scale turbulent fluctuations do not have to be directly simulated. Additional terms are introduced for both methods in order to achieve a "closure" for the unknown variable. In the RANS approach the equations are ensemble-averaged, which reduces the computational expense and in the LES the large eddies are explicitly computed in a time-dependent simulation using the "filtered" Navier-Stokes equation.

Standard k-ε model

The standard k-ε model (Launder and Spalding, 1974) is one of the most widely used turbulence model due to its robustness and its ability to reasonably predict turbulent flows in various engineering applications. It is a two-equation model where two transport equations are solved to compute the Reynolds stresses. It is a semi-empirical model, where the turbulent kinetic energy, k, is from the exact Navier-Stokes equations and its dissipation rate, ε, is derived from physical reasoning and dimensional analysis. The derivation of the model is based on the assumptions that the flow is fully turbulent, the effects of molecular viscosity are negligible and turbulence is an isotropic process.

2.2.2 Multiphase Models

Multiphase models can be grouped into two main groups, namely Euler-Lagrange and Euler-Euler. The Euler-Lagrangian approach uses ensemble-averaged Navier-Stokes equations to describe a continuous phase and a tracking method to describe the discrete phase which can be either particles, bubbles or droplets. The Euler-Euler method uses different phases which are treated as inter-penetrating continua. The mixture model and the Euler-Euler model are most commonly used multiphase models for gas-liquid stirred systems.

2.2.2.1 Euler-Euler model

The Euler-Euler model (Khopkar et al., 2005; Scargiali et al., 2007) uses different sets of conservation equations for each phase. The equations are similar to the single phase equations but with the addition of a volume fraction term to describe multiphase flows. With additional sets of equations that need to be solved the Euler-Euler model becomes computationally intensive.

The volume fraction accounts for the space occupied by each phase, and the laws of conservation of mass and momentum are satisfied by each phase individually.

The volume occupied by a phase q, V_q, is given by:

$$V_q = \int_V \alpha_q dV \tag{2.14}$$

where α_q is the volume fraction of phase q

The sum of the volume fraction of all phases is always 1 in the control volumes:

$$\sum_{q=1}^{n} \alpha_q = 1 \tag{2.15}$$

The effective density of phase q is given by

$$\hat{\rho}_q = \alpha_q \rho_q \tag{2.16}$$

where ρ_q is the physical density of phase q.

Continuity equation

For the conservation of mass the resulting continuity equation for phase q is given by:

$$\frac{\partial}{\partial t}\left(\alpha_q \rho_q\right) + \nabla \cdot \left(\alpha_q \rho_q \vec{v}_q\right) = \sum_{p=1}^{n} \left(\dot{m}_{pq} - \dot{m}_{qp}\right) + S_q \tag{2.17}$$

where $\vec{v}_q$ is the velocity of phase q
$\dot{m}_{pq}$ is the mass transfer from the p^{th} to the q^{th} phase
$\dot{m}_{qp}$ is the mass transfer from phase q to phase p
S_q is the source term

Conservation of momentum

The momentum balance for phase q is represented by:

$$\frac{\partial}{\partial t}\left(\alpha_q \rho_q \vec{v}_q\right) + \nabla \cdot \left(\alpha_q \rho_q \vec{v}_q \vec{v}_q\right) = -\alpha_q \nabla p + \nabla \cdot \bar{\bar{\tau}}_q + \alpha_q \rho_q \vec{g} + \sum_{p=1}^{n} \left(\vec{R}_{pq} + \dot{m}_{pq}\vec{v}_{pq} - \dot{m}_{qp}\vec{v}_{qp}\right) + \left(\vec{F}_q + \vec{F}_{lift,q} + \vec{F}_{vm,q}\right) \tag{2.18}$$

where $\bar{\bar{\tau}}_q$ is the q^{th} phase stress-strain tensor:

$$\bar{\bar{\tau}}_q = \alpha_q \mu_q \left(\nabla \vec{v}_q + \nabla \vec{v}_q^T\right) + \alpha_q \left(\lambda_q - \frac{2}{3}\mu_q\right) \nabla \cdot \vec{v}_q \bar{\bar{I}} \tag{2.19}$$

where μ_q is the shear viscosity of phase q
λ_q is the bulk viscosity of phase q
$\vec{F}_q$ is the external body force
$\vec{F}_{lift,q}$ is the lift force
$\vec{F}_{vm,q}$ is the virtual mass force
$\vec{R}_{pq}$ is the interaction force between phases
p is the pressure shared by all phases
$\vec{v}_{pq}$ is the interphase velocity

The interaction term is given by:

$$\sum_{p=1}^{n} \vec{R}_{pq} = \sum_{p=1}^{n} K_{pq} \left(\vec{v}_p - \vec{v}_q \right) \tag{2.20}$$

where K_{pq} $(= K_{qp})$ is the inter-phase momentum exchange coefficient

Fluid-Fluid exchange coefficient

The inter-phase momentum exchange, K_{pq}, coefficient is used to account for momentum exchange between phases, for instance between water as well as gas bubbles and is given by:

$$K_{pq} = \frac{\alpha_q \alpha_p \rho_p f}{\tau_p} \tag{2.21}$$

where f is the drag function

τ_p is the particulate relaxation time

The relaxation time is given by:

$$\tau_p = \frac{\rho_p d_p^2}{18 \mu_q} \tag{2.22}$$

where d_p is the diameter of the bubbles of phase p.

The drag function depends on a drag coefficient C_D that is based on relative Reynolds numbers, Re. There are various drag models for multiphase systems such as the Schiller and Naumann model, the Morsi and Alexander model and the symmetric model. The most commonly used model is the Schiller and Naumann model.

The drag function for the Schiller and Naumann model takes the following form:

$$f = \frac{C_D Re}{24} \tag{2.23}$$

where

$$C_D = \begin{cases} 24 \left(1 + 0.15 Re^{0.687} \right) / Re & Re \leq 1000 \\ 0.44 & Re > 1000 \end{cases} \tag{2.24}$$

The relative Reynolds number for the primary phase q and the secondary phase p is given by :

$$Re = \frac{\rho_q |\vec{v}_p - \vec{v}_q| d_p}{\mu_q} \tag{2.25}$$

In contrast, the relative Reynolds number for the secondary phases p and r is given by:

$$Re = \frac{\rho_{rp} |\vec{v}_r - \vec{v}_p| d_{rp}}{\mu_{rp}} \tag{2.26}$$

where μ_{rp} is the mixture viscosity of phases p and r, and is equal to

$$\mu_{rp} = \alpha_p \mu_p + \alpha_r \mu_r \tag{2.27}$$

However, this correlation is only suitable for particles moving in a stagnant liquid. Thus, to account for the effect of turbulence, a modified drag law is often used (Bakker, 1992; Kerdouss et al., 2006). The relative Reynolds number is modified and is based on a modified viscosity term instead. This is given by:

$$Re = \frac{\rho_q |\vec{v}_p - \vec{v}_q| d_p}{\mu^*} \tag{2.28}$$

where the modified viscosity term is the sum of the primary phase and a term proportional to the eddy viscosity. It is written as:

$$\mu^* = \mu_q + C\rho\frac{k^2}{\varepsilon} \tag{2.29}$$

where C is a model parameter
ρ is the density
k is the turbulent kinetic energy per unit mass
ε is the turbulent energy dissipation rate

The parameter C is introduced to account for the decrease in slip velocity when a bubble is moving in a turbulent flow instead of in a still liquid (Bakker, 1992; Kerdouss et al., 2006).

But for the k-ε dispersed model (Kerdouss et al., 2008) the turbulent viscosity is related to k and ε through the semi-empirical expression:

$$\mu_t = \rho_q \frac{k_q^2}{\varepsilon_q} \tag{2.30}$$

where q represents the primary phase

Thus,

$$\mu^* = \mu_q + C\mu_{t,q} \tag{2.31}$$

k-ε dispersed model

The k-ε dispersed model is one of the models available to account for turbulence in multiphase flows. It is appropriate where the concentrations of the secondary phases are low and inter-particle collisions are negligible.

The Reynolds stress tensor for the continuous phase is given by:

$$\overline{\overline{\tau}}_q'' = -\frac{2}{3}\left(\rho_q k_q + \rho_q \mu_{t,q} \nabla \cdot \vec{U}_q\right)\overline{\overline{I}} + \rho_q \mu_{t,q}\left(\nabla\vec{U}_q + \nabla\vec{U}_q^T\right) \tag{2.32}$$

where $\nabla\vec{U}_q$ is the phase-weighted velocity
$\mu_{t,q}$ is the turbulent fluid dynamic viscosity
k_q is the turbulent kinematic viscosity

The two transport equations, for k and ε that need to be solved for this model are as follows:

$$\frac{\partial}{\partial t}\left(\alpha_q\rho_q k_q\right) + \nabla\cdot\left(\alpha_q\rho_q\vec{U}_q k_q\right) = \nabla\cdot\left(\alpha_q\frac{\mu t,q}{\sigma_k}\nabla k_q\right) + \alpha_q G_{k,q} - \alpha_q\rho_q\varepsilon_q + \alpha_q\rho_q\Pi_{k_q} \quad (2.33)$$

and

$$\frac{\partial}{\partial t}\left(\alpha_q\rho_q\varepsilon_q\right) + \nabla\cdot\left(\alpha_q\rho_q\vec{U}_q\varepsilon_q\right) = \nabla\cdot\left(\alpha_q\frac{\mu_{t,q}}{\sigma_\varepsilon}\nabla\varepsilon_q\right) + \alpha_q\frac{\varepsilon_q}{k_q}\left(C_{1\varepsilon}G_{k,q} - C_{2\varepsilon}\rho_q\varepsilon_q\right) + \alpha_q\rho_q\Pi_{\varepsilon_q} \quad (2.34)$$

where $G_{k,q}$ is the production of turbulent kinetic energy

The turbulent viscosity is related to the turbulent kinetic energy and the dissipation rate of turbulent kinetic energy via

$$\mu_{t,q} = \rho_q C_\mu\frac{k_q^2}{\varepsilon_q} \quad (2.35)$$

Π_{k_q} and $\Pi\varepsilon_q$ represent the influence of the dispersed phase on the continuous phase and are as follows:

$$\Pi_{k_q} = \sum_{p=1}^{M}\frac{K_{pq}}{\alpha_q\rho_q}\left(k_{pq} - 2k_q + \vec{v}_{pq}\cdot\vec{v}_{dr}\right) \quad (2.36)$$

where $\vec{v}_{pq}$ is the relative velocity
$\vec{v}_{dr}$ is the drift velocity
k_{pq} is the covariance of the velocities of the continuous phase q and the dispersed phase l

and

$$\Pi_{\varepsilon_q} = C_{3\varepsilon}\frac{\varepsilon}{k_q}\Pi_{k_q} \quad (2.37)$$

Table 2.1 outlines the various model constants used in the turbulence model.

Table 2.1: Values of coefficients for k-ε turbulence model as used in FLUENT®

$C_{1\varepsilon}$	$C_{2\varepsilon}$	$C_{3\varepsilon}$	C_μ	σ_k	σ_ε
1.44	1.92	1.2	0.09	1	1.3

All the other terms have the same meaning as in the single phase k-ε model and the various models constants used in the turbulence model are tabulated in Table 2.1.

2.2.2.2 Mixture model

The mixture model (Wallis, 1969; Zuber and Findlay, 1965) uses a different approach to the Euler-Euler model, where the system is modelled as a single-fluid. The phases can be inter-penetrating such that the volume fractions α_q and α_p for a control volume can be equal to any value between 0 and 1, depending on the fluid system used. The model also allows phases to move at different slip velocities. The continuity, momentum, energy and algebraic expressions for the relative velocities are based on a mixture determined on the space occupied by the different phases involved rather than a set of equations for each phase. Thus, the mixture model is computationally less intensive than the Euler-Euler model, where a set of equations for each phase has to be solved.

2.2.3 Population Balance Model

2.2.3.1 Bubble size distribution

The bubble size distribution (BSD) is dependent on various factors; the net rate of convection, bubble breakage and coalescence. Bubble breakage and coalescence can result in either death or birth as shown in Figure 2.3 and a population balance model can be used to model such phenomena. The population balance model is a set of mathematical models giving a detailed description of the dispersed phase characteristics (Azizi and Taweel, 2007). It allows the description of bubble breakage and coalescence processes in terms of physical parameters and operating conditions.

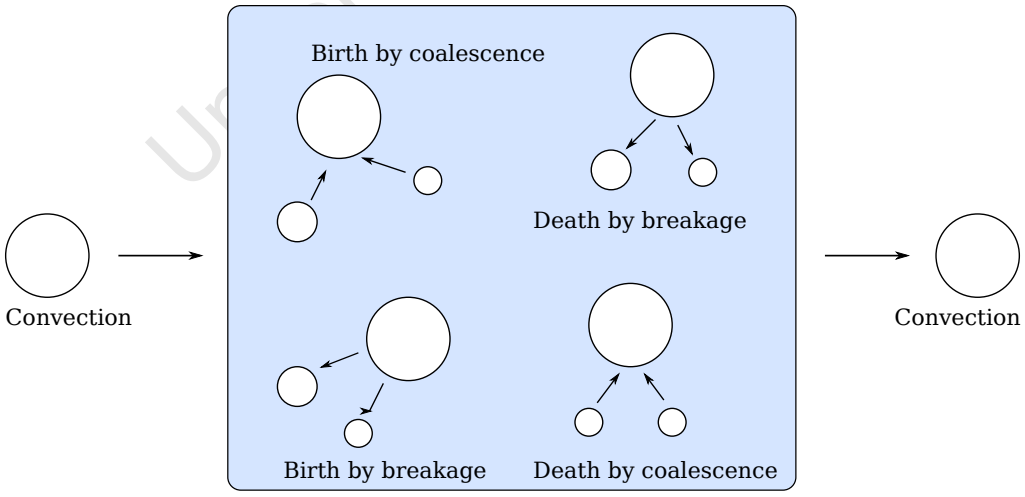

Figure 2.3: Bubble breakage and coalescence

The population balance model can also be used to account for particle growth or shrinkage. However, the shrinkage term due to mass transfer is neglected for this research work.

A similar approach was used by Kerdouss et al. (2008). The term was found to have a small effect on the bubble size distribution over the tank due to the low gas solubilities (Laakkonen et al., 2006a,b).

Historically, the population balance has been formulated in various ways. There are three ways that have been formulated (Jakobsen, 2008). Two of the population balance forms are formulated based on the conventional continuum mechanical theory, namely a macroscopic approach and a microscopic approach. The third approach is derived by averaging a statistical Boltzmann-type of equation.

The macroscopic approach consists in describing the evolution in time and space of several groups or classes of the dispersed phase properties (Jakobsen, 2008). That is, it is directly formulated on the averaging scales in terms of number density functions. The population balance kernels are based on eddy collision arguments. These rely on the fact that turbulent flows consists of a collection of fluid eddies which are treated using relationships based on the kinetic theory of gases. This engineering eddy concept is impossible to validate regarding eddy shape, the number densities and the breakage mechanisms (Jakobsen, 2008).

The microscopic approach considers a continuum representation of a particle density function (Jakobsen, 2008). The population balance model describes evolution of populations of countable entities like bubbles, drops and particles. Phenomenological characteristics are implemented based on the interpretations of the mechanisms. The links to discrete particles scale phenomena are usually expressed on averaging scales extrapolating relationships and concepts from the kinetic theory of gases. It allows for the introduction of external forces which determine the interaction between the fluid and the dispersed phase. This method is convenient for multiphase systems where the discrete phase is treated as a population of particles distributed in both a physical space (continuous phase) and the property space. Hulburt and Katz (1964) referred to the external coordinates as external coordinates and the property coordinates as internal coordinates. This technique was implemented in the modelling approach developed by Randolph and Larson (1988), Himmelblau and Bischoff (1968) as well as Ramakrishna (2000). These methods are further described below.

Particulate dispersed-phase systems are inherently complex as one needs to consider two "sub-systems" or from a mathematical point of view two coordinate systems. Firstly, to account for a particulate system and secondly for a spatial concentration. These two types of coordinate axes are defined as (Randolph and Larson, 1988):

- Internal coordinate properties, which could be the size, concentration, chemical activity or temperature
- External coordinates, which denote the x, y, z spatial coordinates giving the location of the particle

2.2.3.2 Particle phase space

The particle phase space also referred to by a particle phase vector is the combined internal and external region. Therefore, with m independent internal coordinates, the particle phase space is an $(m + 3)$-dimensional space.

The number of particles at time t in an incremental particle phase space dR and is given by:

$$dN = ndr \tag{2.38}$$

where n is the population density

The total number of particles in some finite subregion of particle phase space R_1 is given by:

$$N(R_1) = \int_{R_1} ndR \tag{2.39}$$

2.2.3.3 Population fluxes

In a particulate system with the formation of a particle distribution, particles change their position in the particle phase space continuously (Randolph and Larson, 1988). That is, each particle moves along various internal and external coordinate axes. The gradual and continuous changes is referred to as a convection along the respective particle coordinates. The rate of change of the coordinate property of a particle is referred to as the convective particle velocity along that coordinate axis. The vector particle phase-space velocity is defined as:

$$\mathbf{v} = \mathbf{v}_\mathrm{e} + \mathbf{v}_\mathrm{i} \tag{2.40}$$

The external velocity $\mathbf{v}_\mathrm{e}$ is not necessarily the same as the fluid velocity u. The internal particle velocities $\mathbf{v}_\mathrm{i}$ are assumed to be a unique function of the state of the particle. For example, the linear growth of a particle is an internal convection velocity.

Population fluxes also represent birth or death functions of the particle distribution. These can be related to the state of the total system and/or to the position of a particle in the particle phase space. Statistical methods are usually used to represent birth and death. Death are statistically related with the position of the particle in the particle phase space.

While birth depends on the entire distribution of particles. These require integrals of the distribution function, such that the particle distribution is described by solution of a set of integro-differential equations.

2.2.3.4 Particle-number continuity equation

The population for particles in a fixed sub-region can be written as:

$$\text{Accumulation} = \text{Input} - \text{Output} + \text{Net generation} \tag{2.41}$$

Considering the subregion, R_1, to move convectively with the particle phase-space velocity v (Lagrangian), the population balance for particles in the subregion R_1 is given by:

$$\frac{d}{dt}\int_{R_1} n dR = \int_{R_1} (B - D)\, dR \tag{2.42}$$

This can be written as:

$$\frac{d}{dt}\int_{R_1} \frac{\partial n}{\partial t} dR = \int_{R_1} \frac{\partial n}{\partial t} dR + \left(n\frac{d\mathbf{x}}{dt}\right)\Bigg|_{R_1} = \int_{R_1} \left[\frac{\partial n}{\partial t} + \nabla \cdot \left(\frac{d\mathbf{x}}{dt} n\right)\right] \tag{2.43}$$

where $\mathbf{x}$ is the set of internal and external coordinates comprising phase space R.

$$\frac{d\mathbf{x}}{dt} = \mathbf{v} = \mathbf{v}_\mathrm{e} + \mathbf{v}_\mathrm{i} \tag{2.44}$$

Then, the population balance in the Lagrangian region is given by:

$$\int_{R_1} \left[\frac{\partial n}{\partial t} + \nabla \cdot (\mathbf{v}_\mathrm{e} n) + \nabla \cdot \left(\mathbf{v}_\mathrm{i} n\right) + D_r - B_r\right] dR = 0 \tag{2.45}$$

The most general form of the model for a flow system, can be given as

$$\frac{\partial n}{\partial t} + \nabla \cdot (\mathbf{v} n) - B_r + D_r = 0 \tag{2.46}$$

where n is the population density
B_r is the birth rate
D_r is the death rate
$\mathbf{v}$ is the velocity vector

The statistical mechanical microscopic approach is based on the Boltzmann theory of gases (Jakobsen, 2008). A single distribution function $p(\mathbf{x},\mathbf{r},\mathbf{c},t)\ d\mathbf{x}d\mathbf{r}d\mathbf{c}$ describes the probable number of particles with internal coordinates in the range $d\mathbf{x}$ about $\mathbf{x}$. The term also includes a spatial range $d\mathbf{r}$ about the position $\mathbf{r}$ and a velocity range $d\mathbf{c}$ about $\mathbf{c}$ at time t.

2.2.3.5 Finite volume models

The population balance model using the finite volume method is described in this section and followed by an overview of the kernels required for breakage and coalescence.

The population balance model is given by:

$$\frac{\partial}{\partial t}\left[n(v,t)\right] + \nabla\cdot\left[\vec{u}n(v,t)\right] + \underbrace{\nabla_v\cdot\left[G_v n(v,t)\right]}_{\text{Growth term}} = \underbrace{\frac{1}{2}\int_0^v a(v-v',v')n(v-v',t)n(v',t)dv'}_{\text{Birth due to Aggregation}} - \underbrace{\int_0^\infty a(v,v')n(v,t)n(v',t)dv'}_{\text{Death due to Aggregation}} + \underbrace{\int_{\Omega_v} pg(v')\beta(v|v')n(v',t)dv'}_{\text{Birth due to Breakage}} - \underbrace{g(v)n(v,t)}_{\text{Death Due to Breakage}} \tag{2.47}$$

The boundary and initial conditions are given by

$$n(v,t=0) = n_v; \qquad n(v=0,t)G_v = \dot{n}_0 \tag{2.48}$$

The model accounts for bubble breakage and bubble coalescence, where both can occur by either birth or death.

In the term representing birth due to breakage, $g(v')n(v')dv'$ is the number of particles breaking per unit time to produce $pg(v')n(v')dv'$ particles, where $\beta(v|v')dv$ is the fraction of particles of volume v. p is the number of child particles produced per parent. In the term accounting for birth due to coalescence particles of volume $v-v'$ coalesce with particles of volume v' to produce particles of volume v. To avoid accounting for each collision event twice a factor of half is included.

The coalescence and breakup kernels are needed to solve the population balance model. The kernels depend on the nature of the physical application. In gas-liquid systems, the kernels are derived from the liquid-phase turbulent dissipation. A complete breakup model include the breakup rate and the daughter size distribution. The daughter size distribution is needed for the calculation of the bubble breakage rates. Also referred to as the breakage kernel, it is needed to determine the frequency with which the bubbles break from a size category to a smaller category. The bubble breakage rate model developed by Luo (1993) has no unknown parameters, all constants are determined from the isotropic turbulence theory. The daughter size distribution can directly be derived from the breakage rate model. These are explained in Sections 2.2.3.7 - 2.2.3.8.

2.2.3.6 Solution methods

There are different ways to solve the population balance model. The Discrete Method, the Standard Methods of Moments and the Quadrature Method of Moments are the most widely used numerical techniques. These are discussed further below.

Discrete method

The discrete method is also known as the classes or sectional method. This approach is based on the discretization of the particle internal coordinate(s), leading to a discretized population balance (DPB) (Marchisio et al., 2003). That is the particle coordinate is discretized into a finite number of size intervals (bins), such that the particle size distribution is directly simulated rather than inferring from lower-order moments. This method is simple to use since the integrals are replaced with summations (Lister et al., 1995) and it is also stable. However, one disadvantage of this method is that the computation becomes very intensive if a large number of intervals is required.

The Standard methods of moments (SMM)

In many engineering problems the knowledge of a complete particle distribution is unnecessary. Rather, an average or a total quantity is enough to describe the particle distribution. The standard methods of moments is another approach to solve the population balance model, proposed by Randolph and Larson (1988) uses this method. The dimensions for transport equations for mass, momentum and energy and the population balance equation are respectively 3 (spatial coordinates) and m+3 (internal + external coordinates). This difference in dimensions leads to the difficulty in solving the equations simultaneously. This approach averages the distribution with regard to the internal coordinates' properties and reduces dimensionality of the problem. It uses lower-order moments that can be tracked directly without prior knowledge of a distribution (McGraw, 1997). That is, this method tracks the moments of the particle size distribution (PSD) rather than the entire PSD. Even though it uses a small number of moments, this method is limited by its closure requirements. Only size-independent growth rate, size-independent aggregation and breakage kernels can result in an exact closure.

The population balance equation is solved by expressing it in terms of a number density function using particle length as the internal coordinate (Marchisio et al., 2003). Then the resulting equation is transformed by applying the moment transformation:

$$m_k(t) = \int_0^{+\infty} n(L;t)L^k dL \tag{2.49}$$

where $n(L;t)$ is the length-based number density function

The Quadrature Methods of Moments (QMOM)

The quadrature methods of moments (QMOM) technique was proposed by McGraw (1997) for modelling aerosol evolution and coagulation problems. This approach is based on the SMM technique of solving only transport equations of lower-order moments. Such that fewer variables than the discrete method are used and the bin size is calculated dynamically (ANSYS, 2010). This method also overcome closure constraints showed by the SMM. However, this method has shown some limitations, the number of abscissas can be insufficient to describe the PSD and solving the product-difference (PD) algorithm may be time consuming.

After the population balance equation is expressed in terms of number density functions and a moment transformation using equation (2.49) is made, the QMOM is applied by using a quadrature approximation:

$$m_k = \int_0^{+\infty} n(L;t)L^k dL \approx \sum_{i=1}^{N} w_i L_i^k \tag{2.50}$$

where weights (w_i) and abscissas (L_i) are determined via the product-difference algorithm from lower-order moments. The abscissas are the eigenvalues of the Jacobi matrix and the weights are the squares of the first component of the eigenvectors. Thus, with the known abscissas and weights, the source terms due to coalescence and breakage can be calculated and the transport equations for moments solved.

2.2.3.7 Bubble break-up

One of the most common mechanism for bubble breakup is based on the balance between disruptive external stresses and surface stresses that resists deformation (Hinze, 1955). The breakup of bubbles in turbulent flows starts with a deformation of the bubble by a turbulent field. The bubble is stretched in one direction. This leads to the necking of the bubble which eventually breaks. Breakage may start with arrival of eddies of different length scales on the bubble surface. But it is assumed that only eddies with length scales less than the diameter of a bubble will lead to breakage.

The breakage rate expression is given by:

$$g(v')\beta(v|v') \tag{2.51}$$

where $g(v')$ is the fraction of particles of volume v' breaking per unit time referred to as the breakage frequency and $\beta(v|v')$ is the probability density function of particles breaking from volume v' to a particle of volume v. The PDF $\beta(v|v')$ is also referred to as the daughter size distribution.

There are various models to calculate breakage frequency and breakage PDF. The ones that are commonly used in literature are the Luo and the Lehr models. The models incorporate both a breakage frequency and a PDF of breaking particles. The general breakage rate per unit volume is given by (Lehr et al., 2002):

$$\Omega_{br}(v,v') = \Omega_B(v')\eta\left(v|v'\right) \tag{2.52}$$

where Ω_{br} is the breakage rate per unit volume $(1/(\mathrm{m}^3 s^{-1}))$
$\Omega_B(v')$ is the breakage frequency
v is the original volume of a bubble (m^3)
v is the original volume of a bubble (m^3)
$\eta(v|v')$ is the normalized daughter particle distribution function

Luo Breakage Model

The breakup rate function is given by (Luo and Svendsen, 1996):

$$\Omega_{br}\left(v,v'\right) = c_4\varepsilon^{1/3}d^{-2/3}\alpha\int_{\xi_{min}}^{1}\frac{(1+\xi)^2}{\xi^{11/3}}\times\exp\left(-\frac{12\left(f^{2/3}+(1-f)^{2/3}-1\right)\sigma}{\rho\varepsilon^{2/3}d^{5/3}\xi^{11/3}}\right)d\xi \tag{2.53}$$

where $c_4 = 0.923$ and $\xi_{\min} = \lambda_{min}/d$

However, this model has some deficiencies (Laakkonen, 2006). It has a dependence on the size discretization. The author suggested that this can be avoided by integrating the breakage rates over all breakage volume fraction and by using a separate model for the daughter size distribution.

The integral can be calculated using incomplete gamma functions (Alopaeus et al., 1999):

$$\Omega_{br}(v,v') = \frac{-3c_4(1-\alpha_G)}{11b^{8/11}}n_j\left(\frac{\varepsilon}{d_j^2}\right)^{1/3}\times\left\{\Gamma\left(\frac{8}{11},t_m\right)-\Gamma\left(\frac{8}{11},b\right)\right.$$
$$\left.+2b^{3/11}\left(\Gamma\left(\frac{5}{11},t_m\right)\Gamma\left(\frac{5}{11},b\right)\right)+b^{6/11}\left(\Gamma\left(\frac{2}{11},t_m\right)-\Gamma\left(\frac{2}{11},b\right)\right)\right\} \tag{2.54}$$

Lehr Breakage Model

The Lehr breakage kernel is given by:

$$\Omega_{br}(v,v') = 1.19\varepsilon^{1/3}d^{-7/3}\sigma\rho^{-1}f^{-1/3}\int_{\xi_{\min}}^{1}\frac{(1+\xi)^2}{\xi^{13/3}}\exp\left(\frac{-2\sigma}{\rho\varepsilon^{2/3}d^{5/3}f^{1/3}\xi^{2/3}}\right)d\xi \tag{2.55}$$

2.2.3.8 Bubble coalescence

Coalescence is usually considered to occur in three stages. The bubbles collide and trap a small liquid film. This liquid film drains until the film ruptures resulting in coalescence (Luo, 1993). Based on the processes, coalescence can be analysed by looking at the

collision and efficiency of the collision. That is coalescence will depend on the collision frequency and the reaction of collisions resulting in coalescence, also known as coalescence efficiency and coalescence probability.

The aggregation kernel expression is given by:

$$a(v, v') \tag{2.56}$$

It is the product of the two quantities. Firstly, the frequency of collisions between particles of volume v and particles v'. Secondly, the probability of particles of volume v colliding with particles of volume v', also known as the "efficiency of aggregation". There are various models available, the Luo model is explained in detail in the following section.

Luo coalescence model

The coalescence rates can be expressed as the product of the collision rate and collision probability (Luo, 1993):

$$\Omega_C(v_i; v_j) = \omega_C(v_i; v_j) P_C(v_i, v_j) \tag{2.57}$$

where ω_C is the collision freqency
P_C is the coalescence frequency
v_i, v_j are the volume of bubbles i and j (m^3)

The collision rate is given by Saffman and Turner (1956):

$$\Omega_C = \frac{\pi}{4} (d_i + d_j)^2 n_i n_j \overline{u}_{ij} \tag{2.58}$$

where u_{ij} is the velocity of collision of two particles with diameters d_i and d_j and number densities n_i and n_j.
The mixing velocity is given by:

$$\overline{u}_{ij}^t = \left(\overline{u}_i^2 + \overline{u}_j^2\right)^{1/2} \tag{2.59}$$

where

$$\overline{u}_i = 1.43 \left(\varepsilon d_i\right)^{1/3} \tag{2.60}$$

The collision or coalescence probability is given by:

$$P(v_i, v_j) = \exp\left\{ -c \frac{\left[0.75 \left(1 + x_{ij}^2\right) \left(1 + x_{ij}^3\right)\right]^{1/2}}{\left(\rho_g / \rho_L + 0.5\right)^{1/2} \left(1 + x_{ij}\right)^3 We_{ij}^{1/2}} \right\} \tag{2.61}$$

where c = 1, $x_{ij} = d_i / d_j$ and

$$We_{ij} = \frac{\rho_L d_i \left(\overline{u}_{ij}^t\right)^2}{\sigma} \tag{2.62}$$

2.3 Hydrodynamics

2.3.1 Theory

Mixing in mechanically stirred tanks is a fundamental process in chemical, biomechanical and mineral processing industries (Tatterson, 1991). The processes vary from blending of miscible and immiscible liquids, to suspensions of solids, chemical reactions and gas-liquid/liquid-liquid mass transfer. Quite often the mixing process is not well understood and a comprehension of the physics of the process is required before modelling the system. An insight into the hydrodynamics (flow regime and power draw) gives a good starting point. Various research studies have been undertaken to better understand fluid flows in mixing vessels. The studies show that the fluid mechanics depend on many factors and the main ones are vessel geometry, impeller type, fluid properties and operating conditions.

Most of the research work has focused on stirred tanks with either Rushton or pitched blade turbines and to the author's knowledge, besides the work of Nicolle et al. (2009), there has been no published experimental work emphasising on hydrodynamics in autoclaves. However, the characteristic fluid flow regime observed in mixing vessels, particularly stirred tanks, is expected to be similar in nature for autoclaves. The fluid flow in a baffled stirred tank with a Rushton turbine is well known, with the characteristic recirculation loops. These are caused by the high radial flows jetted outwards which split into two upon hitting the vessel as shown in Figure 2.4(a).

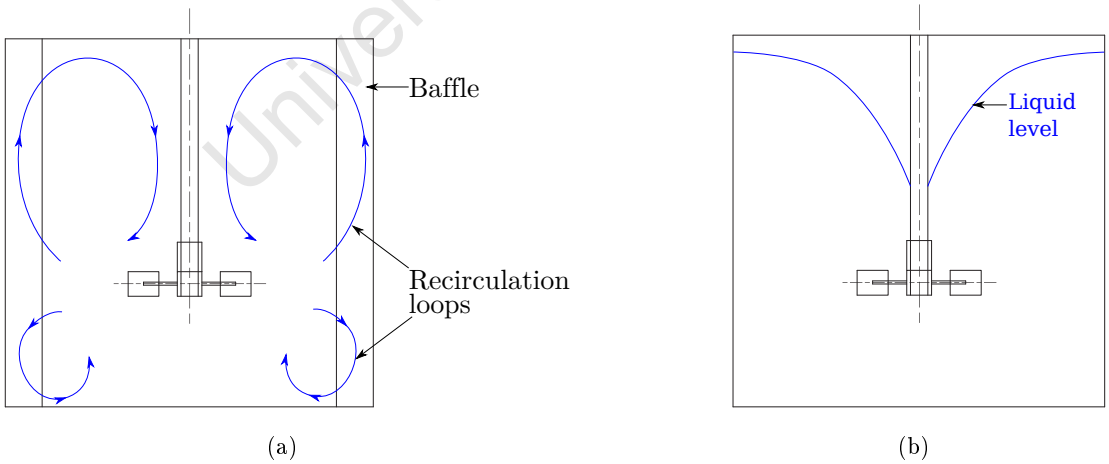

Figure 2.4: (a) Baffled stirred tank, (b) Unbaffled stirred tank

The baffles also play an important role in the hydrodynamics. The absence of baffles in a cylindrical vessel produce rotary and laminar flow (Rushton et al., 1994). These give rise to small relative velocities between the impeller and the fluid as well as weak radial flows directed towards the tank walls (Ciofalo et al., 1996). The resulting flow leads to

poor mixing and in the formation of a vortex on the free surface of the liquid as shown in Figure 2.4(b). Baffles prevent the formation of the vortex and result in an almost flat liquid surface.

The position of the shaft also influences the flow field and in an unbaffled vessel, the frequency of the vortex formation (Galletti et al., 2009). The eccentricity of the impeller shaft results in two main vortical structures; one above and one below the impeller. The vortices are unsteady but oscillate slowly and periodically creating flow instabilities with an impact on macro-mixing.

The impeller clearance from the bottom of the vessel affects the flow pattern in stirred tanks. Nienow (1968) observed that the known double-loop flow structure with radial flow impellers changes to a single-loop when the distance between the impeller and bottom of the vessel is reduced. Similar observations were made by Montante et al. (2001) where the system was numerically modelled.

2.3.2 Experimental

2.3.2.1 Power

Power draw is the amount of energy required per unit time to move the content of a vessel by mechanical agitation. There are various techniques available to measure power consumption in mechanically agitated tanks, namely, electrical measurements, calorimetric measurements, dynamometers, torquemeters and strain gauges (Ascanio et al., 2004). The different methods are appropriate for different applications.

Power using electrical measurements is obtained from the current and the supply voltage. However this simple method is not very accurate. The power input is not equal to the power output due to losses involved. Even though the losses can be determined from the efficiency of the motor they can be difficult to find since they are load dependent.

The calorimetric measurement technique is based on an energy balance approach. Thermistors placed at different positions are used to measure temperature variations. This method is very accurate and accounts for losses due to friction. However, the expression required for a fluid system comprising of various phenomena, such as chemical reactions, heat transfer or bubble breakage is complex. This method also requires highly sensitive thermistors, which is an intrusive method and as a result can also alter the flow patterns.

Dynamometers are also used to measure power draw. This method is based on New-

ton's third law. The resistive force on a fluid upon mechanical agitation results in a torque on the impeller. The latter is transmitted through a shaft to the motor and the reaction causes the vessel to rotate freely in the same direction as the impeller. For this method the vessel is normally placed on a low friction turntable (or torque turntable) so that the vessel rotates freely. The torque is measured from the force transmitted to the lever arm and the power is hence determined from the known impeller angular velocity.

The power is given by:

$$\text{Power} = FB_l\omega \tag{2.63}$$

where F is the force applied for counter rotation (N)
B_l is the lever arm (m)
ω is the angular velocity (rads^{-1})

The mean energy dissipation is given by:

$$\epsilon = \frac{2\pi NmgB_l}{\rho V} \tag{2.64}$$

where m is the mass applied for counter rotation (kg)
g is the gravitational acceleration (ms^{-2})
B_l is the lever arm (m)
N is the stirring speed (s^{-1})
$\rho \cdot V$ is the mass of the fluid in the cell (kg)

The power draw is also commonly determined from measurements of torque with a torquemeter. It consists of a transducer, which is coupled to the shaft by means of a rigid or flexible couplings, and a signal amplifier. The strain experienced by the shaft is measured by the transducer as a change in electrical resistance. The signal produced is directly proportional to the torque applied. The power is hence determined from known angular velocity.

A similar way of determining power draw is by using strain gauges. The latter are placed on the shaft and the strain experienced under a known stress is thus obtained. The mechanical strains are converted into electrical signals and calibrated to determine the torque experienced by the shaft.

2.3.2.2 Velocity and turbulence

The investigation of velocity fields in stirred tanks has been the subject of many research studies. Mavros (2001) gives an excellent review of different measurement techniques, single point and ensemble, as well as results for each of them.

There are many non-intrusive techniques that have been developed for measurements of velocity and turbulence. These highly promising techniques for the study of fluid flows, especially turbulent flows, have led to very precise and accurate measurement methods. Turbulence occurs over a broad range of physical scales, from the largest scales of the flow to the small Kolmogorov scale (Adrian, 2005). They are also random in nature. Therefore, the flows in all directions are required. Moreover, since turbulence often occurs at high Reynolds numbers, flows with high velocities and high acceleration need to be measured. A few techniques have been developed to measure these characteristics; Laser Doppler anemometry (LDA), Laser Doppler velocimetry (LDV) and particle image velocimetry (PIV).

The LDA technique has been used since the mid-1970s (Paul et al., 2003) and applied for the investigation of the flow field in stirred vessels (Lee and Yianneskis, 1994; Ng et al., 1998; Montante et al., 2001; Hartmann et al., 2004). Similarly, LDV has been used either to validate CFD models or to understand the flow patterns in mixing vessels (Shäfer et al., 1997; Armenante et al., 1997; Bittorf and Kresta, 2000; Aubin et al., 2001)

PIV is a quantitative velocity measurement technique based on images of tracer "seeding" particles suspended in a fluid flow (Paul et al., 2003). The tracer particles are used to visualise the flow field and images are analysed to measure the velocity flow field. This is determined by measuring the displacement of tracer particles from multiple images over the time interval between exposures. The accuracy of the measurement depends on the exposure time, which should be smaller than the time scales in the flow and the spatial resolution and which should also be shorter than the length scales in the flow.

Figure 2.5 shows a schematic of a typical PIV system. The PIV technique involves two main processes; firstly, the image capturing for visualisation and secondly analysis (Okamoto et al., 2000). A pulsed laser is used to create a light sheet to illuminate a cross-section of the seeded flow. The high intensity pulsed laser allows for the measurement of phenomena such as turbulence, which is random, varies in time scales (with size varying between the scale of the flow and the Kolmogorov scale), has high velocities and accelerations (Adrian, 2005).

There are different PIV techniques, such as holographic PIV, laser-induced fluorescence (Okamoto et al., 2000) and stereoscopic PIV. Most PIV techniques measure only two components of velocity. The third component is obtained by projection onto the plane defined by the light sheet. However, this method can lead to considerable errors. The stereoscopic PIV technique allows for the measurement of three-component velocity field

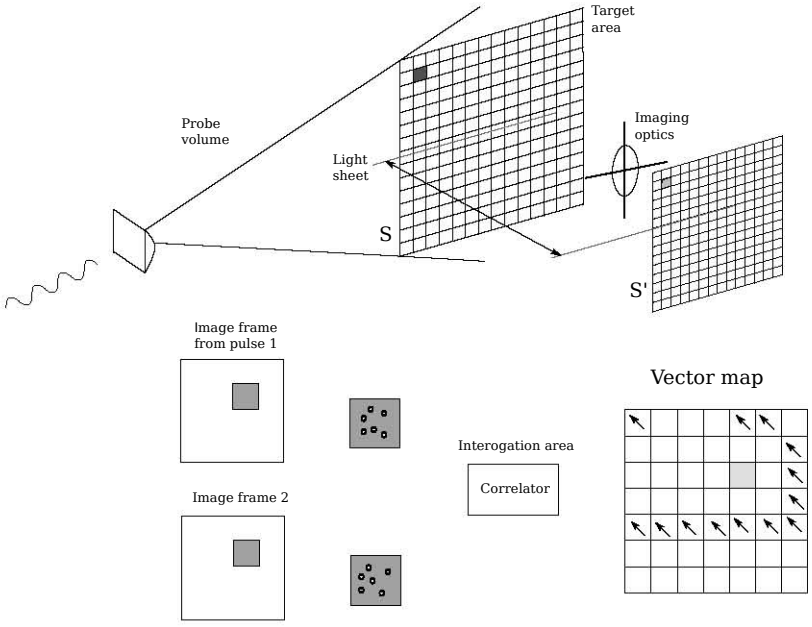

Figure 2.5: PIV system (Paul et al., 2003)

in a planar region illuminated by the laser light sheet. Two cameras placed at different angles record the displacement of the particles. The 3-D displacements are obtained from a proper calibration of two different 2-D images from two cameras (Paul et al., 2003).

Bakker et al. (1996) were among the first users to study two-dimensional flow patterns at a centre plane of a stirred tank for a single phase system. A similar study was performed by Sheng et al. (1998) for the validation of CFD simulations for a stirred tank with a down-pumping 4-bladed pitched blade turbine. The mean velocity and turbulence characteristics were compared whilst investigating the effect of boundary conditions on the CFD simulations. The PIV measurements reported by Ranade et al. (2001a) were emphasised on the flow field and trailing vortices generated by the standard Rushton turbine. In addition to PIV measurements in single phase systems research studies have also been performed in multiphase systems (Ranade et al., 2001b; Aubin et al., 2004b; Svensson and Rasmuson, 2006).

2.3.3 Numerical

Despite the progress made using experimental techniques there was still a need for detailed information about the flow field in stirred tanks (Shäfer et al., 1997). Thus, predictive methods such as Computational Fluid Dynamics have been used, with the first step being single phase flows. Various research work coupled with experimental techniques such as LDV (Armenante et al., 1997) and PIV (Sheng et al., 1998; Ranade et al., 2001a) were presented to provide enhanced information about 3-dimensional flows (Mavros, 2001).

Comprehensive single phase studies have been presented to enhance the prediction of flow field and associated phenomena in stirred tanks. These, as detailed below, were focused on the investigation of the effect of discretisation schemes, turbulence models, grid resolution as well as impeller rotation models on predictive abilities of stirred tanks CFD simulations.

Aubin et al. (2004a) investigated three discretisation schemes; upwind, higher order upwind and quadratic upwind differencing schemes. The authors found that the type of discretisation scheme has little or no effect on the prediction of the mean velocities. However, the first order upwind method under-predicted the small swirling region below the impeller. The dimensionless kinetic energy was under-predicted for the three numerical schemes, but was more significant for the upwind scheme.

The power-law discretisation scheme was used for the research conducted by Javed et al. (2006). The velocities were accurately predicted, however the turbulent kinetic energy was under-predicted throughout the tank.

The work presented by Brucato et al. (1998a) made a comparison between the standard hybrid-upwind and the QUICK discretisation scheme. The authors showed that the two schemes gave slightly different results with respect to velocities, which were comparable to experimental values. The QUICK scheme predicted a slightly higher recirculation rate near the top and bottom of the tank.

Deglon and Meyer (2006) investigated the effect of the upwind central and QUICK discretisation scheme. The authors concluded that, for a case where the grid was not too coarse, the mean velocity was negligibly affected by the discretisation scheme used. In contrast, the turbulent kinetic energy was highly influenced by the discretisation scheme. The authors also concluded that a high order discretisation scheme was required for more accurate CFD predictions.

The effect of turbulence models has been investigated in different studies, where the authors have looked at different variants of the k-ε, LES and k-ω models. Jaworski and Zakrzewska (2002) compared the standard k-ε model and five of its variants. There was negligible difference between predictions of the axial velocity. The tangential velocity was well predicted irrespective of the turbulence model used. Turbulent kinetic energy was under-predicted with all models, however the standard k-ε model agreed better to the experimental values. Similar observations were made by Aubin et al. (2004a) while comparing the standard and the RNG k-ε model. In general the standard k-ε model predicted the flow field and the velocity components reasonably well (Javed et al., 2006;

Montante et al., 2001; Ranade et al., 2001a). However, the turbulence parameters were under-predicted close to the impeller blade. This discrepancy as reported by Deglon and Meyer (2006) was due to numerical errors and can be reduced by using higher order discretisation schemes and/or finer grids.

Even though, the LES model has been limited to only a few research studies, primarily due to the computational expense involved, reasonably good predictions have been observed. Derksen and van Den Akker (1999) found that the LES model gave good predictions of the mean velocity and turbulence intensities. However, it was found to over-predict tangential velocities and turbulent kinetic energy values (Hartmann et al., 2004). Recently, Delafosse et al. (2008) compared the flow predictions using the LES and RANS turbulence model to PIV data. The authors reported a better prediction of turbulence parameters with the LES than with the RANS models. Similar findings were observed by Yapici et al. (2008); the flow prediction compared well to experimental data. Moreover, it was found that decreasing the impeller clearance and increasing the turbine disc resulted in a decrease in the power number.

Several numerical methods have been developed to simulate impeller rotation in mixing vessels as properly reviewed by Brucato et al. (1998a). Harvey and Greaves (1982) modelled the system using experimental data. A two-dimensional grid was used and the impeller rotation was modelled as a "black-box" and velocity profiles were used on the periphery of the box. Middelton et al. (1986) presented the first three-dimensional model of an impeller rotation model. A similar method was used by Ranade (1997) where it was referred to as the snapshot model. A second approach was used where the control volume surrounding the impeller swept region was defined using momentum sources. However, this method showed some weak points as outlined by authors such as Fokema et al. (1994) The approach was found to be only adequate for geometrically similar tanks and impellers.

Luo et al. (1993) developed a model that solved a time-dependent form of the governing equations for a computational domain comprising of two regions. The inner domain was solved with a reference rotating with the impeller and the outer one stationary with respect to the reference frame. The mesh was allowed to shear or slide at the interface to account for relative motion. This steady state method is referred to as the multi-reference frames (MRF) model. Its suitability for time-averaged flows allows the MRF model to be used for applications where the rotor-stator interaction is weak. The MRF model has been used in various research studies (Lane et al., 2002; Aubin et al., 2004a; Deglon and Meyer, 2006). The model was found to give reasonable predictions of flow patterns and fluid velocities.

Perng and Murthy (1993) developed a moving mesh method, known as the sliding mesh (SM) model. To implement the model, as in the MRF method, the computational domain is divided into two different regions. The grid surrounding the rotating component physically moves, by rotating in a stepwise manner. This method has to be solved in an unsteady manner since the grid motion is accounted for by transforming the time derivatives of the Eulerian conservation equations into a Lagrangian form. The grid defining the impeller region moves such that time-accurate simulation of the impeller-baffle interaction is achieved and it gives a realistic model of the impeller. Although being computationally expensive the sliding mesh approach has been used in several research studies. The flow field and the velocity components were generally well predicted (Brucato et al., 1998a; Hartmann et al., 2004; Deglon and Meyer, 2006). However, the turbulent kinetic energy values in the impeller region were poorly predicted (Brucato et al., 1998a).

Ng et al. (1998) investigated the flow in a stirred tank using the sliding mesh model and compared the predictions to experimental LDA data. The predicted mean velocity profiles agreed well with the measured data. Moreover, it was reported that grid refinement did not significantly improve the predicted velocities. However, the turbulent kinetic energy, k, was under-predicted in the region near the impeller blade. This discrepancy was attributed to grid size, time step size, wall region treatment, discretization scheme and turbulence model. Wechsler et al. (1999) reported that the discrepancy in the prediction of turbulent kinetic energy is mainly due to the grid resolution rather than an inadequacy of the turbulence model. Montante et al. (2001), using a flat bottom stirred tank, reported that the relatively small improvement in the turbulent kinetic energy with finer meshes implied that further grid refinement was unlikely to give a better prediction. The authors also noted that the prediction for a system with a single-loop configuration, the discharge angle was over-estimated. The stream over prediction towards the bottom is thought to depend on flow phenomena such as the 'Coanda' effects which the simulation approach used could not reproduce.

The prediction of power has also been investigated. Power is usually calculated using two methods; either from torque or using the turbulence energy dissipation rate. Singh et al. (2011) reported that the power calculated on torque gave a better indication of the actual power than the predicted power calculated from the turbulence energy dissipation rate. This is sensible as power calculated is a 'direct' calculation whereas the turbulent kinetic energy is estimated from the turbulence model and integrated through the entire vessel, that is an 'indirect' calculation based on an approximate turbulence model. The effect of discretisation schemes and grid resolution has been investigated by authors such

as Deglon and Meyer (2006). The authors reported that the accuracy of the prediction increased with grid resolution and the order of discretisation schemes. The closest prediction was about 10% lower than the experimental value. The magnitude of the under-prediction was observed to increase with Reynolds numbers. The difference was thought to be possibly due to the impeller blades being modelled as infinitely thin walls. However, the experimental study of Rutherford et al. (1996) showed that an increase in blade thickness resulted in a decrease in the power number. Therefore, modelling the blades as infinitely thin walls would lead to an over-prediction of the power number.

CFD modelling of autoclaves has been very scarce. Recently Nicolle et al. (2009) modelled the first compartment of an autoclave agitated by three impellers. The flow field of the slurry that was fed into the vessel was investigated. The system was found to be well-mixed and the overall flow pattern was found to be uninfluenced by the direction of rotation of adjacent agitators.

2.4 Gas Dispersion

2.4.1 Theory

Gas dispersion gives a quantitative and a qualitative description of the gas phase in terms of gas hold-up and gas distribution in the tank respectively. Gas hold-up (ε) is described as the dimensionless volume fraction of the gas phase in the dispersion and is normally experimentally determined by a volume or area balance performed across a section of a tank (Tatterson, 1991). In stirred tanks gas dispersion is influenced by factors such as impeller speed, gas flow-rate, vessel and impeller geometry as well as fluid properties. The most common method to gasify the system is via a sparger placed below the impeller as shown in Figure 2.6.

When the gas leaves the sparger it rises to the impeller where it is either dispersed to the top of the vessel or recirculates to the impeller. This gives rise to a non-homogeneous gas distribution with a high gas accumulation in the recirculation loops and close to the impeller tip. Gas accumulation behind the impeller blades in the low-pressure region is also observed. This is a result of the rotating impeller blades which generate low and high pressure regions, ahead and behind the blade respectively (Ranade and Van Den Akker, 1994). The difference in densities between the gas and the liquid causes the two phases to react differently to the pressure distribution leading to gas accumulation in different regions.

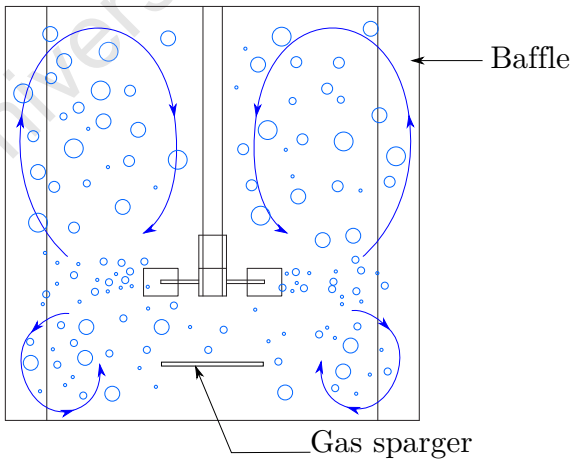

Figure 2.6: Typical motion of gas and its distribution in a stirred tank

Similarly, the spatial bubble size distribution is non-homogeneous. This is mainly because of a complex interaction between local gas hold-up, local bubble size and local turbulence intensity (Bakker and Van Den Akker, 1994). In a region with high gas hold-up the probability of collision is larger and thus leads to a larger coalescence rate. Bubble break-up is

mainly controlled by turbulent kinetic energy contained in eddies of a wave-length of an order of a bubble diameter. The increase in number of bubbles due to break-up also leads to an increase in coalescence due to the increase in bubbles collision rate. Thus, bubble size will depend on the dominating mechanism. The bubble size is small in the outflow of the impeller, with a large energy dissipation rate, and increases along the circulation loops due to coalescence (Bakker and Van Den Akker, 1994; Greaves and Barigou, 1988).

Besides affecting the flow patterns, gas dispersion also influences power draw. The latter is expected to drop with aeration which is a result of the drop in drag on the impeller blade due to the gas cavities formed under gassing condition. It is also believed it can be due to the decrease in density with the occurrence of the gas cavities. The power draw under gassing condition is also used as a measure of gas dispersion, to determine gas hold-up, inter-facial area and mass transfer.

2.4.2 Experimental

2.4.2.1 Gas hold-up

There are different experimental methods to measure gas hold-up. Deglon (1998) determined the gas hold-up by measuring the amount of gas in different regions in the tank. This was achieved by pumping a fixed flow-rate of aerated fluid using a peristaltic pump and de-aerating the fluid in an inverse burette. Gas hold-up was calculated from the pump flow-rate and the volume of gas in the burette.

Newell (2006) used a technique where the increase in height of the aerated fluid compared to the un-aerated fluid was measured. Even though this method is simple, it is not the most accurate.

The measurement of gas-hold up via differential pressure measurements is also commonly used. This method is widely used in semi-batch bubble columns, air-lift reactors and co-current bubble columns (Tang and Heindel, 2006). The pressure measurement can be performed either using manometers or, as in common practice recently, using pressure transducers. These are normally placed close to the vessel walls such that minimum flow disturbance is caused to the flow.

Thus, the average, gas hold-up, $\overline{\varepsilon}$ is given by:

$$\overline{\varepsilon} = \left(1 - \frac{1}{\rho_1}\frac{\nabla p}{\nabla z}\right) + \frac{4\overline{\tau}_w}{\rho_1 D_c g} \tag{2.65}$$

where ∇z is the difference between positions z_1 and z_2 (m)

∇p is the pressure difference at positions z_1 and z_2 (Pa)
ρ_1 is the density of the liquid (kgm^3)
g is the acceleration due to gravity (ms^{-1})
$\overline{\tau}_w$ is the average wall shear stress (Pa)
D_c is the vessel inner diameter (m)

The first term on the right is the hydrostatic head contribution and the second term is the wall shear effects. The latter can be neglected for low superficial liquid velocities, for example when $U_1 = 1$ cms^{-1} in air water systems (Tang and Heindel, 2006). Gas holdup can also be determined by measuring the pressure difference between two levels for an aerated (∇P) and un-aerated liquid (∇P_0) (Dhaouadi et al., 2008). Such that gas hold-up is given by:

$$\varepsilon = \left(1 - \frac{\nabla P}{\nabla P_0}\right) \tag{2.66}$$

2.4.2.2 Bubble size distribution

There are different techniques available for the measurement of bubble size distributions (BSDs) such as the capillary suction probes, photography, phase Doppler anemometry, optical probes and viewing chamber technique (Laakkonen, 2006).

The measurement technique used for the Capillary Suction Probe (CSP) is based on two main parts. The dispersion is firstly sucked into a capillary tube, where bubbles are transformed into cylindrical slugs. Then, the length of the slugs is determined from sensitive light sensors. The latter measures the time taken for the slug to travel known distances between sensors. The accuracy of this technique depends on bubble sizes, since bubble sizes smaller than the capillary tube are not detected properly.

Phase Doppler Anemometry (PDA) is another non-intrusive method used to measure bubble size distributions. This method determines bubble size from the disturbance caused by a bubble. Two laser beams are directed onto a measurement volume, which create a fringe pattern of white and black stripes. The passage of a bubble between the laser beams, causes the light to scatter. This is read by detectors as optical signals which are then converted into electrical signals. The bubble diameter is calculated from the phase difference determined from the detectors.

The photographic method is also commonly used, where images of bubbles are taken using a digital camera. The images are analysed from an image processing software from which the bubble size and shape are measured. This method offers the advantage of measuring both size and shape of projection on a view plane (Zhu et al., 2001).

The viewing chamber technique developed by Grau and Heiskanen (2002) is a combination of a photographic technique and a capillary method. It is also referred to as the viewing chamber technique. This method is only appropriate for a non-coalescing system since coalescence can occur in the sampling tube before reaching the viewing chamber where the photos are taken.

The critical angle of reflection/refraction varies in different phases. This concept is used in the optical probe technique, where the light is sent in optical fibres and detected by a photo-diode. The collected light is converted into a voltage output. The bubble size distribution can be obtained by using a multi-sensor probe (Guet et al., 2005). The accuracy of the technique depends on the orientation of the sensor relative to the direction of the bubbly flow and is thus not convenient for agitated systems.

The accuracy of the bubble size distribution depends on various factors, among which are the measurement techniques and the system investigated (Laakkonen, 2006). The authors compared three techniques; the capillary suction probe (CSP), phase Doppler anemometry and digital imaging (DI). Although, DI and CSP experiments detected the volumetric BSDs and Sauter mean diameter better, none of the techniques detected both number and volume BSDs quantitatively. Pacek and Nienow (1995) also compared different measuring techniques and reported that the video technique is more reliable than the capillary technique since the bubble size is limited by the diameter of the capillary. Other methods have also been compared, for instance Hernandez-Aguilar et al. (2004) showed that the UCT bubble sizer (Randall et al., 1989) which used a capillary method gave similar results to the viewing chamber method.

2.4.3 Numerical

To the author's knowledge no published work has been presented on the CFD modelling of gas-liquid systems for autoclaves. However, due to the similarity of stirred systems with radial impellers this review is based mostly on stirred tanks. Gas-liquid systems have been widely investigated in stirred tanks and the systems were most commonly modelled using the Euler-Euler model and the k-ε model (Gosman et al., 1992; Khopkar et al., 2005; Aubin et al., 2004a; Morud and Hjertager, 1996; Deen et al., 2002; Gentric et al., 2005).

The Euler-Euler method was also used by Khopkar et al. (2005) with the computational snapshot method to model impeller rotation. The general flow field was well predicted; however velocity components were over-predicted in the impeller region. The poor gas hold-up prediction was attributed to the experimental data obtained. A similar method

was used by Ranade and Van Den Akker (1994) as well as Ranade and Deshpande (1999). The authors reported good predictions of velocities and a good qualitative prediction of the gas distribution. Nonetheless, the turbulent kinetic energy correlated poorly with experimental data in some regions of the tank (Ranade and Van Den Akker, 1994).

Lane et al. (2002) using the MRF model also reported a poor gas hold-up prediction although the gas prediction pattern was reasonable. The author reported that specification of bubble drag coefficient could have led to this discrepancy. Various studies applying different techniques have been presented with the aim of improving gas hold-up predictions. The effect of grid refinement and different drag laws were investigated by Deen et al. (2002). The authors reported that trailing vortices observed in single phase flows disappears in aerated systems. A 30% decrease was observed in the maximum velocity in the radial jet in the gas-liquid system. The prediction of the radial velocity profiles showed good correlation to experimental data. However, the authors reported an over prediction of axial velocity profiles. Furthermore, two different drag models were investigated with the C_D expression proposed by Ishii and Zuber (1979) for distorted bubbles and Schiller and Naumann (1933) for spherical bubbles. The authors reported that the drag coefficient was different by a factor of two, thus implying that the choice of the drag model is important. In spite of the difference both models gave the same radial velocities when compared to PIV experimental data. However, the Schiller and Naumann (1933) model poorly predicted the gas axial velocity.

The influence of the turbulence model was investigated by Sun et al. (2006) where the k-ε-A_p turbulence model, an extension of the k-ε was used. The turbulent viscosity for the gas-phase and the liquid phase is related by the algebraic formulation proposed by Hinze-Tchen. The simulation gave a good gas-hold-up prediction in the upper tank, but showed a poor prediction in the region below the impeller. Khopkar and Ranade (2006) used the turbulent correlations developed by Brucato et al. (1998b) but the gas-hold-up was over-predicted. Recently, Scargiali et al. (2007) investigated the effect of grid refinement, lift and virtual mass forces, which are the main non-drag forces. The authors reported that the influence of the non-drag forces on the prediction of the gas distribution were negligible when compared to the drag force exerted on the gas bubbles.

Besides grid size, turbulence model and drag model which account for the poor prediction of gas hold-up, the assumption of uniform bubble size is also believed to contribute to that discrepancy (Gimbun et al., 2009). The bubble size affects the momentum exchange mechanism of inter-phase drag coefficient, which has a direct influence on the prediction of local mean velocities and gas hold-up. The local bubble size distribution was mod-

elled initially using a population Bubble Density Model (BDM) and a one way-coupled approach (Ranade and Van Den Akker, 1994) and recently using a coupled CFD-BDM approach (Lane et al., 2002; Kerdouss et al., 2006; Moilanen et al., 2008). The gas-liquid system in a double turbine stirred tank was investigated by Kerdouss et al. (2006). The system was modelled with a fully unstructured mesh and the effect of turbulence on the drag correlation of Schiller and Naumann was modelled using a similar approach to Bakker and Van Den Akker (1994). The gas hold-up and the bubble size distributions agreed well with the experimental data. Even though the BDM method gives a reasonable prediction this method is thought to be inappropriate (Gimbun et al., 2009) since empirical constants have to be adjusted and are not fully predictive. Moreover, the lack of proper breakage and coalescence kernels makes the model unsuitable where experimental data is not available. The equations relative to the bubble size are written as a function of the Weber number and energy dissipation rate. This is done without modelling the probability and rate of bubble-bubble and bubble-eddy collisions (Petitti et al., 2010).

A full PBM is used to avoid these shortcomings and a coupled CFD-PBM approach with the method of classes or discrete method has been used (Kerdouss et al., 2008; Moilanen et al., 2008; Montante et al., 2008). The approach employed by Montante et al. (2008) gave good prediction for the mean bubble size, but the Sauter mean diameter were under predicted by approximately 50%. Even though the studies by Laakkonen et al. (2007) showed that 80 classes are required to minimize discretization errors when using the multiblock tank model, reasonable predictions were obtained using 13 classes in the work presented by Kerdouss et al. (2008). In order to reduce the computational demand required by the discrete method, the QMOM has been used (Marchisio et al., 2003; Gimbun et al., 2009; Petitti et al., 2010). The work presented by Petitti et al. (2010) showed satisfactory prediction of the BSDs when compared to experimental values.

2.5 Mass Transfer

2.5.1 Theory

There are many theories to describe mass transfer such as the film, penetration, surface-renewal and other theories (Treybal, 1968). In practice most situations occur in a turbulent regime. In such a system, when the flow passes a surface, the gas close to the surface is zero, suggesting that there must be a liquid film close to the surface. The rapid motion of eddies in the turbulent and relatively slower motion in the film give rise to a difference in concentration. This results in a mass transfer process and is usually explained by diffusion.

Fick's Law relates molecular diffusion and concentration difference. In the x-direction it can be written as:

$$J = -D\left(\frac{dC}{dx}\right) \cong \frac{D}{\delta}(C_G - C_L) \tag{2.67}$$

where D is the diffusivity or diffusion coefficient
J is the mass-transfer flux
dC is the difference in concentration
dx, δ is the thickness of the layer

The negative sign implies that diffusion occurs from a region of high concentration to a region of low concentration. The driving force of diffusion is a concentration difference between the gas C_G and the liquid C_L side of the interface.

Since the flux is proportional to the concentration difference for a gas-liquid system, J is given by:

$$J = K\left(C_G - C_L\right) \tag{2.68}$$

where K is the mass transfer coefficient and can be defined as the ratio of the diffusion coefficient to the thickness of the film (Kaskiala, 2006).

For a gas-liquid system K can be split into two parts, a gas and a liquid mass transfer coefficients as given by:

$$k_G = \frac{D_G}{\delta_G} \tag{2.69}$$

$$k_L = \frac{D_L}{\delta_L} \tag{2.70}$$

The mass transfer coefficient K can be written as:

$$K = \frac{1}{\frac{1}{k_G} + \frac{1}{k_L}} \tag{2.71}$$

Thus, if $k_G \gg k_L$, then $K \approx k_L$ and if $k_L \gg k_G$, then $K \approx k_G$. Mass transfer on the liquid side commonly controls gas absorption. This is due to the high diffusivities in the gas phase as well as low diffusivities in the liquid phase and consequently, mass transfer resistance as well as concentration gradients in the gas phase, become negligible (Tatterson, 1991). Therefore,

$$J \cong \frac{D_L}{\delta_L}(\Delta C) \cong k_L(C - C_L) \tag{2.72}$$

where the driving force is a concentration difference between the saturated concentration of the gas in the liquid C_L and the concentration C in the liquid at gas liquid interface.

If the gas dissolves in the liquid without reacting:

$$N_A = k_L \frac{A}{V}\Delta C = k_L a \Delta C \tag{2.73}$$

where N_A (mol/m^{3}s) is the mass transfer rate, a is the gas-liquid inter-facial area A per unit volume of fluid V.

2.5.1.1 Film theory

The concentration difference is the driving force for the mass transfer. Figure 2.7 shows a schematic with concentrations C_{A1} and C_{A2} at the surface and in the turbulent region respectively. The film theory assumes that the concentration follows the broken curve. Mass transfer occurs by molecular diffusion over the film thickness Z_F due to the concentration difference $C_{A1} - C_{A2}$. Furthermore, turbulence is expected to reduce the effective film thickness and therefore increasing mass transfer.

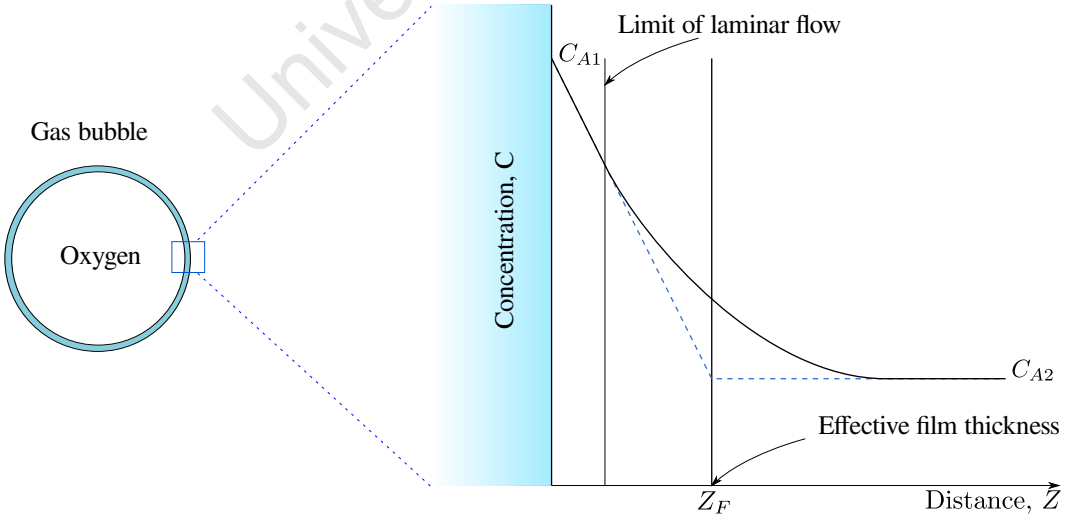

Figure 2.7: Film Theory

The velocity of a fluid surface is not zero (Treybal, 1968) and therefore other theories were

developed based on an unsteady-state form of the Fick's Law given by:

$$\frac{\partial c_A}{\partial \theta} = D_{AB}\frac{\partial^2 c_A}{\partial z^2} \tag{2.74}$$

where θ is the exposure time.

The various mass transfer models, such the Penetration model developed by Higbie (1935) are further described in section 2.5.1.4

2.5.1.2 Diffusion coefficients

The diffusivity in liquids cannot be determined with the same accuracy as for gases (Treybal, 1968). A common basis to estimating diffusion coefficients in liquids is the Stokes-Einstein equation. It is given by:

$$D_{AB} = \frac{kT}{6\pi\mu_B R_A} \tag{2.75}$$

where D_{AB} is the diffusion coefficient of A in B
k is the Boltzmann constant (1.381×10^{-23} J/K)
T is the absolute temperature
μ_B is the viscosity of solvent
R_A is the radius of solute

The equation was developed from a hydrodynamic approach, where the Stokes law for drag on a spherical particle was used as the retarding force. The Stokes-Einstein equation is accurate mainly for systems where the solute concentration is larger than the solvent concentration (Cussler, 1997). Thus, different correlations were developed, such as the Wilke and Chang (1955) expression which starts from the same approach as the Stokes-Einstein equation.

$$D_{AB} = \frac{7.4 \times 10^{-8}(\chi_B M_B)^{\frac{1}{2}} T}{\mu_B V_A^{0.6}} \tag{2.76}$$

where M_B is the molecular weight of solvent B
V_A is the molar volume of solute A
χ_B is the association number of the solvent

2.5.1.3 Correlation for k_La

Various studies have been presented on the correlation between the overall mass transfer coefficient, k_La, power consumption, volume of liquid and the superficial gas velocity. However, no consistent correlations have been developed. This is because the volumetric mass transfer is highly affected by factors such as vessel geometry, the fluid property and the experimental method used to determine k_La.

The most common correlation for the volumetric mass transfer, k_La is given by :

$$k_La = a\,(U_g)^b \left(\frac{P}{V_L}\right)^c \tag{2.77}$$

where a is a constant
P_g is the gassed power consumption, (W)
V_L is the volume of the liquid, (m^3)
U_g is the superficial gas velocity (ms^{-1})
b, c are exponents

Among the vast number of correlations available another variant is commonly used, where a ratio (Q/V_L) is used instead of U_g (Schlüter and Deckwer, 1992). In addition, there have also been a wide variety of exponents that have been used with equation 2.77 and Table 2.2 shows some of the exponents obtained for different systems investigated. The study presented by Moo-Young and Blanch (1981) gives a good summary of the exponents obtained. The exponents showed a large variation; $0.4 < b < 0.7$ and $0.4 < c < 0.8$ and likewise for the constant a.

Table 2.2: k_La Correlation

a	b	c	Agitator	Reference
Water				
0.026	0.5	0.4	-	van't Riet (1979)
0.025	0.5	0.4	6-bladed Rushton turbine	Moo-Young and Blanch (1981)
0.00495	0.4	0.593	6-bladed Rushton turbine	Linek et al. (1987)
0.01	0.4	0.475	Various agitators	Moo-Young and Blanch (1981)
0.0062	0.51	0.66	Various agitators	Vasconcelos et al. (2000)
Electrolyte solutions				
0.002	0.2	0.7	-	van't Riet (1979)
0.0018	0.3	0.7	6-bladed Rushton turbine	Moo-Young and Blanch (1981)
0.002	0.4	0.475	Various agitators	Moo-Young and Blanch (1981)

2.5.1.4 Mass transfer models

In multiphase systems the mass transfer coefficient, k_L, is estimated mainly because of the difficulty in measuring the values. Kulkarni (2007) gives a comprehensive review of mass transfer models for gas/liquid interfaces. Some of the models are summarised below.

The Penetration Theory presented by Higbie (1935) is given by:

$$k_L = 2\sqrt{\frac{D_L}{\pi \tau_e}} \tag{2.78}$$

where τ_e is the exposure time (s)
D_L is the diffusivity of gas in liquid (m^2s^{-1})

The mass transfer across the liquid film is considered unsteady and age-distribution is considered constant with this model.

Higbie (1935) recommended that the exposure time can be assumed to be d_b/u_{slip}. The model is also known as the slip penetration model (Wang and Wang, 2007; Gimbun et al., 2009) and is given by:

$$k_L = \frac{2}{\sqrt{\pi}}\sqrt{\frac{D_L u_{slip}}{d_b}} \tag{2.79}$$

where d_b is the bubble diameter (m)
u_{slip} is the bubble slip velocity (ms^{-1})

Danckwerts (1951) refined the penetration model such that:

$$k_L = \sqrt{D_L s} \tag{2.80}$$

where s is the fractional rate of surface-element replacement. Equation 2.80 assumes that mass transfer is an unsteady process and does not take random age distribution and eddy distribution into consideration

Lamont and Scott. (1970) calculated s using the Kolmogorov's theory of isotropic turbulence to obtain the eddy cell model (Dhanasekharan et al., 2005; Kerdouss et al., 2008; Moilanen et al., 2008; Gimbun et al., 2009).

$$k_L = F\sqrt{D_L}\left\{\frac{\varepsilon_L \rho_L}{\mu_L}\right\}^{0.25} \tag{2.81}$$

where F is a model parameter
ε_L is the water turbulent dissipation rate (m^2s^{-3})
ρ_L is the density (kgm^{-3})
μ_L is the viscosity ($kgm^{-1}s^{-1}$)

A steady state process is assumed for Equation 2.81 and highly mobile eddies contribute the most to mass transfer.

2.5.2 Experimental

Different techniques have been presented in literature to measure the mass transfer coefficient in gas-liquid systems. The methods can be grouped into three main categories; Sulphite Oxidation Method (SOM), Dynamic Pressure-step Method (DPM) and Gassing-Out Dynamic Method (GOM) (Blažej et al., 2004).

The SOM method is a chemical method where sodium sulphite (Na_2SO_3) is oxidised in an aqueous solution. This reaction is normally catalysed with a cobalt salt, which leads to the complex formation of a cobalt ion and ensures a zero liquid oxygen concentration. The volumetric mass transfer coefficient is determined from an empirical correlation which is dependent on the concentration and volume of the sulphite as well as steady state oxygen concentration and time.

The DPM method is performed by causing a sudden change in pressure. Blažej et al. (2004) used a ± 15 kPa change, which results in a change in oxygen concentration in all bubbles in the dispersion. The volumetric mass transfer was then determined from the pressure and liquid oxygen concentration.

The principle behind the GOM method is the desorption of oxygen from the liquid phase in the gas-liquid system by using nitrogen. Dissolved oxygen (DO) probes are used for the measurement of the concentration of oxygen. The rate of change of oxygen is given by (Kerdouss et al., 2008):

$$\frac{dC_L}{dt} = k_L a \left(C^* - C_L\right) \tag{2.82}$$

where C^* is the saturation concentration. According to Henry's Law:

$$P_{O_2} = H \cdot C^* \tag{2.83}$$

Considering that the initial concentration = 0. Then,

$$\ln\left(\frac{C^* - C_L}{C^*}\right) = -k_L a t \tag{2.84}$$

Thus, the volumetric mass transfer coefficient, $k_L a$, is determined by plotting the left-hand side of the equation against time.

Moilanen et al. (2008) employed a dynamic technique using a polarographic oxygen probe in a stirred vessel. The volumetric mass transfer coefficient was calculated from dissolved

oxygen (DO) measurements. A similar technique was used by Kerdouss et al. (2008). Optical sensors were also used in bubble column reactors by Terasaka et al. (2008) and Dhaouadi et al. (2008).

Kulkarni and Joshi (2004) used different methods to determine k_L values, the true mass transfer coefficient as referred to by the authors. A chemical method of oxidation of sodium sulphite was used in the determination of k_L. The mass transfer coefficient was also determined using information on eddy life distribution. The latter was determined from the analysis of velocity-time data from LDA measurements.

Kaskiala (2006) reported the effect of impeller speed and volume flow-rate on the volumetric mass transfer coefficient, k_La, in a 108 l vessel. The increase in impeller speed and gas flow-rate resulted in an increase in k_La due to an increase in gas hold-up and gas-liquid contact area. The k_La values varied between 2.17 and 12 $\times$ 10^{-3} s^{-1}. The effect of impeller speed on the mass transfer coefficient, k_L, was also investigated. The increase of surface removal and turbulence at the interface with increase in impeller speed was found to result in an increase in k_L. The mass transfer coefficient did not seem to be affected when the hydrostatic pressure was increased from 200 to 800 Pa. An increase in electrolyte, H_2SO_4, concentration led to a reduction in the mass transfer coefficient. Similar, effects were seen when NaCl and $ZnSO_4$ were used. The k_L values were lower for water when compared to the electrolyte solution. Linek et al. (2004) reported an increase in the k_La values with the addition of an electrolyte in water. The latter reduced the rate of bubble coalescence resulting in an increase in k_La up to a maximum. The k_La values for a 0.5 and 0.2 M Na_2SO_4 solution did not differ. Zhu and Wu (2004) investigated the effect of temperature on the volumetric mass transfer rate in a mechanically agitated tank for an air-water system. The authors reported that gas flow-rate and the impeller speed did not have a major effect on the saturation oxygen concentration. It was observed that there was an increase in k_La with temperature in the range of 18-60°C. However, a drop in k_La was reported for temperatures above 60°C and was attributed to a decrease in the gas hold-up. Moreover, it is noted that even though electrolytes reduce k_L and increase a by increasing the gas hold-up and decreasing the bubble size by a large amount so that k_La increases, occasionally k_La has been found to decrease (Harnby et al., 1992).

There are various types of impeller systems that are used in autoclaves. Klepper (2000) reported four cases as shown in Figures 2.8(a)-2.8(d). The vortex gassing method as shown in Figure 2.8(a) was reported as the least efficient method of gas mass transfer. The interfacial area is the sum of the pulp-gas interface plus surface area of bubbles. The gas enters from the headspace of the autoclave and due to the presence of water vapour and other

by-product gases the elemental gas concentration is low. Figure 2.8(b) depicts the surface gassing method. The inter-facial area for this system is the surface area of the liquid-gas interface. The bottom impeller is downward pumping and top impeller upward pumping creating a surface flow. The water at the interface is continuously replaced by unsaturated liquid creating a concentration gradient. This gives rise to a higher mass transfer coefficient than that created by vortex gassing.

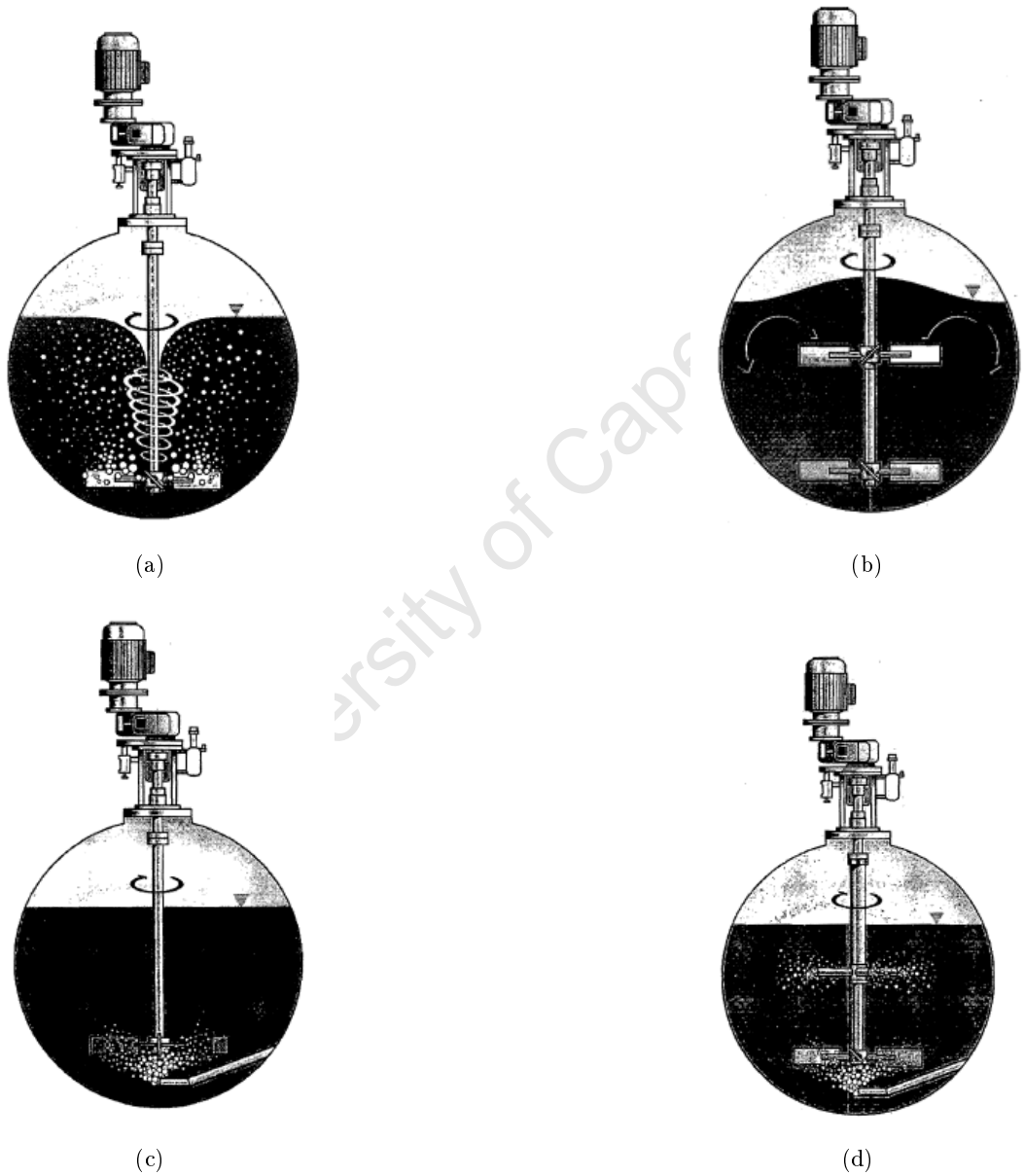

(a) (b)

(c) (d)

Figure 2.8: (a) Vortex gassing impeller, (b) Surface gassing impeller, (c) Submerged gas entry with flat blade turbine,(d) Submerged gas entry with pitched blade turbine and gassing impeller (Klepper, 2000)

The submerged gas entry technique as illustrated in Figure 2.8(c) is considered as the most

widely used method in hydrometallurgy. The gas enters the system via a sparger located under or near the impeller. The inter-facial area is a combination of the surface area of bubbles and surface area of the pulp-gas interface. A pitched blade impeller or a flat blade turbine is normally used, where the flat blade impeller produces finer bubbles due to high shear radial flow. The submerged entry with gassing impeller as shown in Figure 2.8(d) method uses a similar technique as the submerged gas entry system, where both a gassing impeller and a pitched blade impeller are used.

Five different scenarios were compared by Klepper (2000), namely the vortex gassing, surface gassing, submerged entry with a pitched blade turbine, submerged entry with a flat blade disc turbine and the gassing impeller method. The k_La experimental values, obtained from lab scale tests in a 50 l vessel, showed that the submerged entry with the flat blade disc turbine was the most efficient with a relative k_La of 2300 and the vortex gassing system with pitched blade turbine the least efficient with a relative k_La of 250.

2.5.3 Numerical

The gas-liquid mass transfer coefficient, k_La, for different gas-liquid systems has been simulated by separately modelling k_L and a (Wang and Wang, 2007; Dhanasekharan et al., 2005; Kerdouss et al., 2008; Moilanen et al., 2008; Gimbun et al., 2009). In most cases simple approaches were used to model the local mass transfer coefficient. This was found to be suitable since the systems involved poorly soluble gases, no chemical reactions and small differences in the diffusivities of the components (Moilanen et al., 2008).

Wang and Wang (2007) predicted k_La in bubble columns using both the eddy cell and slip penetration models. Both methods predicted reasonable k_La for a wide range of superficial gas velocity with a small change to model constants. Furthermore, it was reported that the models showed good correlation to experimental data in high turbulence range but a deviation between the two models were observed in low turbulence range. The authors suggested that if the effects of gas hold-up and turbulent energy dissipation rate on bubble size and bubble slip velocity are taken into account, the slip penetration model can be used in a wide range of applications.

Moreover, various numerical studies have been undertaken to numerically model the gas-liquid mass transfer in stirred tanks. Bakker and Van Den Akker (1994) modelled k_La using mass transfer coefficient correlation proposed by Kawase and Moo-Young (1990) along with the in-house code GHOST!. The bubble size did not have a major influence on k_L. It was mainly dependent on local turbulent intensity since the main resistance for mass transfer is on the liquid side. The highest k_La values were observed in the outflow of the

impeller and was relatively low in the bulk region. Moilanen et al. (2008) investigated the effect of impeller geometry on gas-liquid mass transfer using two different population balance methods, namely multiple size groups (MUSIGs) and bubble number density (BND). The mass transfer coefficient was simulated using the eddy cell model. Lower k_La values were predicted by the BND method than MUSIGs. Kerdouss et al. (2008) simulated the gas-liquid mass transfer using the eddy cell model using bubbles with both constant size and a size distribution. The authors reported that the population balance method gave better k_La predictions and got the desired accuracy with 13 classes. The eddy cell model and the slip penetration model were used by Gimbun et al. (2009) to simulate the local k_La values. The eddy cell model, which is more sensitive towards high dissipation rates, predicted a higher k_La value around the impeller region. The slip penetration model, which is dependent on the bubble size, predicted a higher local k_La in the bulk region.

To the author's knowledge there has been no published work on numerically modelling mass transfer using the above-mentioned methods. Nicolle et al. (2009) modelled the first compartment of an Activox® autoclave and k_La values were determined from an empirical correlation based on P/V. The first compartment was designed to leach approximately 77% of the nickel mass leached across the autoclave. The reactions in that compartment require the greatest oxygen demand and agitation. Thus, the mass transfer of oxygen to the solution was crucial to the leaching efficiency. A 3-D model of the first compartment with three impellers was simulated. The fluid in the system was found to be well mixed and a good mixing between the solids and dissolved oxygen was expected.

2.6 Summary

Hydrodynamics, gas dispersion and mass transfer have been studied extensively, both numerically and experimentally for stirred tanks. There is still on-going work to better understand flow in stirred vessels with two phase systems both experimentally and numerically. There is still on-going work on flow visualization (Hu et al., 2012) and CFD modelling of turbulence using LES (Roy et al., 2010). Similarly, there is substantial work on the two-phase modelling, especially with the population balance models (Buffo et al., 2012; Selma et al., 2010). However, numerical modelling and even experimental studies on autoclaves have been very scarce. Only recently, Nicolle et al. (2009) presented a study predicting fluid flows in the first compartment of an autoclave. Mass transfer was determined using a power law correlation rather than using the prediction of k_L and a, which provides a better description of k_La. Due to the scarcity of research studies on autoclaves a summary of numerical and experimental findings based on stirred tanks is presented in

the following sections.

The first studies were based on flow visualisation, which started with relatively simple photographic methods to more advanced techniques such as PIV. The flow patterns, velocity profiles and turbulence were analysed for various scenarios. The position of the impeller affects the flow pattern, if off-centered a vortex is expected to form. A similar phenomenon occurs in systems without baffles. The bottom clearance of the impeller also influences the flow pattern. The double-loop flow structure observed in the cylindrical tanks with a radial impeller changes to a single-loop structure as the bottom clearance is reduced.

With the development of faster computers numerical modelling using CFD has been used extensively for the prediction of hydrodynamics for single phase systems in stirred tanks. Coupled with advanced experimental techniques the CFD models were validated. Several numerical methods were developed and enhanced to simulate the different flow phenomena. MRF and sliding mesh models were the most commonly used methods. The k-ε model was widely used to simulate the turbulent flow regime. From the various studies presented reasonable predictions were obtained for mean velocity and power draw. The main discrepancies were in the prediction of the turbulence parameters. However, these were attributed to the influence of the order of discretisation schemes and the grid resolution used rather than a shortcoming of the turbulence model.

In the last couple of decades efforts have been made in the development of models for gas-liquid systems. Simultaneously, experimental techniques were developed to provide a better understanding of gas-liquid systems. Different methods were developed to measure gas hold-up. The simplest method being the measurement of the change in liquid level in the tank. Tomography and differential pressure probes were also used. Bubble size distribution was measured using various techniques such as the Phase Doppler Anemometry, photographic methods, optical probes, capillary suction techniques. However, due to the highly agitated flow in stirred tanks photographic and video methods were the most reliable techniques. The prediction of flow for gas-liquid systems for stirred tanks has been thoroughly investigated. The simulations which are commonly based on the Euler-Euler model gave good qualitative predictions of gas dispersion but some quantitative discrepancies have been observed. Different studies have been conducted investigating the effects of grid resolution, turbulence model and drag model on gas hold-up. The effect of the drag model has been reported to significantly affect gas hold-up predictions. Bubble size which is directly related to the drag force is believed to be the main reason for this shortcoming. The use of population balance models enhanced the accuracy of the predictions of gas

hold-up and also simulated local bubble size which are crucial when modelling gas-liquid mass transfer. The discrete method and variants of the method of moments were the models that were most commonly used. The variants of the method of moments are the less computationally expensive compared to the discrete method which sometimes require a large number of classes. Moreover, in some cases it was reported that the breakage and coalescence models had to be modified to accurately predict bubble size distribution.

The modelling of gas-liquid mass transfer has been done by separately simulating k_L and a. There are two models, namely the slip penetration model and the eddy cell model that have been most widely used. The eddy cell model has been found to be more sensitive to the turbulent energy dissipation rate. The model has been found to give a higher k_La values in the impeller region but with lower values in the bulk region. In addition to the numerical work, experimental research has been conducted to measure k_La in stirred systems. The influence of operating conditions were investigated in different systems, either in water or electrolytes. The electrolytes generally led to an increase in the k_La values due to an increase in a.

Based on published work it is clear that there is a lack of data available on gas-liquid mass transfer in autoclaves. Mass transfer has been highlighted to be highly dependent on hydrodynamics and gas dispersion and therefore the need to understand the different flow phenomena in autoclaves is important. The current study is aimed at investigating hydrodynamics, gas dispersion and mass transfer in a pilot-scale autoclave. CFD models, validated experimentally, will be developed and used for predictions.

3 Experimental

The experimental details used for this study are presented in this chapter. The latter begins with a description of the pilot-scale experimental vessel used, as presented in Section 3.1. The following two sections, 3.2 and 3.3, cover the experimental programme and measurements used to characterise hydrodynamics, gas dispersion as well as mass transfer. Hydrodynamics was characterised in terms of velocity flow field and power draw. These were measured by using PIV measurements and a load cell respectively. Gas dispersion was characterised in terms of bubble size and the measurements were made using an Anglo Platinum American bubble sizer. A dissolved oxygen probe was used to determine gas-liquid mass transfer coefficient, k_La. The experimental procedures used and analysis made for each measurement are described. Finally, experimental errors are discussed in Section 3.4.

3.1 Autoclave

The vessel used for this study was based on the first compartment of an 80 m^3 Sherritt Gordon horizontal autoclave. The tank dimensions and operating conditions are based on these used at the Anglo American Platinum RMBR plant for the secondary leach autoclave. The pilot-scale vessel is shown in Figure 3.1.

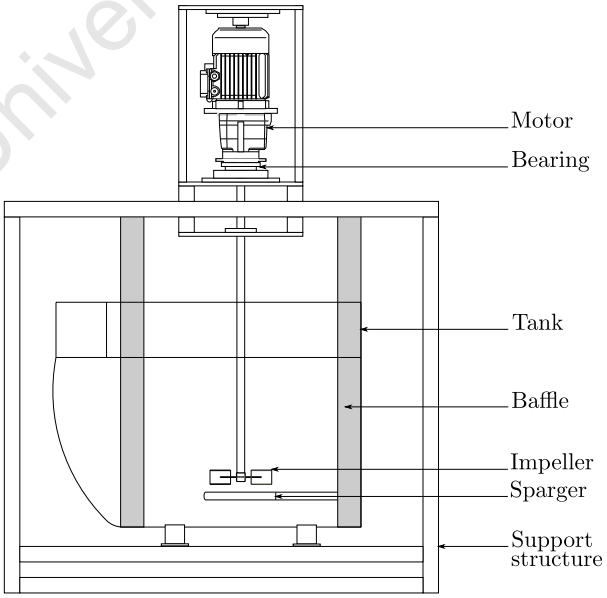

Figure 3.1: Pilot-scale vessel of first compartment of an autoclave

The first compartment was scaled down by a factor of seven which resulted in a 60 l

vessel. A capacity of 60 l was chosen as it was large enough to have similar hydrodynamic attributes of industrial autoclaves and small enough to conduct laboratory characterisation experiments for CFD validation. The size of the vessel was close to the 50 l vessel used by Klepper (2000) to conduct experimental work for mass transfer measurements.

3.1.1 Tank

The perspex tank had a capacity of 60 l, with two baffles, one on each sides as shown in Figure 3.1.

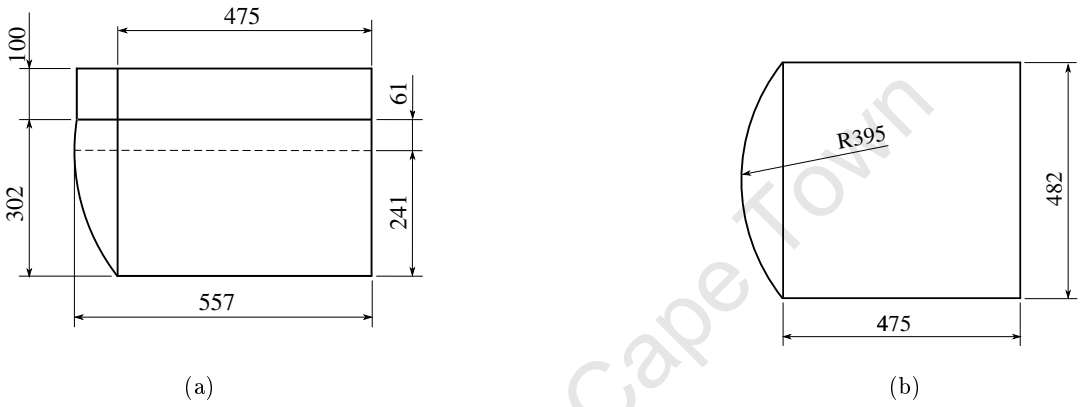

Figure 3.2: (a) Front view, (b) Top view

The dimensions of the tank, in mm, are as given in Figures 3.2(a) and 3.2(b), with the front view of the vessel (viz. Figure 3.2(a)) and the top view (viz. Figure 3.2(b)). The baffles were 15 mm × 50 mm in cross-section.

3.1.2 Aeration System

A diamond shaped sparger, placed at a distance of 48 mm below the impeller, was used. Oxygen gas was supplied through the sparger. The latter had four equi-distant 2 mm holes drilled on its four sides. The volumetric flow-rate was controlled with a rotameter flowmeter.

Figure 3.3: Sparger

Figure 3.3 shows a schematic of the diamond shaped sparger used.

3.1.3 Impeller

The impeller was based on a six-bladed Smith turbine and was powered by a 1.5 kW AC motor mounted on a gear box. The motor speed was controlled with a speed control box and confirmed with an optical tachometer.

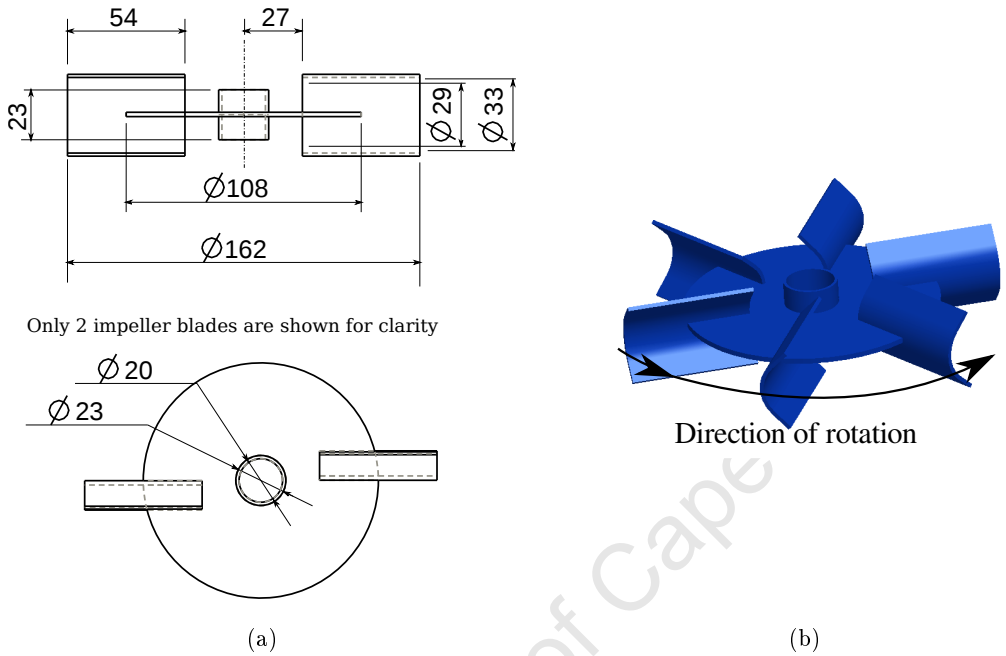

Figure 3.4: (a) Impeller dimensions, (b) Impeller

Figure 3.4(b) shows the Smith turbine used, with curved blades in the form of a half cylinder. The main dimensions in mm are as depicted in Figure 3.4(a). The impeller had a 102 mm clearance from the bottom. The direction of rotation of the impeller is shown in Figure 3.4(b).

3.1.4 Temperature Control

A heating element was used to heat the liquid to the required temperature and was controlled by a thermostat. The heating element was then removed from the system to avoid any disturbance of the fluid flow. This resulted in changes in temperature during experiments. The changes varied between 1 and 2°C depending on the experimental conditions but led to negligible differences in the data measurements.

3.2 Experimental Programme

An experimental programme was designed to characterise hydrodynamics, gas dispersion and mass transfer. The system was investigated at different conditions, including impeller

speed, gas flow-rate, temperature as well as two different liquids. Sections 3.2.1 and 3.2.2 cover the experimental conditions and variables in further detail.

3.2.1 Conditions

The experimental conditions are outlined in Table 3.1. Two systems were investigated for this research study; single phase and gas-liquid systems. The single phase experiments were mainly used for the validation of hydrodynamics for the CFD models, which is common practice for modelling of mixing vessels. The vessel was filled with 60 l of water and the latter was used to facilitate PIV measurements in the clear perspex vessel. Furthermore, the system was operated at atmospheric pressure and ambient temperature. The two main conditions used were gas flow-rate and liquid medium as tabulated in Table 3.1.

Table 3.1: Experimental conditions

Parameter	**Conditions**
Volume	60 l
Medium	Water & Synthetic leach liquor
Gas	Oxygen
Gas flow-rate	4.37 and 7.8 $lmin^{-1}$

Two different liquid media, water and synthetic leach liquor, were used to investigate the gas-liquid system. The synthetic leach liquor is a solution of copper, nickel ions and sulphuric acid mimicking the solution used in the autoclave at the plant. This was mainly used to investigate the effect of the ions on the mass transfer process. The synthetic leach liquor was prepared from the composition given by Anglo American Platinum (Table 3.2).

Table 3.2: Solution and solids composition

	Cu	**Acid**	**Ni**
Solution	70-90 g/l	10-15 g/l	40-60 g/l
	Cu	**Ni**	**Fe**
Solids	20-35%	5-7%	5-15%

The lower concentration was taken such that the solution prepared from the hydrated nickel sulphate, hydrated copper sulphate and sulphuric acid had the following composition. The leach liquor had 40 g/l Ni, 70 g/l Cu and 10 g/l H_2SO_4. The lower concentration

was used avoid to precipitation. The mass of copper and nickel from the hydrated solute, which could have changed by hydration, were checked by performing ion analysis using an Atomic Absorption Spectroscopy (AAS) technique.

Oxygen gas was supplied at two flow-rates, 4.37 and 7.8 lmin^{-1}. Gas flow-rates are typically scaled on either a constant flow-rate per unit area (superficial gas velocity) or per unit volume. Here the gas flow-rate (4.37 lmin^{-1}) was determined by scaling on a constant flow-rate per unit volume basis. This resulted in a substantially lower superficial gas velocity than in an industrial autoclave. However, scaling on a constant superficial gas velocity would have resulted in very high flow-rates well above the operating window of the laboratory vessel. A second flow-rate, 7.8 lmin^{-1}, was chosen such that it was near double the first one but it was limited by the flow-meter available. The effects of an increase in superficial gas velocity on gas dispersion and mass transfer are explained in Chapter 5 as well as Sections 6.2 and 6.3.

3.2.2 Variables

There were two major experimental variables that were used for the study; impeller speed and temperature. Impeller speed is known to have an effect on hydrodynamics, gas dispersion and consequently mass transfer. Temperature was mainly used to investigate its effect on mass transfer.

Impeller speed has a direct effect on the fluid flow in mixing vessels. Flow patterns and subsequent micro phenomena such as turbulence are directly affected. Hydrodynamics in turn influences gas dispersion, both by affecting bubble size and gas hold-up. Consequently, those two factors play a major role in controlling mass transfer. Therefore, the impeller speed was varied to investigate and understand those phenomena in the pilot-scale vessel. The choice of the impeller speeds was initially based on the speed of the actual industrial autoclave. The maximum impeller speed of 395 rpm was determined by scaling on a constant power per unit volume basis. The flow patterns were found to be influenced by the impeller speed. A transition point was observed at around 225 rpm where the free surface collapsed due to the formation of a vortex causing air to be sucked in by the impeller. The resulting entrainment was however not excessive. This is further explained in Section 4.4.2. Thus, operating conditions with impeller speed below 225 rpm were also investigated. A minimum impeller speed of 150 rpm was chosen. At this speed even though the system provided a minimum amount of mixing, sufficient gas dispersion could be observed and satisfactory measurements could be made. Therefore, measurements were made at 150, 200, 225, 250, 300, 350 and 395 rpm.

Temperature was varied for two main reasons; to investigate its effect on mass transfer and so that near operating conditions in autoclaves could be replicated. Temperature affects mass transfer, k_La in two ways; on the one hand by affecting the bubble size, therefore a and on the other hand k_L. To investigate the effect of temperature three different temperatures were chosen. Ideally, to mimic the conditions in the autoclave near boiling point temperatures should have been considered. However, the maximum temperature was limited by the solubility of oxygen, which beyond 70°C was too low to be measured accurately using the Gassing-Out Dynamic method with a DO probe. The response time was too small to obtain accurate data. The maximum temperature was also limited by the mechanical integrity of the perspex vessel, which above 70°C started to soften. The lowest temperature was at 25°C. The third and intermediate temperature chosen was at 50°C.

3.3 Experimental Measurements

The different experimental measurements conducted to investigate the three flow phenomena and to validate the CFD models are covered in the following sections. These include, measurements of power draw and velocity flow field which were used for the characterisation as well as validation of hydrodynamic properties. In addition, bubble size measurements were made to investigate gas dispersion in the vessel and also to validate the two phase CFD model. Finally, measurements of gas-liquid mass transfer were performed. The details of the experimental techniques used and analysis performed are discussed in the following sections.

3.3.1 Power

Power input was calculated from the product of torque experienced by the motor, which occurs due to the inertia on the impeller blades, and the impeller speed.

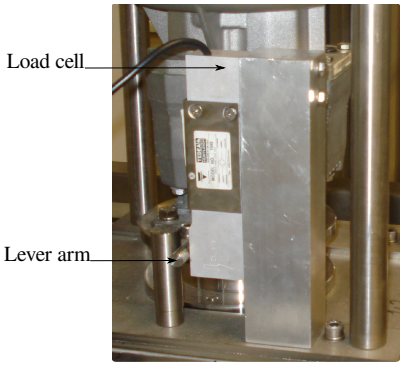

Figure 3.5: Load cell and torque arm

The motor was mounted between bearings to allow free rotation and any torque experienced resulted in a rotation. The torque exerted was determined from a load cell, which measured the resultant moment applied on a lever arm fitted to the motor. The set-up used is shown in Figure 3.5.

3.3.2 Velocity

A 2-D PIV system was used to measure velocity vector fields. The main objective of this method is to determine velocity of suspended particles in a fluid in motion. The velocity is calculated based on measured displacement of particles over a known time interval. The movement of particles are detected over an area of a flow field that is illuminated by a light sheet generated by a laser. The light sheet is pulsed to produce a stroboscopic effect that freezes the movement of the seeding particles over time. The particle point cloud in two sequential frames are recorded with two cameras positioned at right angle to the light sheet. The data is processed by dividing the frames into interrogation areas. The interrogation areas from the two frames are correlated and the distance moved by the particle cloud within the interrogation area is calculated. Thus an average particle displacement vector is obtained. The velocity is then calculated by dividing the distance by the known time interval between frames. This method is used to determine the velocity vectors in each interrogation area and the interrogation areas are combined to form a vector field.

3.3.2.1 Experimental equipment

A Dantec Dynamics PIV system was used, which can either be used for 3-D or 2-D velocity measurements. However, due to the inaccuracies that can be involved with the 3-D stereoscopic system coupled with the curved surfaces of the vessel, the 2-D approach was chosen. There are four main pieces of equipment that are used in the PIV system. The laser to generate a light sheet, cameras, seeding particles and postprocessing equipment as well as software.

3.3.2.2 Experimental procedure

The velocity measurements were done on 3 different planes as shown in Figure 3.6(a). Plane 1 was at 10 mm away from the impeller tip or 91 mm from the centre of the shaft, Plane 2 at the centre of the shaft and Plane 3 at 119 mm away.

The calibration is the first step in the PIV measurement. This is done by placing a target on the plane where the laser will be shone. A photo of the target is taken and is analysed by the software. The target consists of equally spaced holes and calibration aims at aligning these holes with a grid as seen by the software. The grid, coloured in

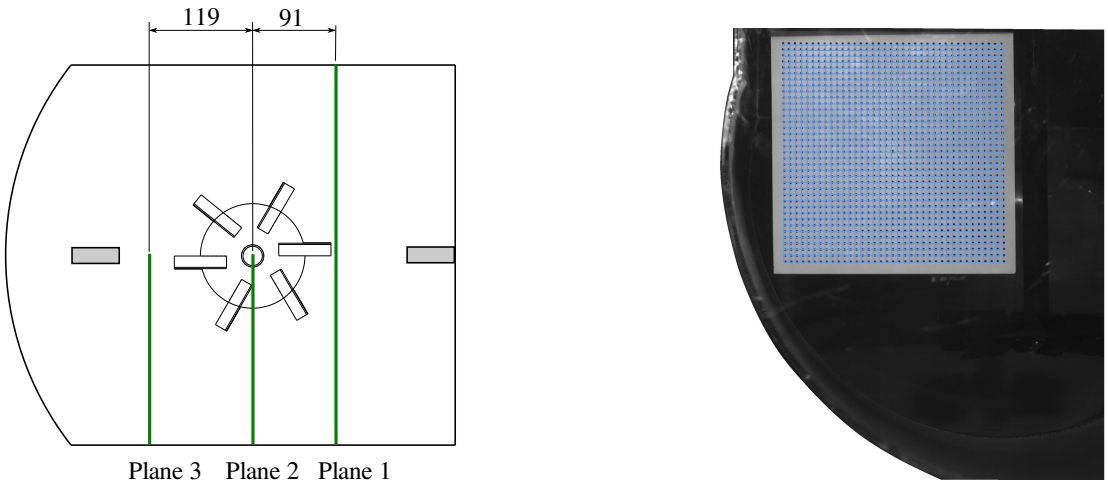

Figure 3.6: (a) Laser and camera position, (b) PIV Calibration

blue, is illustrated Figure 3.6(b). The accuracy of the PIV measurement depends on the calibration. This means that data which is in a region where the grid aligns exactly on the holes is the most accurate.

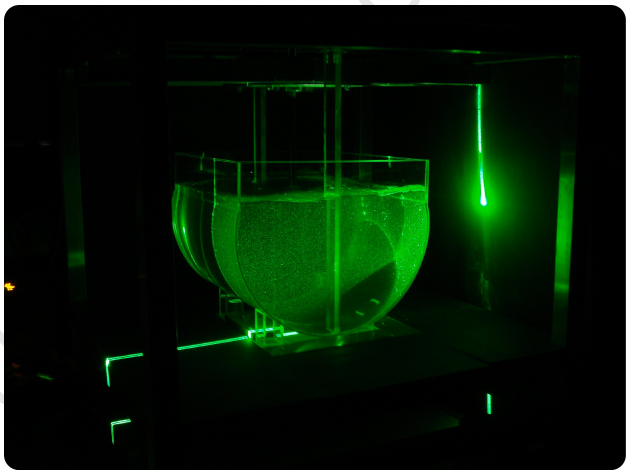

Figure 3.7: Laser sheet with particles

Then the flow was seeded with Polyamid Seeding Particles (PSP) with a diameter of 50 μm. A seeding concentration of 5 g/l was used for the experiments. A Nd:YAG doubled pulsed laser beam was used to create a 1 mm thick light sheet. Figure 3.7 shows a laser sheet with illuminated particles on Plane 1. The laser was synchronised with the CCD cameras, with a resolution of 1024 $\times$ 1028 pixels, placed at right angle to the light sheet. As outlined in Section 4.4.2 at about 225 rpm surface vortices, which allowed air to be sucked into the impeller, occurred. The vortex created a void region with no particles

and led to inaccuracies in the measurement. Therefore, three impeller speeds were chosen for the PIV measurements and they were at 150, 200 and 250 rpm. The exposure time of the laser was determined from preliminary experiments for each impeller speed and for each plane. Based on the results, the exposure time delay for Plane 1 was set at 3000 μs, for Plane 2 at 1000 μs and Plane 3 at 3000 μs. For each measurement set, 150 image pairs were taken and were found sufficient to provide accurate data.

3.3.2.3 Data analysis

The DANTEC Dynamic Studio post-processing software was used to analyse the data. The analysis was performed by initially dividing the captured images into interrogation areas of 32 $\times$ 32 pixels. A mask was defined to eliminate the unimportant regions on the images and then a vector mask was performed to remove any erroneous velocity vectors. A peak validation was then performed to select velocity vectors that are in an allowable range. Finally average flow fields were obtained by time averaging data over 150 images. The data was further post-processed in Paraview 3.10.1 to extract velocity profiles.

3.3.3 Bubble Size

Bubble size measurements were made at two positions in a region close to the impeller and in the bulk region using an Anglo American Platinum bubble sizer (AAPBS). The experimental techniques and procedures are explained in detail in the following sections. It should be noted that in industrial autoclaves oxygen mass transfer occurs continuously because of the presence of minerals, which consequently leads to a decrease in bubble size. However, this would not be observed in the experimental-set, as this was saturated.

3.3.3.1 Experimental equipment

A photographic technique was used for bubble size measurements. The measurements were performed with an Anglo American Platinum Bubble Sizer. The apparatus, as shown in Figure 3.8(b), uses a 12.0 mega pixels FUJIFILM digital still camera. The bubbles rise up a collection pipe, which is attached to the connector and immersed in the liquid via the inlet point, as shown in Figure 3.8(a). The bubbles rise up the collection pipe until they reach the viewing chamber, which is in front of the camera housing. The camera fitted inside the camera housing is used to manually capture images of the bubbles. The images are post-processed with a software application to determine the bubble size (Taute, 2006).

3.3.3.2 Experimental procedure

The samples were taken at two different positions, in the impeller stream and in the bulk region. Samples in the impeller region were taken at a distance of 120 mm from the bottom

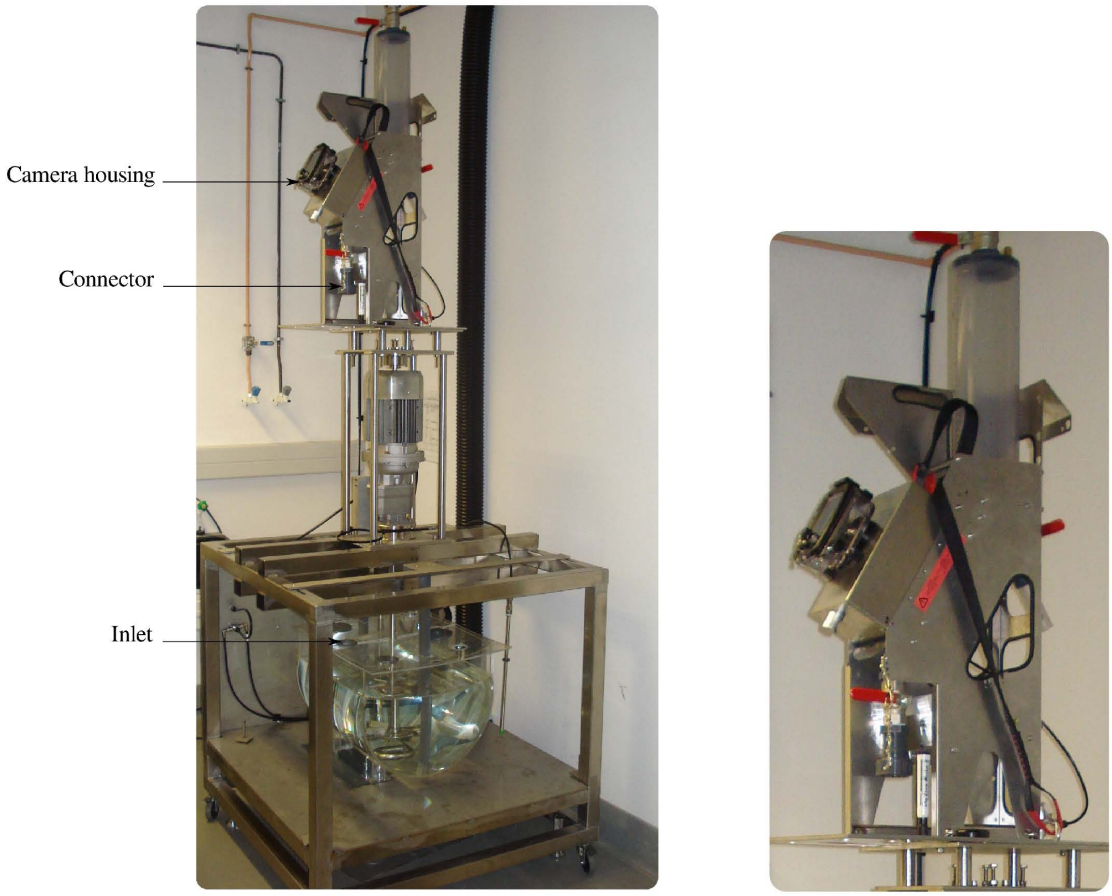

(a) (b)

Figure 3.8: (a) Bubble sizer Set up, (b) Anglo Platinum Bubble Sizer

of the vessel and 205 mm for the bulk region. After the system was allowed to stabilise a total of 100 photos at intervals of 5 s were taken for each measurement. The number of bubbles determined for each experimental run depended on the conditions, but an average of 600 were measured per run.

3.3.3.3 Data analysis

The AAPBS image processing software was used to size bubbles, where the size is evaluated from the known size of the glass plate in the viewing chamber. A MATLAB (The Mathworks, R2010a) script was used to determine the number of bubbles in each photo. Figure 3.9 shows an image, with bubbles, that was taken at 350 rpm, at ambient temperature and at a flow-rate of 7.8 lmin^{-1}.

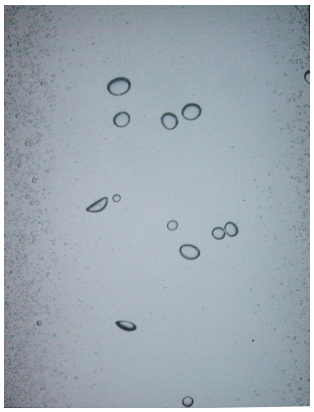

Figure 3.9: Typical image from bubble sizer

3.3.4 Gas Hold-up

Gas dispersion is commonly characterised in terms of gas hold-up. However, due to the low superficial gas velocity used gas hold-up was too low, less than 1%, to be measured accurately. There are two common techniques that are normally used to determine gas hold-up experimentally for mixing vessels. Gas hold-up is either determined by measuring the volume change due to gas or by measuring pressure differences which arises as a result of a change in density of a fluid in the presence of gas. However, none of these methods was convenient. The change in volume of the fluid was too low to be accurately measured. Moreover, this method is only convenient when the free surface is flat and stationary. It was observed that with the autoclave the free surface moved by a fair amount as a result of agitation.

Piezoelectric transducers are also used to measure pressure changes to determine gas hold-up. However, due to the small amount of oxygen gas in the vessel and the high agitation rate the pressure measured by transducers would have been mainly due to dynamics pressures. This would have resulted in erroneous and inaccurate gas hold-up measurements.

3.3.5 Volumetric Mass Transfer Measurements

Volumetric mass transfer values were determined using a Gassing-Out Dynamic Method (GOM) with a dissolved oxygen probe. The initial experiments were performed at five different positions, which are depicted in Figure 3.10(a). A difference of less than 2% was observed for k_La values at the different positions, which showed that mass transfer measurements were independent of location in the vessel when using the GOM with a DO probe. Furthermore, this showed that the well mixed assumption is reasonable. The values are summarised in Table C.1. Based on these, measurements were made at Position 2 only.

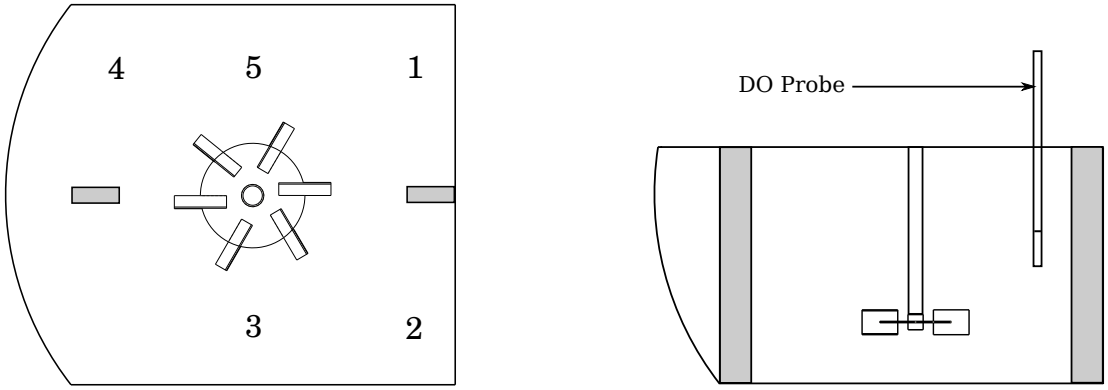

(a) (b)

Figure 3.10: (a) Mass transfer measurement points, (b) Position of DO Probe

3.3.5.1 Experimental equipment

The InPro6800 O_2 sensor (Mettler Toledo), DO probe, was used for the determination of k_La values. With the DO probe the measurement of the concentration of oxygen is based on a polarographic technique. The oxygen present close to the membrane, found at the tip of the probe, reacts with the membrane to produce a current which is proportional to the amount of oxygen. The current is then measured by a transmitter (Transmitter M300). The output voltage from the transmitter was captured using the commercial package LabVIEW 9.0.1 (National Instruments, 2009 SP1) and then post-processed using MATLAB (The Mathworks, R2010a).

3.3.5.2 Experimental procedure

Firstly, the oxygen concentration was lowered by gassing out the liquid with nitrogen gas. Then, the liquid was aerated with oxygen gas at a constant flow-rate and the increase in oxygen concentration was measured using the Dissolved Oxygen electrode. k_La is determined from the data of concentration of dissolved oxygen against time. The probe was placed at Position 2 with the tip located at half the tank height as shown in Figure 3.10(b). Position 2 was chosen so that the signal captured by the electrode was least affected by the noise produced, if any, by the jet leaving the impeller.

3.3.5.3 Data analysis

The rate of oxygen transfer from the oxygen bubble to the liquid phase is given by:

$$\frac{dC(t)}{dt} = k_La\,(C^* - C(t)) \tag{3.1}$$

where $C(t)$ is the concentration of dissolved O_2, (mmoles dm^{-3})
C^* is the saturated dissolved O_2 concentration, (mmoles dm^{-3})

k_La is the volumetric transfer coefficient, (s^{-1})

k_L is the mass transfer coefficient, (ms^{-1})

a is the gas/liquid interface area per liquid volume, (m^{-1})

Thus,

$$\ln\left(\frac{C^* - C(t)}{C^* - C_0}\right) = -\langle k_L a\rangle t \tag{3.2}$$

The values of $\ln(C^* - C(t))$ vs t were plotted. The gradient of the straight line obtained is equal to k_La. The saturated concentration of pure oxygen in water and synthetic leach liquor (SLL) were determined from the OLI StreamAnalyzer 3.0 software. The saturation curve for the two systems are shown in Figure 3.11 and 3.12 respectively.

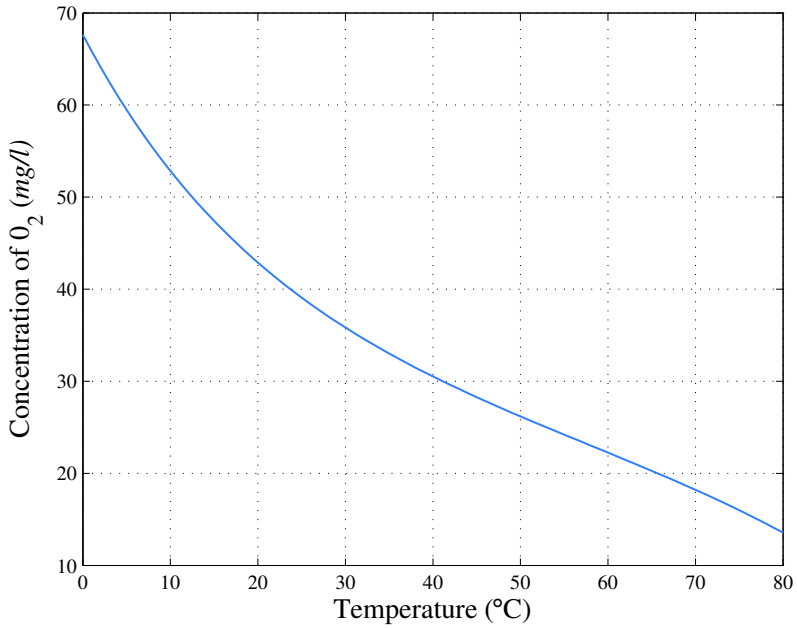

Figure 3.11: Saturation concentration curve of 0_2 in water

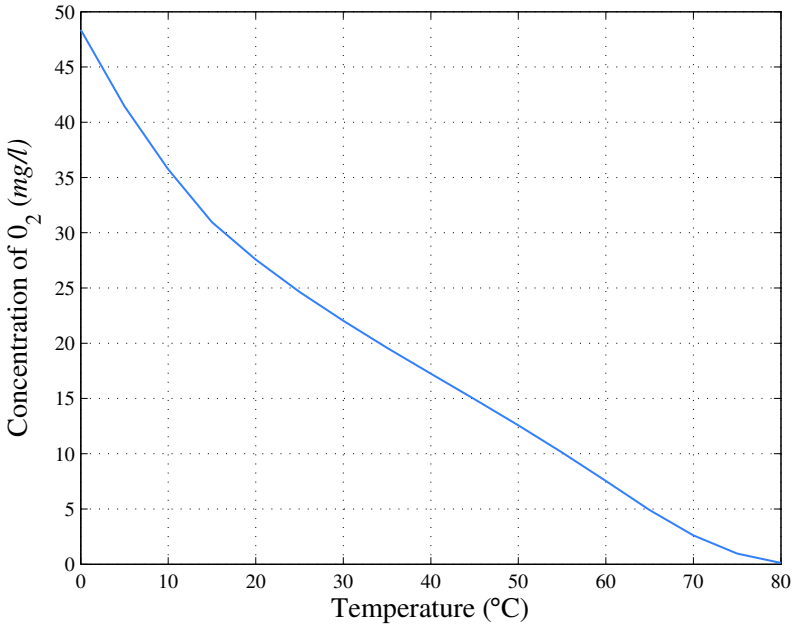

Figure 3.12: Saturation concentration curve of 0_2 in SLL

3.4 Repeatability and Errors

The experimental errors for the power draw, bubble size and mass transfer measurements are presented in this section. Bubble size and mass transfer measurement were found to be affected by the operating conditions, particularly at high temperatures and with the synthetic leach liquor. The apparatus used were found to be less accurate at certain operating conditions and to minimise errors as well as uncertainties the experiments were repeated. The errors were determined in terms of the standard error of the mean, σ_{m}, which gives an indication of how well the mean represents a population, and is given by :

$$\sigma_{\mathrm{m}} = \frac{\mathrm{s}}{\sqrt{\mathrm{n}}} \tag{3.3}$$

where s is the standard deviation
n is the number of observations

Such that $\overline{x} \pm \sigma_{\mathrm{m}}$, $\overline{x}$ is the mean.

3.4.1 Hydrodynamics

The experimental errors for the power draw is shown in Figure 3.13. It can be seen that after 3 repeats the errors for the power draw varied between 1.9% and 4.5%. The larger errors at the higher impeller speeds are mainly due to the small vibrations experienced by the rig at these speeds.

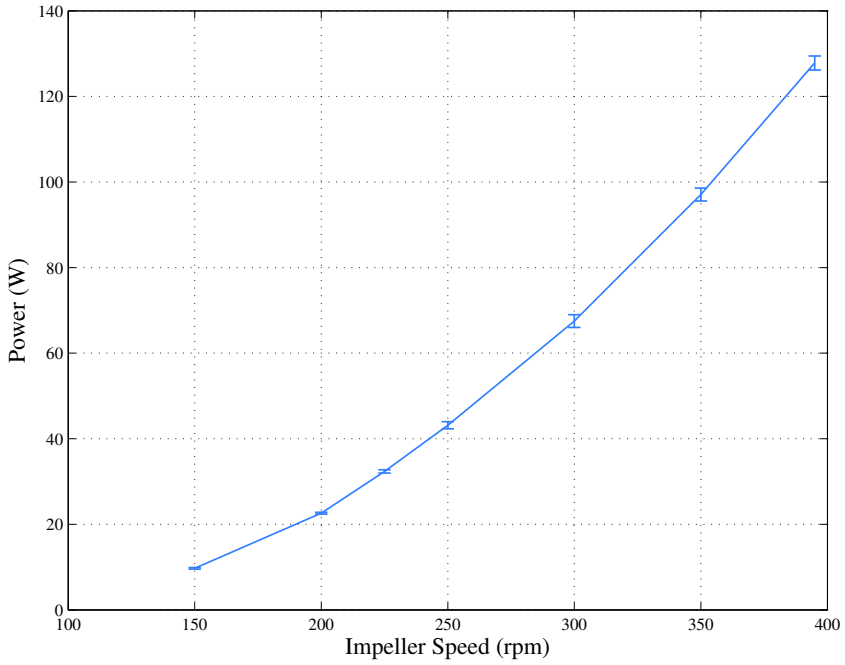

Figure 3.13: Errors for power draw measurement

3.4.2 Gas Dipersion

The result for the standard error of the mean for the bubble size measurements in the bulk region at a flow rate of 4.37 lmin^{-1} is shown in Figure 3.14. The errors were determined after 2 repeats, each with total of 100 photos.

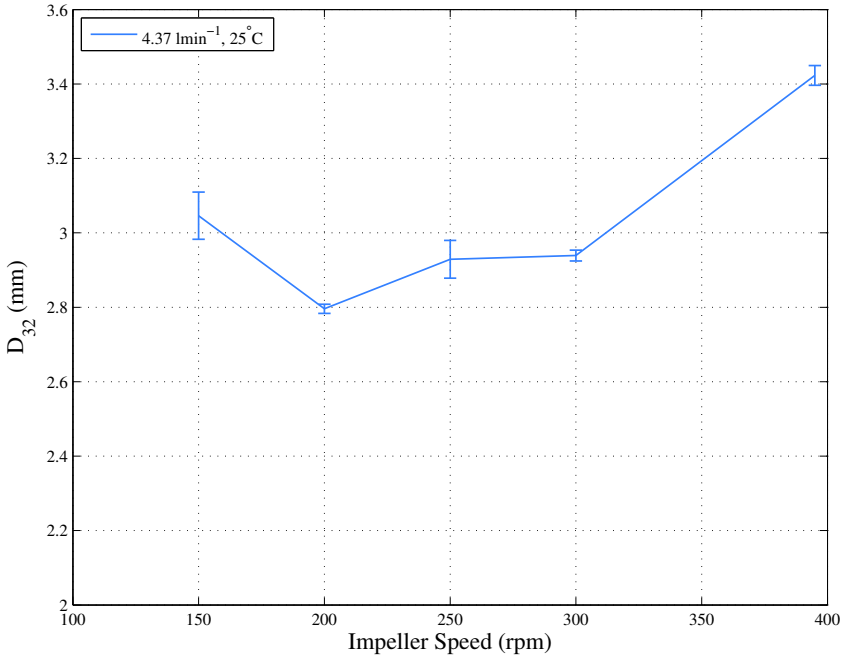

Figure 3.14: Errors for bubble size measurement

The errors for this case were found to vary between 1% and 4.5%. The errors are expected be in the same range for all the other cases.

3.4.3 Mass Transfer

Figure 3.15 shows the error for the gas liquid mass transfer coefficients, k_La, measurements for the water and oxygen system.

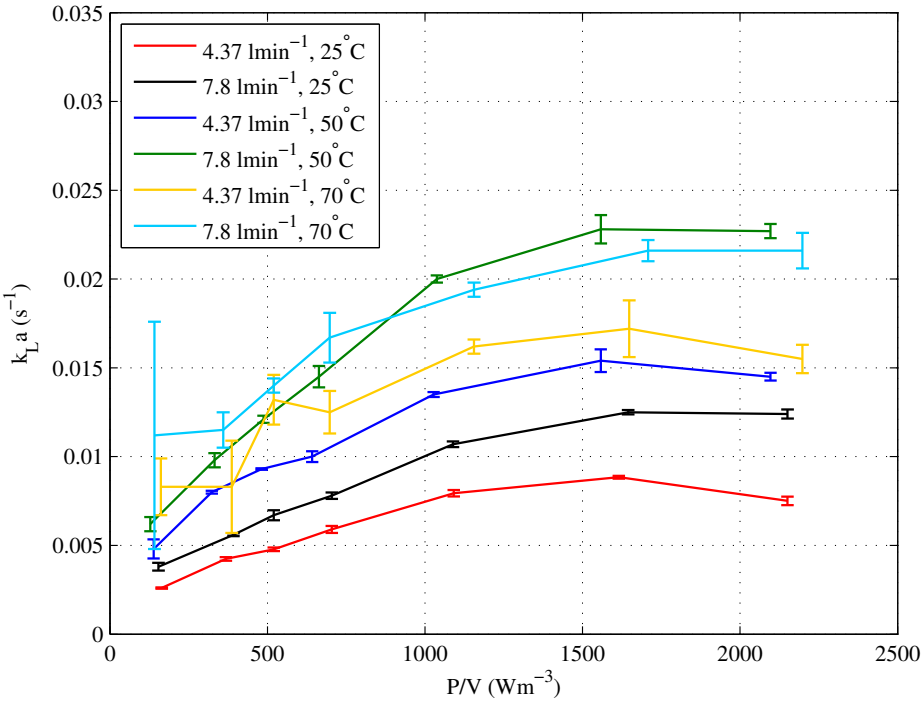

Figure 3.15: Errors for mass transfer measurement

The errors were based on data obtained after 3 repeats. The errors were negligible at ambient temperature, varying between 1 and 3%. However, they increased with temperature, reaching a maximum of 6% at 50°C and 30% at 70°C. Similar observations were made for the synthetic leach liquor, with a maximum error of 35%. The errors were due to the low saturation concentration of oxygen at high temperatures and in the synthetic leach liquor. This led to less accurate data as the measurement time was too short. For the synthetic leach liquor, because of the relatively high errors at low impeller speeds and high temperatures, only the results at 25°C are presented,

4 Numerical

The numerical techniques used to model the first compartment of the autoclave are presented in this chapter. The latter starts with a description of the geometry, computational grid as well as the impeller rotation model used to simulate the autoclave, as presented in Section 4.1 - 4.3. The computational model used to simulate the single phase and multiphase systems are presented in Sections 4.4 and 4.5. Each section covers the turbulence model, discretisation schemes and boundary conditions used to simulate both systems. The computing requirements and time are described in Section 4.6. This is followed by an overview of post-processing methods employed to determine the velocity, power draw, gas hold-up, bubble size and gas-liquid mass transfer coefficient.

4.1 Geometry

Before simulating any numerical model the domain or geometry has to be defined. Figure 4.1 shows the 3-D geometry used for the CFD simulations.

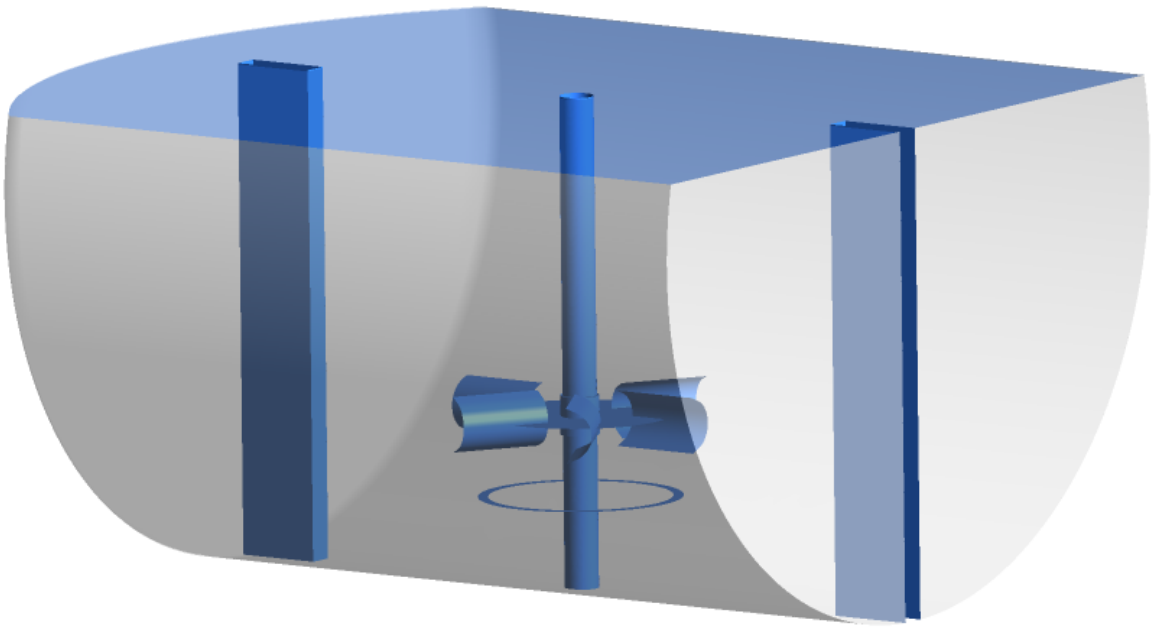

Figure 4.1: Computational model

The geometry was based on the experimental vessel and the dimensions are as described in Section 3.1. For the finite volume method the geometry is used to create the mesh or

grids as described in Section 4.2. The accuracy of the solution depends on the quality of the mesh used which is determined from the skewness of the cells. In order to avoid skew hexahedral cells in certain regions, minor changes were made to the geometry but not to the detriment of the overall solution. The impeller shaft was extended to the bottom of the vessel so that the mesh containing the impeller region could be swept or projected down to the bottom of the vessel. The impeller blades and disc have a thickness of about 2 mm but were modelled as infinitely walls. In addition the sparger, which is a tube curved in the shape of a diamond with 2 mm holes, was modelled as a thin disc. These changes were also made to facilitate meshing of the geometry with hexahedral cells. Moreover, meshing walls with small thickness would have required a very fine mesh and would have increased computational expense with a small improvement in accuracy.

4.2 Computational Grid

The first step to numerically model a system is to divide the domain into discrete finite volumes or grids. The commercial preprocessor Gambit 2.4 was used to create the geometry and the grids.

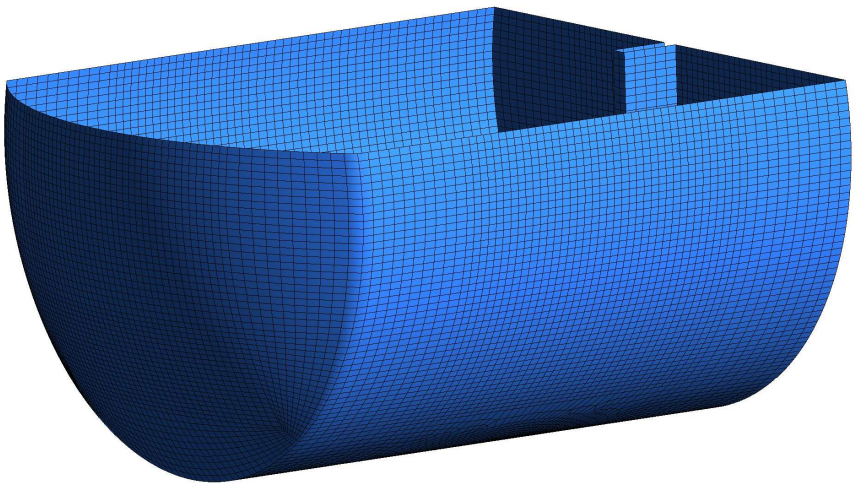

Figure 4.2: Autoclave divided into discrete volumes

Figure 4.2 and Figure 4.3 show the grid for the autoclave model and for the impeller respectively. A full 3-D model was created due to the asymmetry of the system. The accuracy of the solution and computation time depends on the mesh quality. The type of mesh used is problem dependent. However, hexahedral meshes give more accurate solutions than other types of mesh for the same number of cells used. To this end unstructured hexahedral cells were used and also because of the geometry of the vessel and of the impeller. The skewness of the cells were kept below 0.85 which is acceptable to avoid inaccurate solutions. The

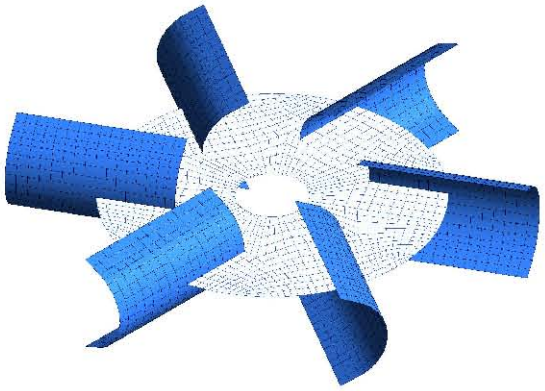

Figure 4.3: Impeller grid

mesh containing the impeller consisted of a cylindrical region. The latter is created to implement the impeller rotation model and is further described in Section 4.3 with the relevant dimensions. The mesh surrounding the impeller and in the impeller discharge region was finer due to the high velocity gradients that occur in these regions.

A grid refinement study was made using Grid 1 and Grid 2. The number of cells used are tabulated in Table 4.1.

Table 4.1: Computational grid

Impeller Grid	**Number of Cells**		
	Bulk	**Impeller**	**Total**
1	232 695	90 054	**322 749**
2	946 608	114 752	**1 061 360**

4.3 Impeller Rotation Model

The system was modelled using two impeller rotation models, namely the Multiple Reference Frames (MRF) and the Sliding Mesh (SM) models. The MRF model in an unsteady system was used to start up the simulation and then the SM model was used to solve the flow completely. This approach was adopted to reduce computational time. The sliding mesh model was used to completely solve the flow field and also to account for any time dependent flow interaction that could exist between the impeller and curved sides. To use either the MRF or the SM model, two zones must be defined, these were named the bulk zone and the impeller zone.

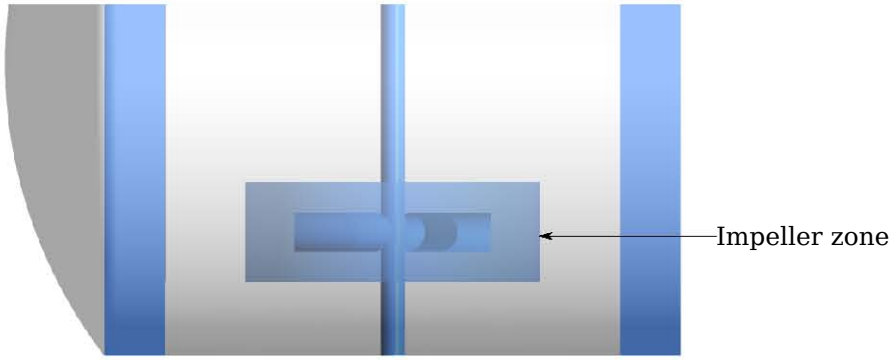

Figure 4.4: Autoclave computational model

Figure 4.4 shows the region representing the impeller zone and the rest of the vessel being the bulk zone. Lee and Yianneskis (1994) reported that in a stirred system with a Rushton turbine the flow within the region surrounding the impeller is strongly periodic and is approximately cylindrical in shape. The cylinder, or the impeller zone as named for this study, had a height three times the blade height and a diameter equal to twice the diameter of the impeller. However, due to the geometry of the autoclave, with curved sides and bottom as well as the position of the sparger, the dimensions above were altered. The impeller region was only 0.75 blade height above and below the blade and 0.25 the impeller diameter away from the impeller. A similar approach was successfully used by Bakker (2009) for similar reasons.

4.4 Computational Model: Single Phase System

The single phase system was modelled with water as fluid. The two grids as described in Section 4.2 were used for comparative purposes. The power draw and velocity for the two grids were compared to experimental data. The results are presented in Section 5.1. The standard k-ε turbulence model of Launder and Spalding (1974) was used to account for the turbulent flow regime.

4.4.1 Discretisation Scheme and Pressure-Velocity Coupling

The first order upwind differencing scheme was used for the start of the simulations to discretise the momentum and turbulence equations. Then higher order QUICK scheme was used for the discretisation of the equations. The SIMPLE algorithm was used for pressure-velocity coupling.

4.4.2 Boundary Conditions

Standard wall functions as proposed by Launder and Spalding (1974) were used to model the viscous flow regime near solid surfaces. These include the baffles, inner surface of the tank, sparger and impeller which are depicted in Figure 4.5. The y^+ value varied between 40 and 280, which is an acceptable range for the Standard wall treatment.

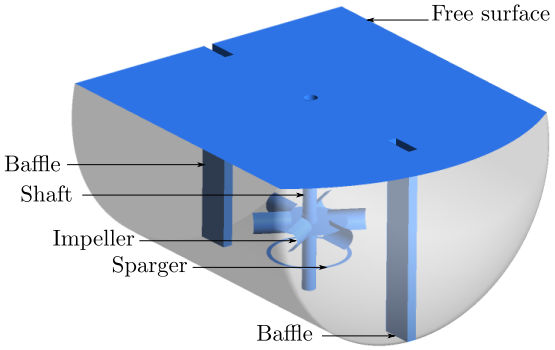

Figure 4.5: Surfaces for computational model

The free surface with the current system was found to be non-stationary and with a vortex formation at certain impeller speeds. The free vortex was found to occur for speeds above 225 rpm. Figure 4.6(a) shows a front view of the tank at 200 rpm, with a relatively flat free surface. Figure 4.6(b) shows the occurrence of a vortex at 395 rpm and an uneven free surface. These are expected to occur because of the geometry of the vessel, the position of the baffles and impeller. Even though entrainment occurred at the higher impeller speeds, it was not substantial. To investigate this phenomenon the free surface is usually modelled with a Volume of Fluid (VOF) approach. The latter, although models the free surface reasonably well, is too computationally expensive. Therefore, the free surface as shown in Figure 4.5 was modelled with a symmetry boundary condition, which assumes that a free surface is stationary.

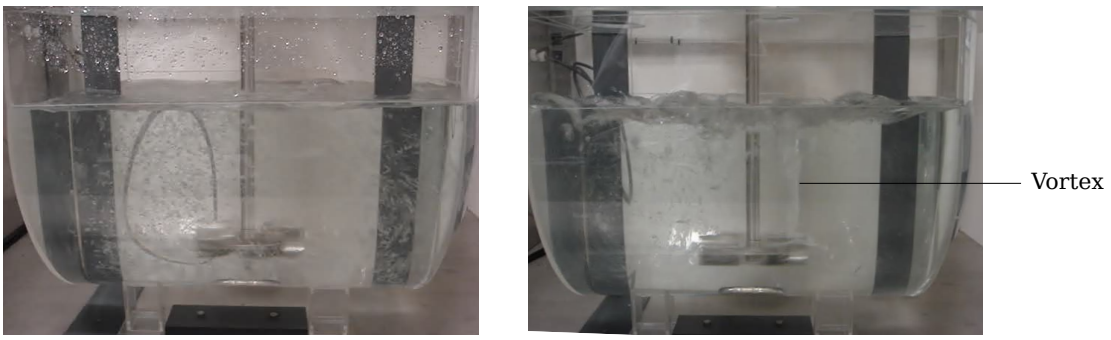

(a) (b)

Figure 4.6: (a) Fluid flow at 200 rpm, (b) Fluid flow at 395 rpm

4.5 Computational Model: Gas-liquid System

The commonly used Euler-Euler model (Gimbun et al., 2009; Kerdouss et al., 2008; Scargiali et al., 2007; Khopkar et al., 2005; Aubin et al., 2004a; Morud and Hjertager, 1996; Ranade and Van Den Akker, 1994) was employed to simulate gas-liquid flows in mixing vessels. The choice of the turbulence model was based on the influence of the secondary phase (gas) on the primary phase (water). Riet and Smith (1973) reported that if bubble sizes are small and superficial gas velocity is low it can be assumed that the influence of gas phase on the primary phase is low. Moreover, Khopkar et al. (2003) showed that in the impeller stream where turbulent dissipation terms were not significant, the influence of the dispersion terms were not quantitatively significant. Since the influence of the gas phase was marginal, the dispersed k-ε turbulence model was used to simulate the inherent turbulent flow.

Besides the effect of turbulent dispersion, the gas-liquid system is also affected by virtual mass and lift. The gain in accuracy that will be obtained by accounting for the virtual mass and lift will be very small compared to the increase in computational demand that would be required (Scargiali et al., 2007). Nevertheless, the effect of drag force is significant in stirred tanks. As mentioned in Section 2.2.2 different approaches to the drag model have been used in previous studies. The Schiller-Naumann model was used to account for the effect of drag. This model was recently used by Gimbun et al. (2009) and reasonable gas-liquid predictions were obtained. The model was considered acceptable, as the bubbles were smaller than 5 mm in diameter and spherical in shape. Therefore, other models were not investigated even though it is acknowledged that other models could be considered to improve the CFD predictions.

The gas phase was modelled by using either a constant bubble size or a size distribution. The bubbles are treated as a dispersed phase in each cell, such that a bubble and a fluid encapsulating the bubble form a continuum. When using the dispersed k-ε model, the primary phase controls the motion of the secondary phase, such that the influence of the bubbles on the flow field is negligible. Therefore, to ensure that the effect of the secondary phase is kept to a minimum and to avoid numerical instability the bubble size should be smaller than the cell size.

4.5.1 Population Balance Model

Bubble size distribution was modelled using the discrete method. It is based on representing the bubble size distribution in terms of classes or bins (ANSYS, 2010). This robust method gives the bubble size distribution directly. However, the bins must be defined

at the start of the simulation and may require a large number of classes. On the one hand, Laakkonen et al. (2007) reported that more than 80 classes are required to minimize discretisation errors. On the other hand, Kerdouss et al. (2008) showed that satisfactory results were obtained with 13 classes. From the experimental data it was found that bubble size distribution did not vary substantially around the mean. It was found that 11 classes gave satisfactory results. The results are presented in Section 5.2.1.

The classes were divided according to bubble size distribution which varied according to the experimental conditions used, as tabulated in Section B.1. The bubble size distribution, which was used as input for the model, was divided into the classes according to the following equation:

$$\frac{v_{i+1}}{v_i} = 2^q \tag{4.1}$$

where v is the volume of a bubble and q is a ratio factor that can be obtained using a geometric progression approach and the known minimum as well as maximum bubble volumes.

The Luo and Svendson bubble break-up model was used. This model as outlined by Laakkonen et al. (2007) has some deficiencies. It has a dependence on the size discretization and that some parameters should be fitted by comparing measured and predicted bubble size. However, from preliminary simulations it was found that the Luo breakage and coalescence model gave satisfactory results.

4.5.2 Discretisation Scheme and Pressure-Velocity Coupling

The momentum equations and the volume fraction were discretised with the QUICK scheme. First order schemes were used for the discretisation of the turbulent kinetic energy and dissipation rate. Higher order schemes were not used to avoid an increase in the computational time of the multiphase system which was already intensive. The phase-coupled SIMPLE algorithm was used for the pressure velocity coupling.

4.5.3 Boundary Conditions

The boundary conditions used for the multiphase system are similar to the ones used for the single phase system. However, to account for the gas phase, the sparger and the outlet were modelled as described below.

4.5.3.1 Outlet

There are various ways to model the outlet of the vessel, by using mass sinks, velocity outlets, pressure outlets or an outflow boundary. A method that is commonly used is to include a volume of gas on top of the vessel, as shown in Figure 4.7, with either a pressure

boundary or an outflow boundary. In the research work conducted by Engelbrecht (2006) the outlet was modelled using an outflow boundary. The outflow boundary extrapolates the flow variables from within the domain. A pressure outlet can also be used with the degassing volume method (Appa, 2007).

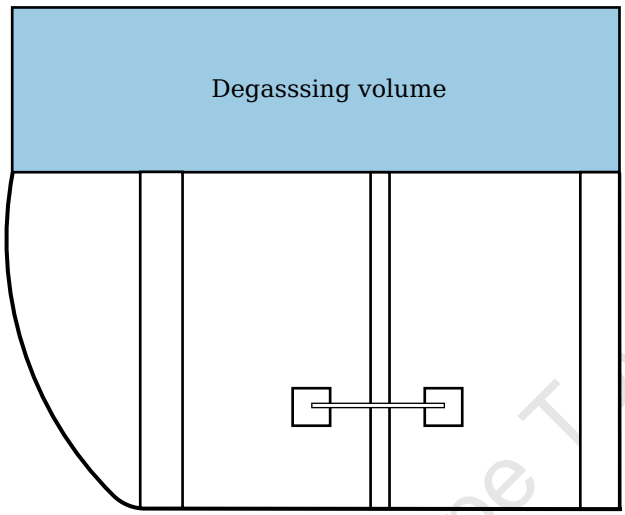

Figure 4.7: Tank with degassing volume

Authors such as Lane et al. (2002), Khopkar et al. (2005) and Spicka et al. (2001) used the mass sinks approach, where mass sinks were specified on the top-most cells. Gentric et al. (2005) used a similar technique, where the outlet was modelled as a degassing boundary, with an outlet for the gas phase and a no-slip wall for the liquid phase. Morud and Hjertager (1996) modelled the outlet using a velocity boundary and the velocity was determined on a mass balance based on the specified inlet conditions. The advantage of using those methods is that the additional volume, normally used to allow the gas to leave the system in a more stable manner, is not required. However, this approach does not allow for any changes in the free surface.

Preliminary work was done using the degassing volume method. Figure 4.8 shows the contour plot of the volume fraction of oxygen at 395 rpm using the degassing volume method to simulate the gas-liquid system. Even though, it is stable the Euler-Euler model is not suitable to model free surfaces. It was found that with the moving free surface, the latter collapsed and led to a large amount of gas being entrained from the degassing volume into the vessel.

Moreover, the additional volume increased the computational expense and was considerable when using the population balance model. Therefore, the free surface was modelled as a degassing boundary, where a velocity boundary is used. The velocity and volume

fraction of the gas at the boundary is set to the value at one cell below the boundary. A no-slip wall for the liquid phase was used, where the water was only allowed to move along the boundary, with the normal component of velocity set to zero.

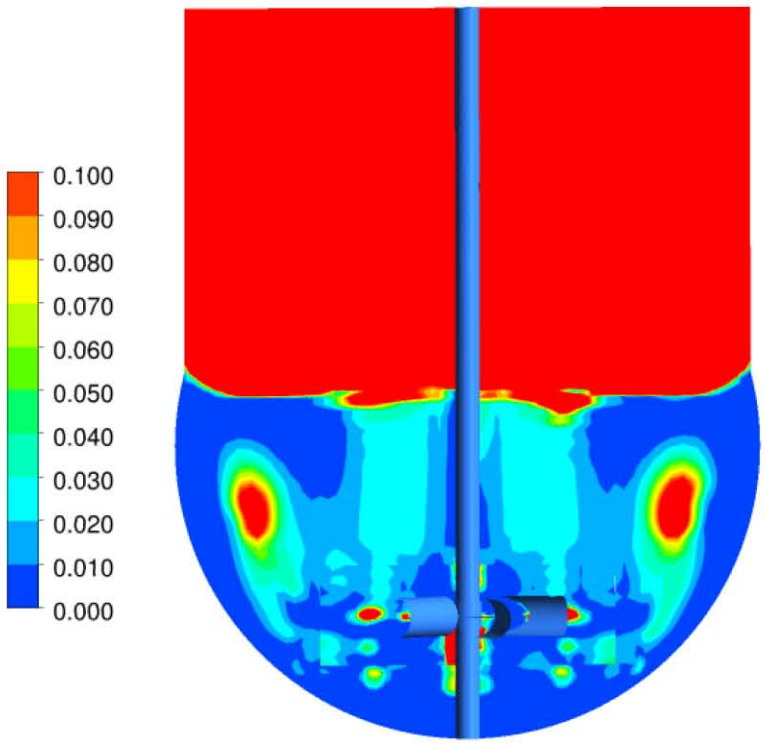

Figure 4.8: Contour plot of volume fraction of oxygen at 395 rpm

4.5.3.2 Spargers

In the research work presented by Ranade and Deshpande (1999) the spargers were modelled as mass sources. This technique allowed the gas to be modelled in the form of bubbles entering the system. This is achieved by setting the sparger inlet equal to the estimated bubble rise velocity with the volume fraction determined from the gas volume flow rate.A similar approah was used by Gentric et al. (2005). The sparger has also been modelled using velocity boundary for the inlets (Morud and Hjertager, 1996; Kerdouss et al., 2006; Engelbrecht, 2006).

The sparger was modelled as a velocity inlet for this research work. The velocity was based on the volume flow rate of oxygen and superficial area of the sparger model. The volume fraction of gas was assumed to be one, simulating pure gas entering rather than bubbles.

4.6 Computers, Computing Time and Convergence

Single phase and multiphase simulations were done using an AMD Quad Core 2.15GHz CPU with 8GB of RAM and an AMD dual Quad Core 2.2GHz CPU with 16GB of RAM respectively. For both single phase and multiphase systems all cores were used, that is 4 and 8 respectively. The average running time for the multiphase simulations were about three weeks. A convergence criteria of 1×10^{-3} for the scaled residuals was used to obtain satisfactory solutions.

4.7 Analysis

Post-processing techniques to analyse and validate the CFD models are discussed in the following sections. These include data for hydrodynamics, gas dispersion and mass transfer. Factors such as power, velocity flow field, bubble size and mass transfer were validated against experimental data. The results for the different systems investigated are presented in Chapter 5.

4.7.1 Hydrodynamics

4.7.1.1 Power draw

It was determined from the torque experienced by the impeller and the known impeller rotational speed. The torque was determined by calculating the sum of the moments on both sides of the impeller blades. The moment is calculated from the sum of the cross product of the pressure and viscous forces with the moment vector, which is from the moment center to the force origin ANSYS (2010).

$$\underbrace{\vec{M}_A}_{\text{total moment}} = \underbrace{\vec{r}_{AB} \times \vec{F}_p}_{\text{pressure moment}} + \underbrace{\vec{r}_{AB} \times \vec{F}_v}_{\text{viscous moment}} \tag{4.2}$$

where A is the specified moment center
B is the force origin
$\vec{r}_{AB}$ is the moment vector
F_p is the pressure force vector
F_v is the viscous force vector

4.7.1.2 Velocity

The validation of the CFD velocity data against the PIV measurements was performed by comparing velocity profiles on three different planes and at different positions on the

planes as outlined in Section 3.3.2.2. The velocity components in two directions were determined by using a time averaging technique.

4.7.2 Gas Dispersion

4.7.2.1 Gas hold-up

The gas hold-up (ϕ), which is the dimensionless volume fraction of the gas phase, was determined from the average volume fraction of oxygen in the vessel.

4.7.2.2 Bubble size distribution

The data for the bubble size distribution was obtained from the post processing population balance model module available in FLUENT. Data such as the bin fraction, number density, moment and the Sauter mean diameter were obtained.

4.7.3 Mass Transfer

The volumetric mass transfer coefficient was calculated as a product of liquid mass transfer coefficient, k_L, and inter-facial area per unit volume, a.

k_L was determined by using two methods; the slip penetration model and the eddy cell model as given by equation 4.3 and 4.4, respectively.

$$k_L = \frac{2}{\sqrt{\pi}}\sqrt{\frac{D_L u_{slip}}{d_b}} \tag{4.3}$$

$$k_L = F\sqrt{D_L}\left\{\frac{\epsilon_L \rho_L}{\mu_L}\right\}^{0.25} \tag{4.4}$$

Different values of F have been used, for example 0.4 (Lamont and Scott., 1970; Gimbun et al., 2009), 0.3 (Moilanen et al., 2008) and 1.13 (Dhanasekharan et al., 2005; Kerdouss et al., 2008). These values mainly have been used as a correction factor for the poor prediction of turbulent parameters as often seen in mixing vessels. A value of 0.7 was found adequate to correctly predict mass transfer for both flow-rates used for this study

A similar approach used by Kerdouss et al. (2006) was employed to determine the inter-facial area. The latter is based on the local volume fraction and the local Sauter mean diameter as given by:

$$a = \frac{6\alpha_G}{d_{32}} \tag{4.5}$$

The local and average $k_L a$ were determined from the product of k_L and a based on equations 4.3, 4.4 and 4.5. A volume average approach was used to determine the average $k_L a$.

The diffusivity of oxygen at the elevated temperatures and in the leach liquor was determined from the Wilke and Chang (1955) equation:

$$D_{AB} = \frac{7.4 \times 10^{-8} (\chi_B M_B)^{\frac{1}{2}} T}{\mu_B V_A^{0.6}} \tag{4.6}$$

5 Results and Discussion

The results and discussion for this research work are presented in this chapter. The latter is divided into three main sections; hydrodynamics, gas dispersion and mass transfer, as presented in Sections 5.1, 5.2 and 5.3 respectively. Each section covers the validation of the CFD model against experimental data; with hydrodynamics validated in terms of power draw and velocity flow field, gas dispersion with bubble size and finally mass transfer validated in terms of the gas-liquid mass transfer coefficient, k_La. Besides being used for validation and comparative purposes, the CFD predictions, complemented with experimental data, are used to describe trends in hydrodynamics, gas dispersion and mass transfer. These are presented as the effects that the geometry of the vessel and operating conditions have on the three flow phenomena. The implication of these effects on mass transfer in the pilot scale autoclave is also covered. Finally, a power law correlation for the autoclave is presented and discussed in Section 5.3.6.

5.1 Hydrodynamics

Mixing processes in turbulent agitated tanks are spatially non-homogeneous (Tatterson, 1991). The processes are commonly characterised in terms of power, velocity and turbulence parameters. These quantify mixing processes on both a local and a global level, hence providing a fundamental understanding of an entire system. To this end, the different flow phenomena were investigated and results as well as discussion are presented. Firstly, results showing the validation of the CFD models against experimentally measured data are presented in Section 5.1.1. This is followed by Sections 5.1.2 - 5.1.3 which cover the effect, of geometry of the autoclave, impeller speed and gas dispersion, on the various phenomena mentioned above. Finally, the implications of the various hydrodynamic parameters to mass transfer in the autoclave are discussed in Section 5.1.5.

5.1.1 CFD Model Validation

The validation of the numerical model used to predict hydrodynamics in the first compartment of the pilot-scale autoclave is presented in this section. The CFD model was validated globally with power draw and locally with velocity flow field. These were compared to experimental data. The findings with the discussion are presented in Sections 5.1.1.2 - 5.1.1.3 for the power and velocity flow field respectively.

5.1.1.1 Numerical

The accuracy of single phase flow predictions in mixing vessels is mainly affected by the order of discretisation schemes, turbulence model and grid resolution. The order of the discretisation scheme normally has very little or no effect on the prediction of local velocities provided a sufficiently fine mesh is used (Aubin et al., 2004a; Deglon and Meyer, 2006; Bakker, 2009). Similarly, the turbulence model has a negligible effect on the prediction of local velocities as reported by Jaworski and Zakrzewska (2002) when comparing the standard k-ε model to five of its variants. The main issue is normally with the prediction of the turbulent kinetic energy, which is under-predicted or over-predicted (Deglon and Meyer, 2006). However, these as well can be reduced by using higher order discretization schemes and/or finer grids (Deglon and Meyer, 2006; Wechsler et al., 1999). To this end the QUICK scheme and the standard k-ε turbulence model was used. The results, for which two different grids were used, are shown in the following sections. In general, good agreement between experimental and numerical results were obtained, using the above-mentioned numerical approach, for two grids. The model predicted the power draw reasonably well and similarly for the local velocities. In addition, the model was able to reproduce flow phenomena atypical for stirred tanks with radial impellers. These are further discussed in the following sections.

5.1.1.2 Power draw

Power draw is the amount of energy per unit time which is transferred from the impeller to the fluid. The power draw is affected by impeller speed and torque experienced by the impeller blades to overcome drag forces. It is expected to increase with an increase in impeller speed and torque.

Figure 5.1 illustrates the results for the power draw over a range of impeller speeds. The experimental results are compared to values predicted using the numerical model. Furthermore, the effect of the cell size was investigated by using two different grid sizes. These are labeled as Grid 1 and Grid 2 where the latter is the finest. The results show good agreement between the experimental and numerical numerical data, with an increase in power draw with increasing impeller speed. A small over-prediction was observed at the higher impeller speeds, 350 and 395 rpm. At these speeds, the occurrence of the free vortex from the surface, causing a marginal amount air to be drawn in by the impeller, was more likely. There was also a higher degree of recirculation at the surface of the vessel. The over-prediction can be a result of the effect of the free surface, which was excluded in the numerical model, and/or the effect of modelling the impeller blades as infinitely thin walls. Furthermore, when comparing the numerically determined power draw it can be

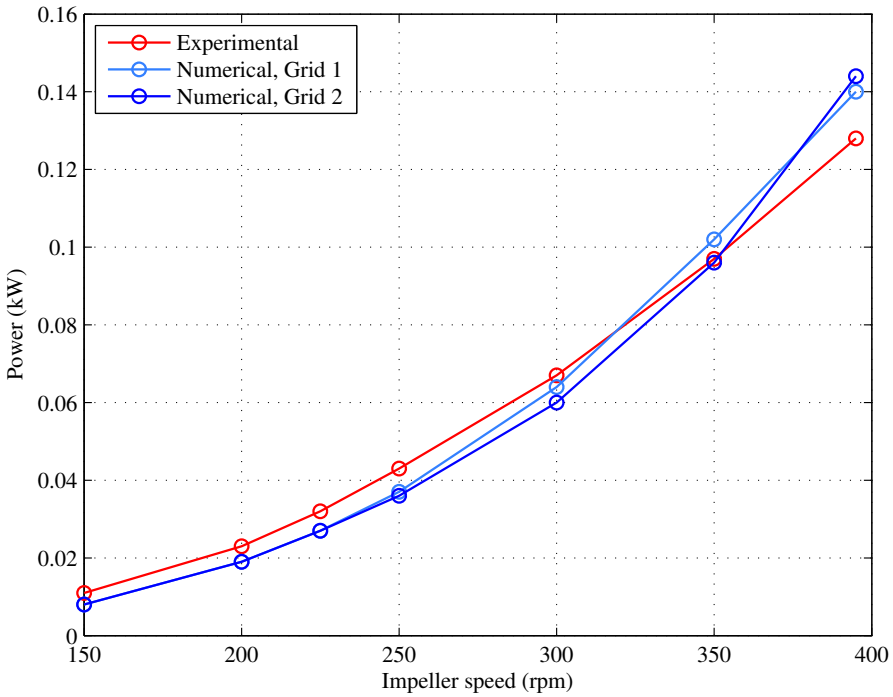

Figure 5.1: Power draw - CFD and Experimental

seen that the difference between the values for the two grids are negligible. This suggests that the cell resolution of Grid 1 is fine enough to predict power draw.

5.1.1.3 Velocity flow field

The key objective of mixing in a stirred vessel is to provide a homogeneous mixture and is usually characterised in terms of the flow patterns. Besides giving an overall view of the flow field it also provides an insight to other phenomena; such as gas dispersion and distribution of mass transfer in the vessel. The flow patterns are a function of the geometry of the vessel, the impeller type and the operating conditions. The typically observed flow pattern in a baffled stirred tank agitated by a radial impeller is the commonly known double-loop structure. There are two recirculation loops, one above and the other below the impeller, that are produced when the strong radial flow hits the wall of the vessel. Due to the importance of the flow pattern, this section is firstly based on a qualitative validation of the velocity flow field and is followed by a quantitative validation, by comparing velocity profiles.

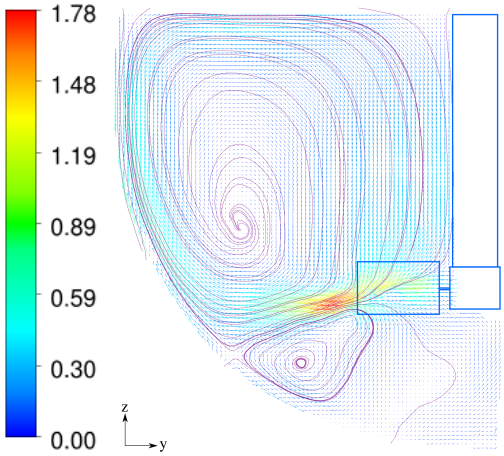

Figure 5.2: Velocity flow field at 150 rpm - PIV

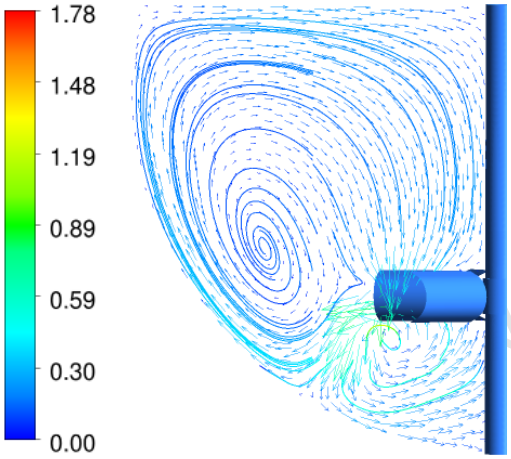

Figure 5.3: Velocity flow field at 150 rpm at Position 1 - CFD

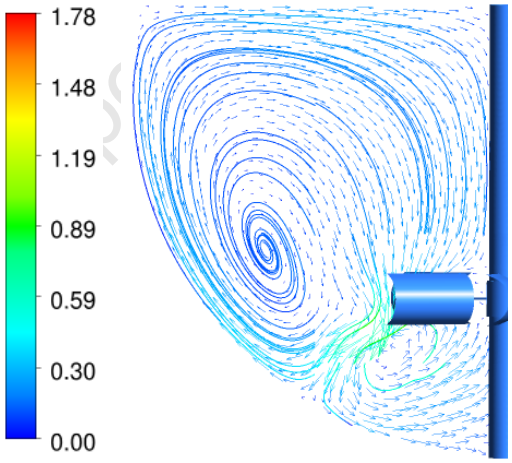

Figure 5.4: Velocity flow field at 150 rpm at Position 2 - CFD

Flow patterns on a vertical plane at the center of the tank at an impeller speed of 150 rpm are shown in Figures 5.2-5.4. The results from PIV measurements are compared to predicted flow fields. Figure 5.2 shows time-averaged velocity flow field on the yz-plane from the PIV measurements. Figures 5.3 and 5.4 show the instantaneous velocity flow field from CFD simulations with impeller blades at two positions, Position 1 and Position 2 respectively. At Position 1, the vertical plane is behind one of the impeller blades and at Position 2 the vertical plane is midway between two blades. From both PIV and CFD results it can be seen that the characteristic velocity flow field expected in a mixing vessel with a radial flow impeller is distinct. This is recognised by the two recirculation loops, one above and one below the impeller. Furthermore, it can be observed that the results from the CFD predictions and PIV measurements are qualitatively similar. Both CFD

and PIV results show the two recirculation loops, with the larger loop in the bulk region.

Furthermore, it can be observed that both CFD predictions and PIV measurements captured an atypical flow behaviour in the impeller region. Normally with a radial flow impeller the fluid leaves the impeller tip horizontally. However, this is not reproduced here with the Smith turbine. It can be seen from Figures 5.2-5.4 that both the CFD model and PIV experiments show that the fluid in the impeller stream is at an angle to the horizontal. The downward inflection can be due to the effect of the low pressure generated by the lower recirculation loops and/or an 'attraction' due to the 'Coanda' effect as a result of the bottom surface of the tank (Montante et al., 2001). This flow phenomena is normally observed in dished bottom vessel (Deen et al., 2002). From the CFD predictions it can be observed that the position of the impeller also influences the flow in the impeller stream. When comparing the radial flow at the two impeller positions, Position 1 and 2, it can be seen that there is a difference in the angle of inclination. It is believed the low pressure region created by the passage of the curved blades results in this difference.

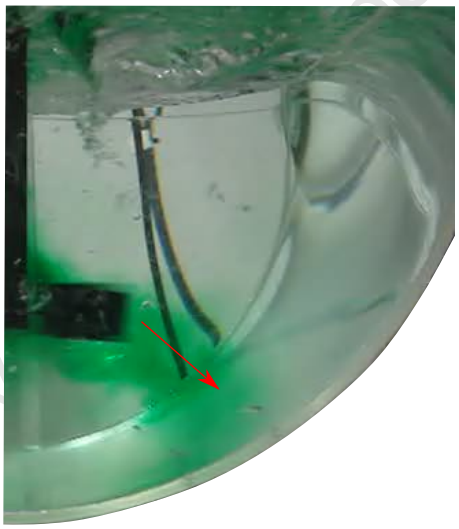

Figure 5.5: Flow field at 150 rpm - Flow visualisation

A flow visualisation study was used to visually confirm this unusual finding by using a dye to highlight the flow patterns. Figure 5.5 shows the flow pattern on a vertical plane in the center of the tank at 150 rpm, which clearly shows the inclined radial jet leaving the impeller.

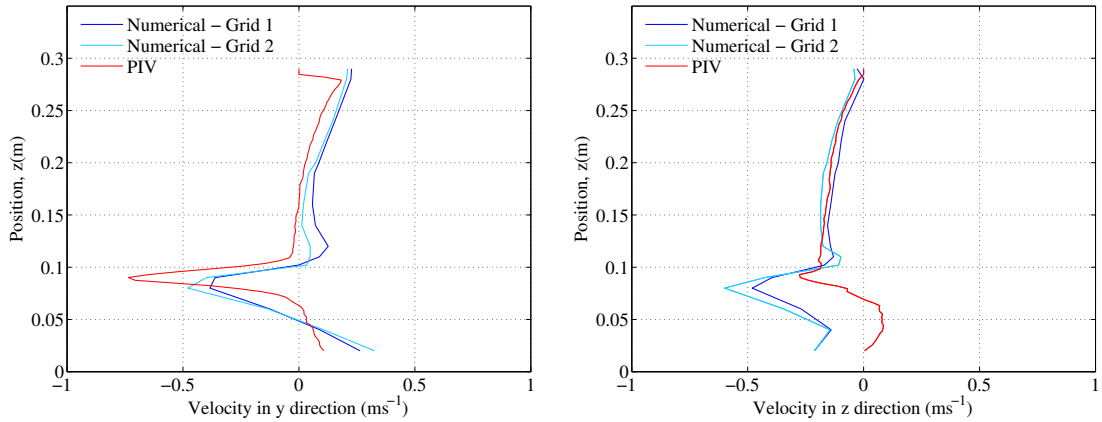

(a) (b)

Figure 5.6: Velocity profile at 150 rpm - CFD and PIV (a) v_y, (b) v_z

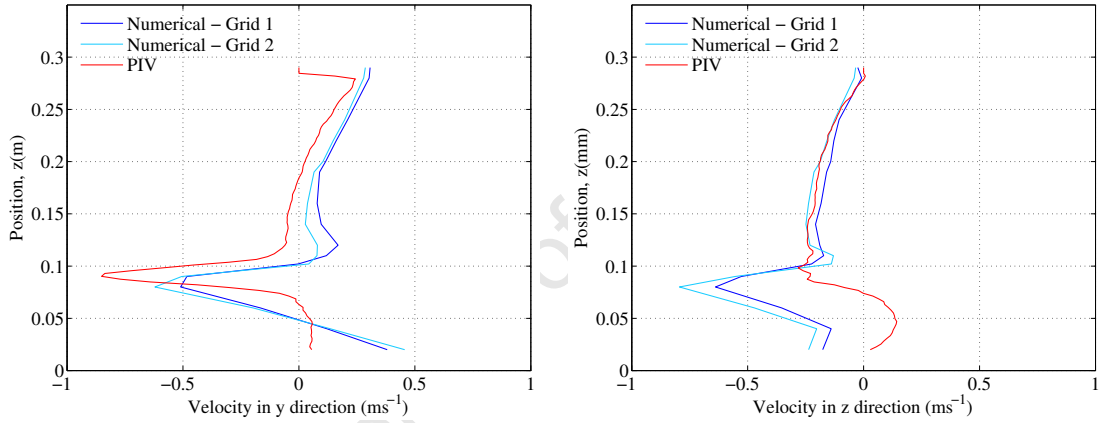

(a) (b)

Figure 5.7: Velocity profile at 200 rpm - CFD and PIV (a) v_y, (b) v_z

The predicted flow field was quantitatively validated by comparing velocity profiles in the y and z directions as defined in Figure 5.2. The validation presented are for three impeller speeds (150, 200 and 250 rpm) as shown in Figures 5.6-5.8. The velocity profiles were obtained at a distance of 10 mm away from the impeller tip (see Figure 3.6(a)). The expected velocity profile can be observed under all conditions, with high velocities in the impeller region. It can also be seen that the velocity displays a maximum value below the impeller tip, which is located 102 mm above the bottom surface of the vessel.

From Figure 5.6(a) it can be seen that the CFD model reasonably predicts the y-component of the velocity. In the bulk region the experimentally measured velocity showed good correlation to the predicted values for both Grid 1 and Grid 2. However, a discrepancy is observed for the prediction of the maximum velocity, with $0.3U_{tip}$, $0.38U_{tip}$, $0.58U_{tip}$ for

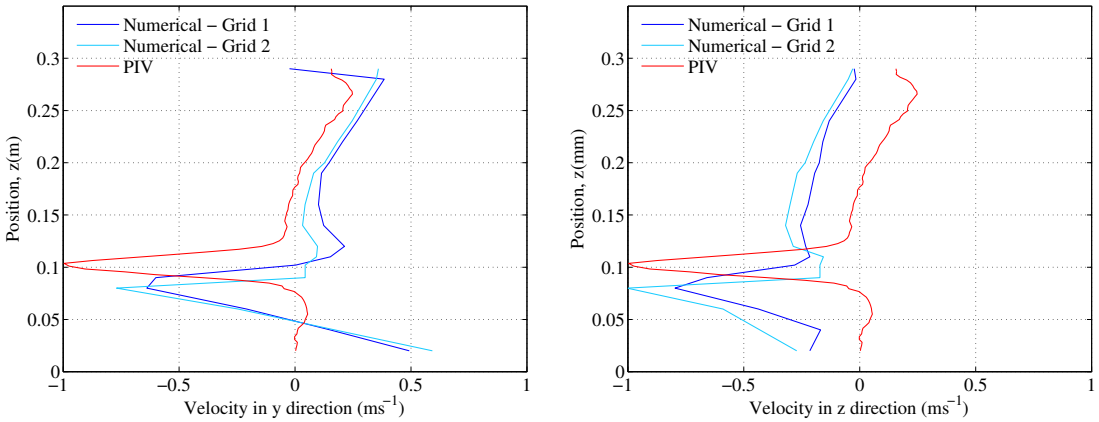

(a) (b)

Figure 5.8: Velocity profile at 250 rpm - CFD and PIV (a) v_y, (b) v_z

Grid 1, Grid 2 and PIV respectively. The disagreement can be due to both numerical and experimental errors. It can be observed that both Grid 1 and Grid 2, even though with an improvement with Grid 2, under-predicted the peak velocity. It is unclear whether it is due to the turbulence model as the latter should not affect the prediction of the local velocity (Jaworski and Zakrzewska, 2002). The difference in the maximum velocity can be attributed to an experimental error as reported by Montante et al. (2001). The authors observed an under-prediction of the fluctuating velocities, which also had an effect on the mean velocity, when using LDA for validation. The discrepancy was attributed to experimental errors as a result of the fast fluctuations of the flow patterns.

It can also be observed that there is a difference in the position of the peak velocity between the experimental and predicted values, which is exacerbated at 250 rpm. This was mainly due to the inability to exactly predict the inclination of the flow leaving the impeller tip as similarly observed by Montante et al. (2001). The discrepancy was attributed to the inability of the CFD model, the simulation strategy and turbulence model, to reproduce the single-loop flow structure.

From Figures 5.6(b), 5.7(b) and 5.8(b) it can be observed that the velocity in the z-direction was well-predicted in the region above the impeller. However, some disagreements are noticeable in the impeller region and below. Below the impeller the effect of the surface on the velocity flow field is larger and therefore the 'attraction' due to the 'Coanda' effects is expected to be larger, mainly on the axial component. Therefore, the discrepancies is believed to be due the turbulence model which cannot exactly predict the flow in the lower recirculation loop.

5.1.2 Effect of Geometry on Hydrodynamics

Hydrodynamics is known to be affected by the geometry of a vessel, position of the impeller and baffles. Similarly, the shape of the autoclave has an effect on the velocity flow field, power draw and turbulent parameters. This section illustrates the key hydrodynamic features observed in the autoclave.

5.1.2.1 Power draw

Power in mixing tanks is dependent on the amount of drag experienced by the impeller blades (Tatterson, 1991). The drag experienced by the blades is a sum of pressure or form drag and skin drag. These are highly dependent on the shape of the impeller blades and also the flow field around blades. In mixing tanks, due to the complex flow regime and its turbulent nature, the fluid mechanics around the impeller blades is believed to have an effect on the resulting drag. In the autoclave as observed in Section 5.1.1.3, the geometry of the vessel does have an influence on the flow field close the impeller blade and it is expected to have an impact on the power draw.

The power draw can be expressed in terms of the power number, N_p, (Equation 5.1) and can be used for comparison for systems using similar impeller blades. The power number is not a constant quantity for a specific impeller and Reynolds number (Tatterson, 1991). It depends on various factors, among which are the geometric configuration of the vessel and the associated flow pattern. Power draw can be used to give an indication of the power draw in a mixing vessel.

$$N_p = \frac{P}{\rho N^3 D^5} \tag{5.1}$$

Figure 5.9 shows the turbulent power number, N_p, for the autoclave. N_p generally varies between 2.8 and 3.2 for the Smith turbine. It can be observed that the power number here under un-aerated conditions was between 4.1 and 5.6, with the lower power numbers at the higher impeller speeds. These power numbers are higher than the typical literature values as reported for stirred tanks. Furthermore, the power number as seen for stirred tanks remains relatively constant for Reynolds numbers greater than 1000. The differences are believed to be due to the flow field generated as a result of the geometry of the autoclave and the chosen Smith turbine.

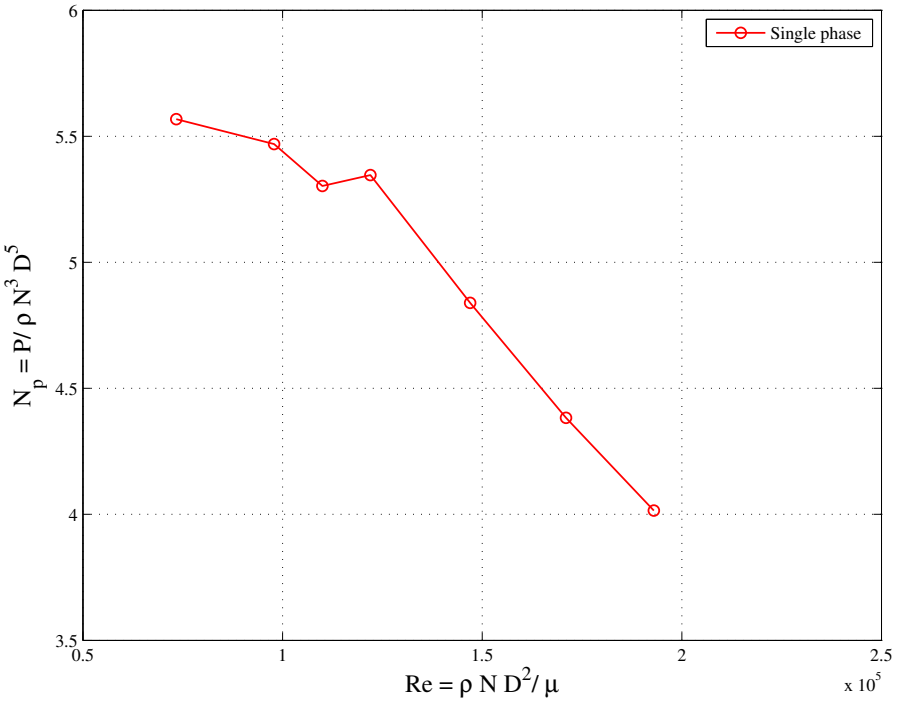

Figure 5.9: Power number - Experimental

5.1.2.2 Velocity flow field

The velocity flow field in mixing vessels is dependent on the vessel, baffles, type of impeller and also the position of the impeller shaft. The absence of baffles in stirred tanks produce rotary and laminar flow, which consequently adversely affects mixing (Rushton et al., 1994). Besides enhancing mixing, baffles also prevent the formation of surface vortices. The latter are also affected by the position of the impeller clearance from the bottom of the vessel (Galletti et al., 2009). The impeller clearance from the bottom of a vessel also influences the flow structure (Nienow, 1968). The geometry of the autoclave combines all of the above effects. The position of the impeller is eccentric since the vessel is asymmetric. With a curved bottom surface the position of the impeller relative to the bottom is not constant. This section covers the key features observed.

Figures 5.10 and 5.11 show the result from the PIV measurements at Plane 2 and 1 respectively. Figure 5.12 shows the predicted velocity flow field at Plane 1. At 150 rpm it can be observed that at Plane 2, which is in the centre of the tank, there are the two recirculation loops, one below and one above the impeller. However at Plane 1 the recirculation loop disappears. This is also captured by the CFD model as shown in Figure 5.12. The resulting flow field is mainly due to the shorter distance from the impeller to the wall of the vessel, which is larger at Plane 1.

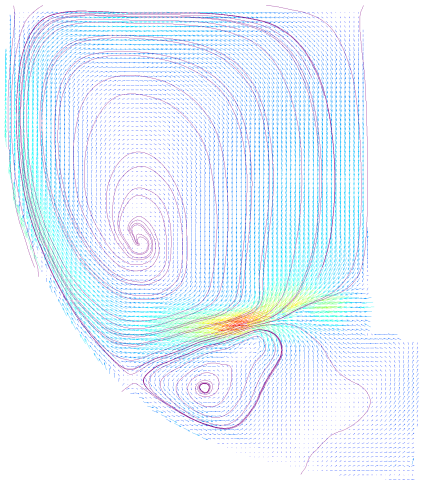

Figure 5.10: Velocity vectors on Plane 2 at 150 rpm - PIV

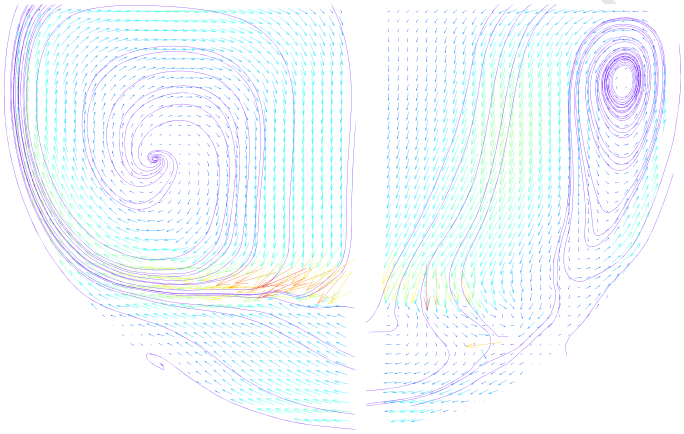

Figure 5.11: Velocity vectors on Plane 1 at 150 rpm - PIV

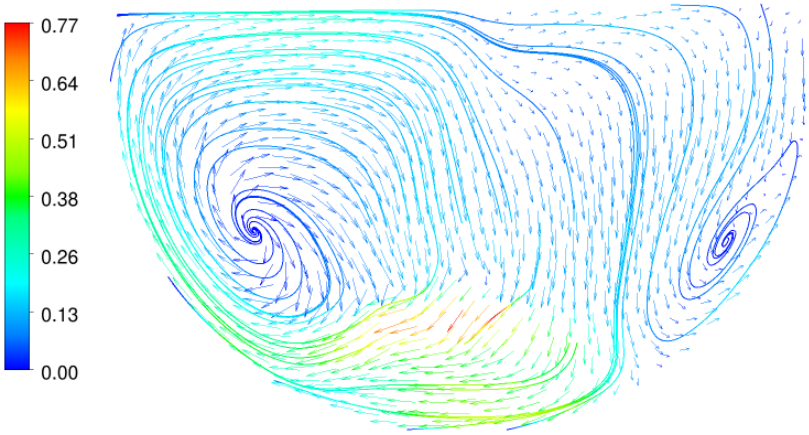

Figure 5.12: Velocity vectors on Plane 1 at 150 rpm - CFD

Figures 5.13 and 5.14 show the instantaneous predicted velocity vectors on a vertical plane in the center of the tank at 395 rpm and at two different impeller positions. The impeller blade is on the plane at Position 1 and the plane is midway between two impeller blades at Position 2.

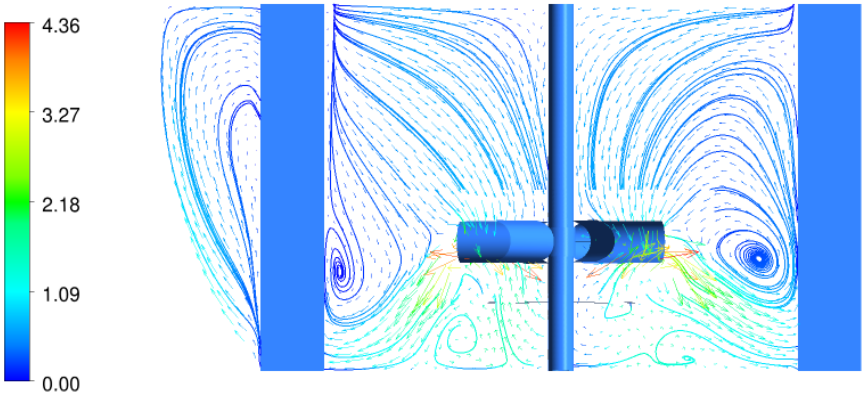

Figure 5.13: Velocity vectors on vertical plane across tank at Position 1 - CFD

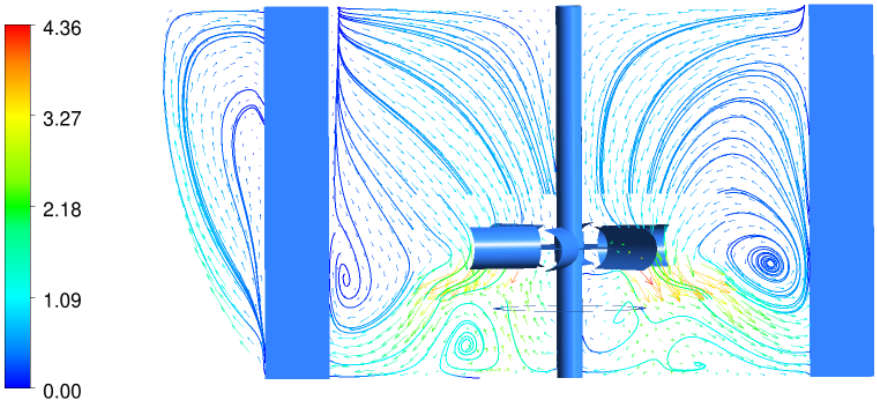

Figure 5.14: Velocity vectors on vertical plane across tank at Position 2 - CFD

There are two main observations; firstly the flow field is asymmetric and secondly the flow field close to the impeller is dependent on the impeller blade position. The asymmetry of the flow field is due to the geometry of the vessel and the effect of the shape of the impeller blade on the flow pattern. It is also observed that the lower recirculation loop disappeared on the right hand side of the vessel. The downward inflection of the fluid flow leaving the impeller is observed at Position 1 and Position 2. The angle of the radial flow to the horizontal is more pronounced than at 150 rpm. This is further explained in Section 5.1.3.2.

5.1.2.3 Turbulence parameters

Turbulence parameters in mixing tanks are usually given in terms of turbulent kinetic energy and dissipation rate. Turbulent kinetic energy, the energy associated with eddies in a turbulent flow, is expected to be high in the impeller region. This is mainly because of the large velocity gradients and fluctuations in that region. Turbulent dissipation rate is the rate at which mechanical energy transmitted by the impeller is dissipated locally by turbulence. It is often used to calculate rates of coalescence and breakage (Koh and Xantidis, 1999).

Figure 5.15 shows the contour plot of the CFD predicted turbulent kinetic energy on a vertical plane across the autoclave at 395 rpm. It can be observed that turbulent kinetic energy is unevenly distributed. It is higher in the impeller stream, because of the high velocity gradients in that region. However, in the bulk region it is irregular and asymmetric, mainly as a result of the velocity flow field and flow pattern.

In the impeller region it can be observed that the turbulent kinetic energy at 395 rpm is 1.23 Jkg^{-1}, equivalent to $0.1V_{tip}^2$. This is close to normally observed values in stirred tanks, for instance $0.07V_{tip}^2$ as reported by Shäfer et al. (1997).

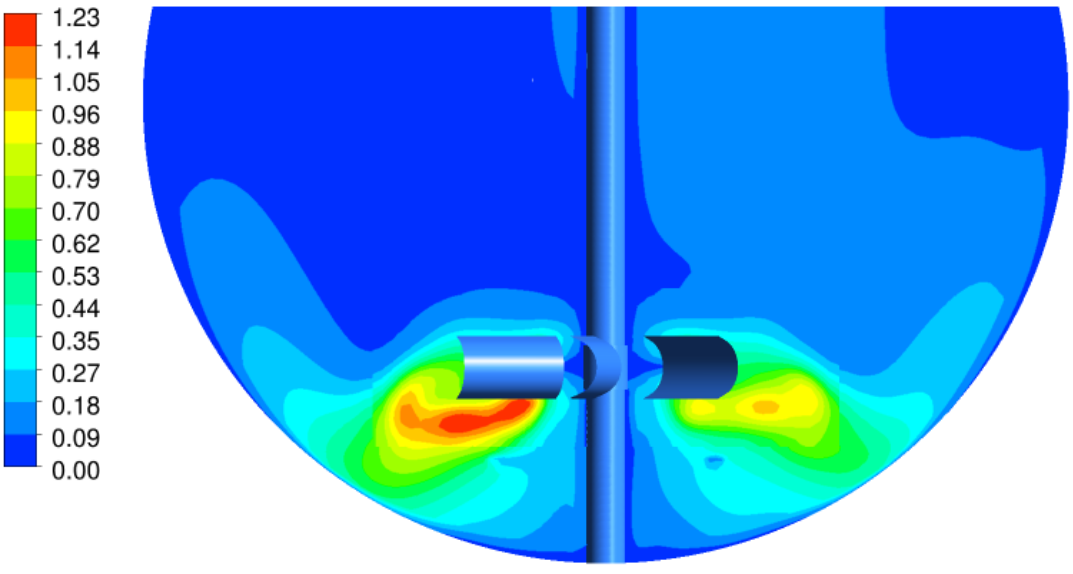

Figure 5.15: Turbulent kinetic energy on vertical plane across tank at 395 rpm - CFD

Figure 5.16 shows the contour plot of the CFD predicted turbulent dissipation rate at 395 rpm. The turbulent dissipation rate as expected is asymmetrical peaking in the impeller

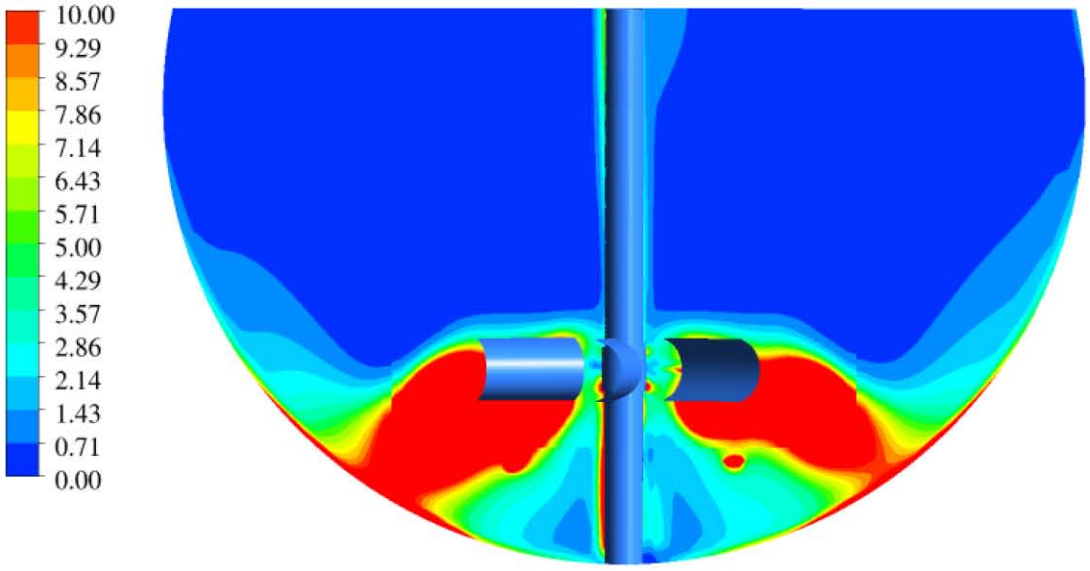

Figure 5.16: Turbulent dissipation rate on vertical plane across tank at 395 rpm - CFD

region and decreases to nearly zero in the rest of the vessel. The average power input at 395 rpm is about 2.5 kWm^{-3}. From Figure 5.16 is can be seen that most of the energy is dissipated in the impeller region and below. The average energy dissipated in the impeller region is about 54%, which is close to what is normally observed in stirred tanks with values varying between 30 and 60 % (Bakker, 1992; Deglon et al., 1998).

5.1.3 Effect of Impeller Speed on Hydrodynamics

The findings showing the effect of impeller speed on hydrodynamics, particularly on power draw, flow patterns and turbulent parameters, are presented and discussed in this section.

5.1.3.1 Power draw

The power draw as mentioned is a function of drag but is also dependent on the impeller speed. Power draw, as given by equation 5.1, is proportional to the cube of the impeller speed. Therefore, power is expected to increase at higher impeller speeds. This can be observed in Figure 5.1, with the power draw increasing from 0.01 kW to 0.13 kW when the impeller speed is increased from 150 rpm to 395 rpm.

5.1.3.2 Velocity flow field

The double loop structure for a stirred tank agitated with a Rushton turbine is commonly observed (Qi et al., 2012). However, with the autoclave the impeller speed was found to have some effects on the flow pattern. Figures 5.17-5.19 show the time averaged flow

patterns obtained in the center of the tank at three different impeller speeds; at 150, 200 and 250 rpm respectively.

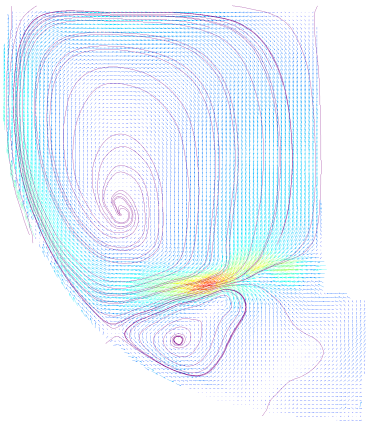

Figure 5.17: Velocity vectors at 150 rpm - PIV

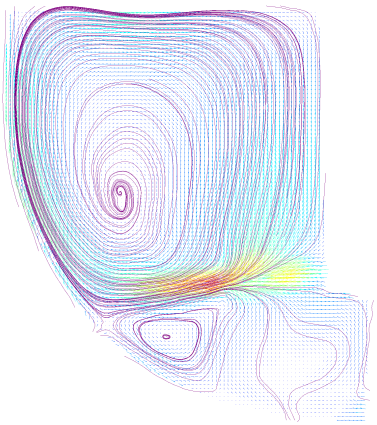

Figure 5.18: Velocity vectors at 200 rpm - PIV

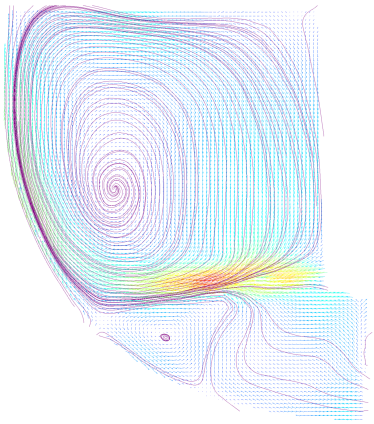

Figure 5.19: Velocity vectors at 250 rpm - PIV

The double loop structure is present for most cases. However, it is noticed that the angle of inclination of the impeller stream is different at the different impeller speeds. This is believed to be a result of the influence of the radial velocity component getting stronger. In addition, it can be observed that the double loops structure transitioned to a single-loop structure, with the weakening of the lower one. This change is normally observed when the impeller bottom clearance in stirred tanks, agitated with a radial impeller, decreases (Nienow, 1968; Montante et al., 2001). Therefore, it is suspected that the bottom surface has an effect on the fluid as seen by Deen et al. (2002) when a dished-bottom vessel is used.

5.1.3.3 Turbulence parameters

The effect of impeller speed on turbulent kinetic energy is shown in Figure 5.20. The profile was determined at a distance of 10 mm away from the impeller tip on Plane 2.

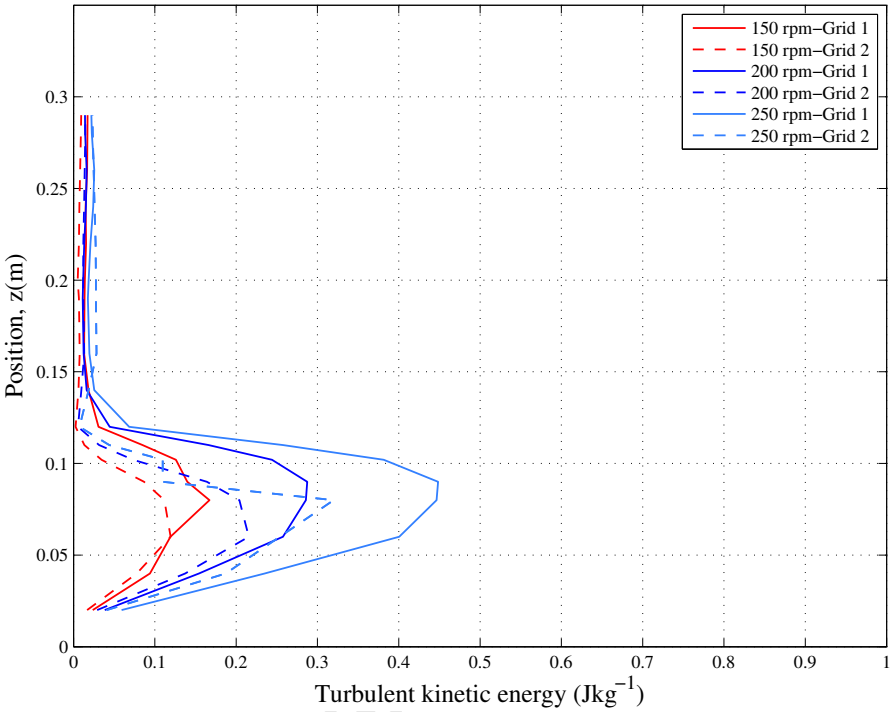

Figure 5.20: Effect of impeller speed on turbulent kinetic energy - CFD

It can be seen that as expected turbulent kinetic energy increases, from about 0.17 to 0.45 Jkg^{-1} for Grid 1, with increasing impeller speed and a subsequent increase in the magnitude of the velocity gradients of the fluid. It can also be observed that there is a difference in predictions using the two grids, which increases with impeller speed. Turbulent kinetic energy has often been found to be either under-predicted (Deen et al., 2002; Montante et al., 2001) or over over-predicted (Basara et al., 2004) and a finer mesh should improve the accuracy of the prediction. Therefore, it is suspected that Grid 1 over-predicted the turbulent kinetic energy and was enhanced by using Grid 2.

Figure 5.21 shows the turbulent dissipation rate profile. It can be observed that the turbulent dissipation rate is very high close to the impeller stream and decreases to nearly zero in the rest of the vessel. It also increased with impeller speed from about 2 to 15 m^{2}s^{-3} in the impeller region. It is suspected that the energy dissipation rate values were over-estimated with Grid 1 as seen for the prediction of the turbulent kinetic energy.

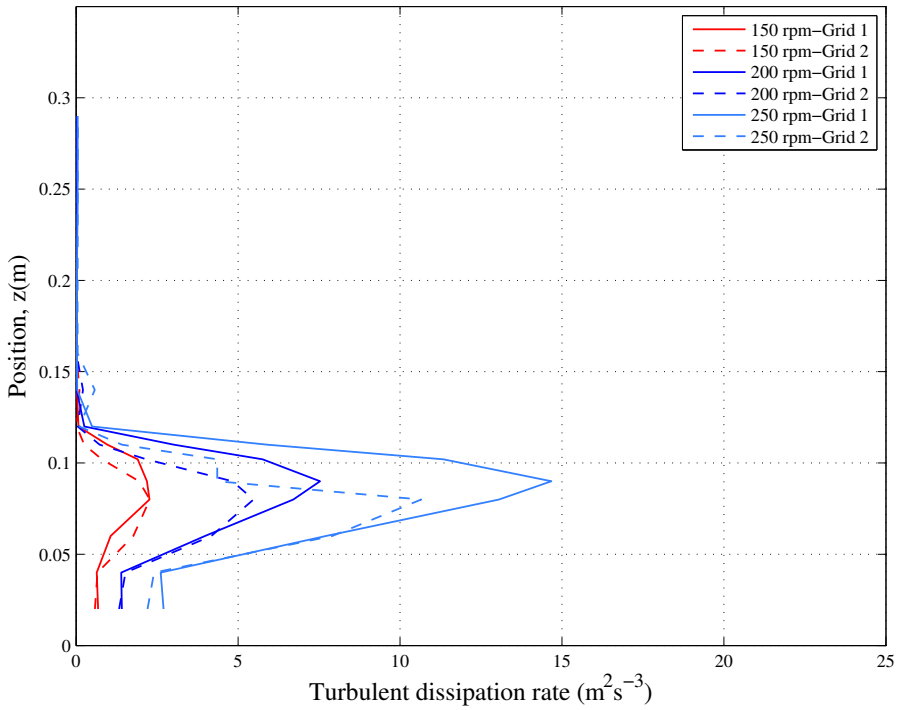

Figure 5.21: Effect of impeller speed on turbulent dissipation rate - CFD

5.1.4 Effect of Gas Dispersion on Hydrodynamics

The effect of gas dispersion on power draw, velocity flow field and turbulence parameters are presented in this section. The results for the velocity and turbulence parameters presented were obtained on a plane in the center of the tank, Plane 2 (defined in Figure 3.6(a)). Furthermore, the results for two impeller speeds are shown, that is at 200 and 395 rpm and with a gas flow-rate of 4.37 lmin^{-1}.

5.1.4.1 Power draw

Power draw is known to decrease under aerated conditions as a result of a drop in the pressure drag of the impeller blades. The decrease is due to the accumulation of gas behind the impeller blades, which form small pockets called gas cavities (Scargiali et al., 2007). Consequently, the pressure drops from the front of the blade to the inside of the gas cavities (Tatterson, 1991).

Figure 5.22 shows the effect of gas dispersion on power draw. It can be seen that there was a negligible difference between the oxygenated and un-gassed system. This is mainly a result of the gas flow-rates used which led to a low superficial gas velocity. The amount of gas accumulated behind the impeller was marginal and too low to induce any decrease in the power draw. Moreover, as will be further explained in Section 5.2.2.2 most of the gas

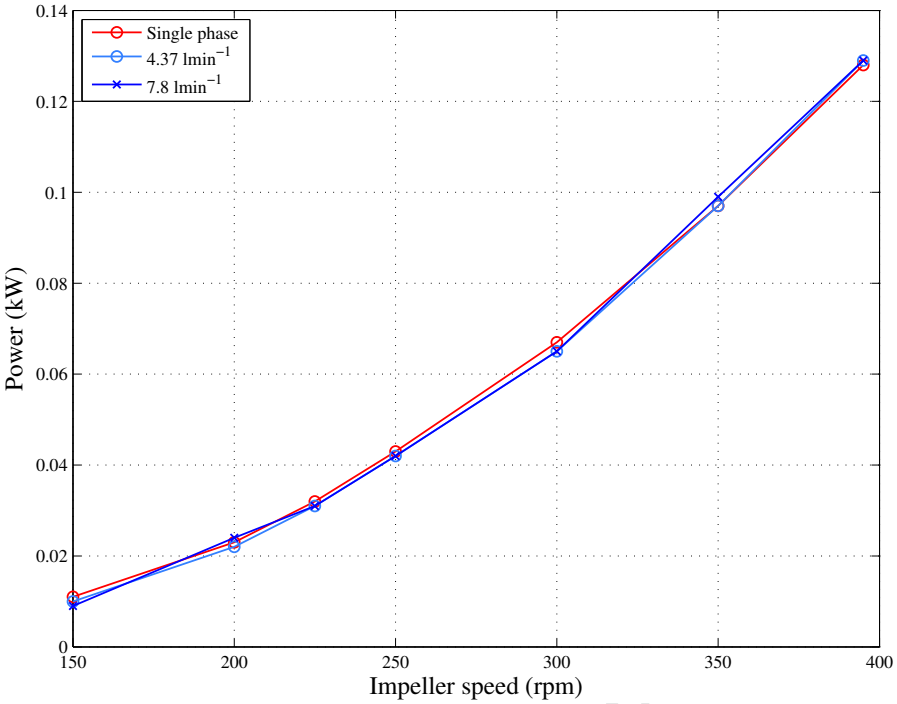

Figure 5.22: Effect of gas dispersion on power - Experimental

is trapped under the impeller disc and blade rather than accumulated behind the impeller blade. A similar trend is observed for the two flow-rates used.

5.1.4.2 Velocity flow field

Aeration usually leads to a decrease in mean velocity at the impeller tip (Deglon et al., 1998). Similar observations were made by Aubin et al. (2004b), where the CFD models showed that aeration either led to a drop in velocity or had a negligible effect on the velocity of water in mixing tanks.

The effect of gas dispersion on the velocity profile on Plane 2, based on CFD results, is illustrated is Figure 5.23. It can be observed that the velocity of water under oxygenated conditions are not highly influenced. The same profile is reproduced, with the flow at an angle to the horizontal and the same trend is observed for the three impeller speeds shown. It can be seen that the difference in velocities in the impeller region is small. This suggests that the impeller is still controlling the liquid flow and therefore even in the presence of gas the motion of bubbles will be controlled by the liquid flow pattern. This effect was similarly observed by Aubin et al. (2004b).

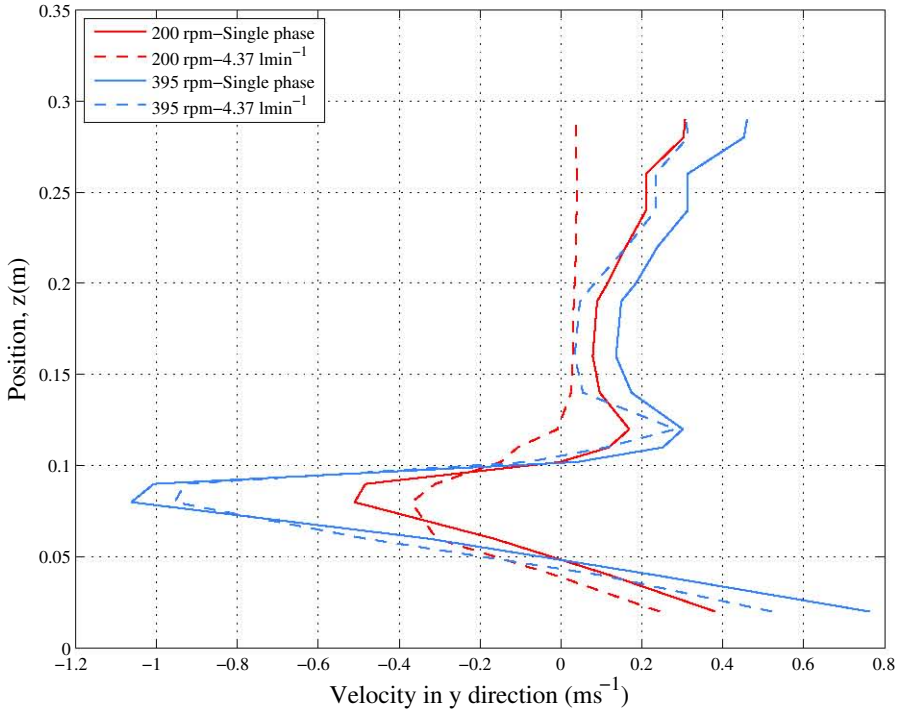

Figure 5.23: Effect of gas dispersion on velocity - CFD

5.1.4.3 Turbulence parameters

Turbulence parameters are also affected by aeration. Turbulent kinetic energy and energy dissipation rate in the impeller region were found to either remain constant or to increase (Deglon et al., 1998). For the turbulent energy dissipation the increase in the impeller region led to a decrease in the bulk of the tank.

Figure 5.24 shows the effect of gas dispersion on turbulent kinetic energy as predicted by the CFD model. It can be seen that there is a marginal increase in the bulk region. In the impeller zone, precisely where the fluid leaves the impeller, a drop in turbulent kinetic energy is observed. It is unclear whether the drop is a result of the dispersed k-ε model, which can result in numerical inaccuracies at a cell if the latter is mainly comprised of the secondary (gas) phase.

A similar observation is made for the prediction of the turbulence dissipation rate as shown in Figure 5.25. There is a negligible change in the bulk of the vessel upon aeration and a drop in the impeller region, where the velocity gradients are highest. The same trend is observed for the two impeller speeds presented.

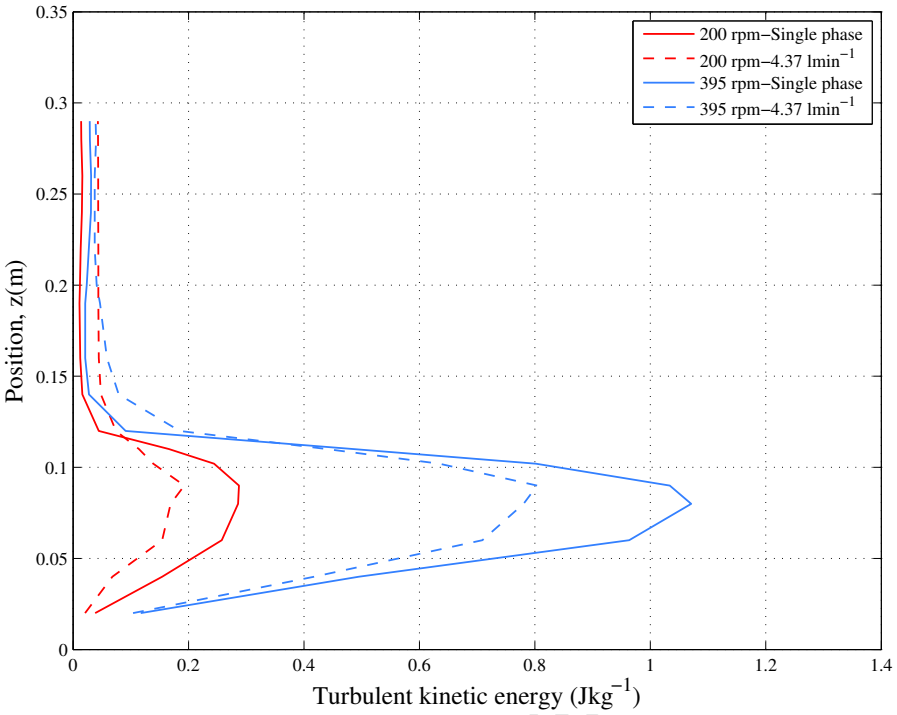

Figure 5.24: Effect of gas dispersion on turbulent kinetic energy - CFD

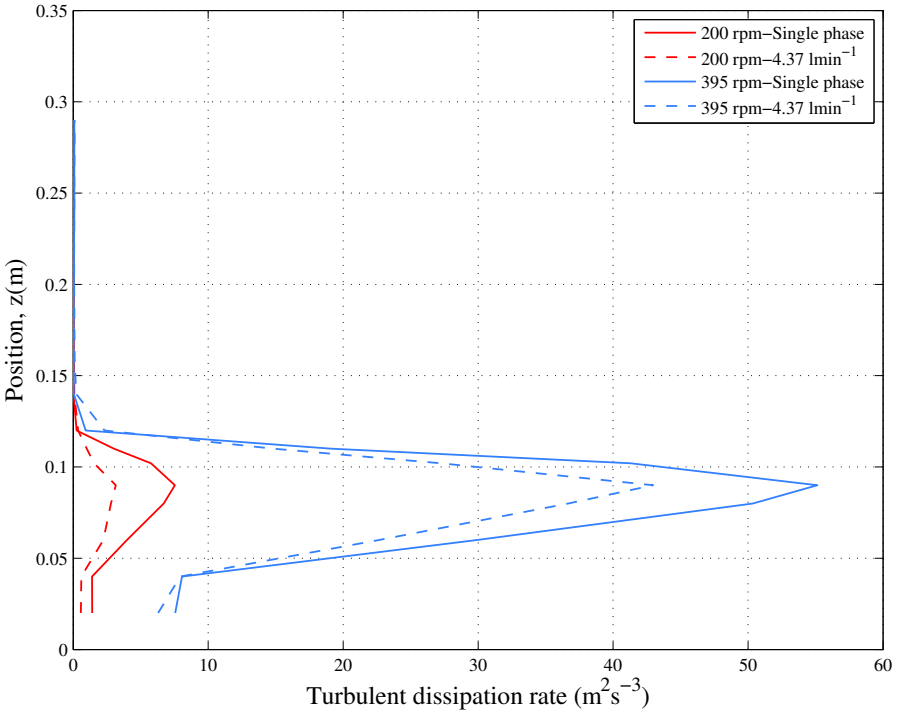

Figure 5.25: Effect of gas dispersion on turbulent dissipation rate - CFD

5.1.5 Implication of Hydrodynamics for Mass Transfer

Hydrodynamics can affect mass transfer on macro and micro levels. On a macro level, mass transfer is affected by the flow patterns, which consequently control the movement of bubbles. On a micro level, mass transfer is affected by turbulence, as the latter affects both bubble size and mass transfer coefficient, k_L. The influences of hydrodynamics on mass transfer are discussed in the following sections.

5.1.5.1 Power draw

Power draw is expected to affect mass transfer and an increase in power draw is expected to enhance k_La. An increase in power draw means an increase in the amount of energy transfered to the fluid. This will lead to an increase in k_L and therefore k_La. The increase in k_L is a result of an increase in turbulence dissipation rate which increases with power input (according to the eddy cell model, Equation 2.81)In addition, with an increase in the turbulent kinetic energy, more bubble breakage is expected, which will consequently increase the gas-liquid mass transfer.

5.1.5.2 Velocity flow field

The flow pattern as seen from Sections 5.1.3 - 5.1.2 is unusual. Mainly because of the geometry of the vessel and the type of impeller used. These gave rise to an asymmetrical flow field which is believed to result in a non-homogeneous system while the objective of the mixing process is to promote a well-mixed and homogeneous system. Besides the asymmetry of the flow pattern, the double-loop structure, commonly observed in stirred tanks agitated by a radial impeller, changed to a single-loop structure at high impeller speeds. In mixing vessels the lower recirculation loop helps movement of bubbles from the sparger to the impeller. However, with the flow patterns observed in the autoclave the motion of the bubbles is hindered and most of the oxygen bubbles are expected to be trapped under the impeller disc. This is further described and discussed in Section 5.2.6.2. In general, the flow field observed at the different impeller speeds investigated is expected to negatively affect mass transfer.

5.1.5.3 Turbulence parameters

Turbulence parameters also affect mass transfer as a result of the influence on both bubble size and k_L. Turbulent kinetic energy in eddies of a wave-length of the order of a bubble diameter controls bubble break-up. Therefore, regions of high turbulent kinetic energy are expected to promote smaller bubbles and consequently larger mass transfer.

It was found that the turbulent kinetic energy was heterogeneously distributed in the

vessel, peaking in the impeller region and also unevenly distributed in the bulk region. Bubble size is expected to be smaller in regions of high turbulent kinetic energies. k_La which is dependent on bubble size is expected to be higher close to the impeller and dissipates in the bulk.

Turbulence dissipation rate influences, k_L. But since ε follows a similar trend as k, the influence on k_La distribution would not be substantial since it is more dependent on a than k_L. An increase in impeller speed, which increases both parameters, k and ε, is expected to increase k_La.

5.2 Gas Dispersion

Gas dispersion was characterised in terms of bubble size as well as gas hold-up and the results are presented in this section. The CFD model was validated against experimentally measured Sauter mean diameter and is presented in Section 5.2.1. Furthermore, behaviour of gas dispersion under various conditions in the autoclave was investigated. In a mixing vessel the main physical parameters are; geometry of the vessel since it affects the flow pattern, gas flow-rate and impeller speed. The effect of temperature and electrolytes (synthetic leach liquor) on fluid properties was also investigated. The mentioned factors also affects gas hold-up. To this end the effect of different parameters on bubble size as well as gas hold-up were investigated. The findings and discussion are presented in Section 5.2.2 - 5.2.5. Finally, the implication of gas dispersion for mass transfer is discussed.

5.2.1 CFD Model Validation

The gas-liquid system was validated in terms of experimentally measured bubble size and gas-liquid mass transfer coefficient which is described in Section 5.3.1. This section covers the results for the numerical and bubble size validation.

5.2.1.1 Numerical

The numerical validation was based on bubble size and also on predictions of the velocity flow field for single phase flow. The grid resolution investigated, as observed, had a marginal influence on the prediction of the velocity flow field. Furthermore, the effect of grid resolution on the turbulence parameters, besides in the impeller region, were not substantial in most part of the vessel. In addition it was observed that the effect of gas dispersion on the hydrodynamics was also small. Based on these and the bubble size to grid size effect, which may have an influence on the numerical solution when using the dispersed k-ε model, Grid 1 was used. The two-phase system was simulated with the Euler-Euler model. The discrete method with the Luo breakage and coalescence models, coupled with the multiphase model, were used. The models gave good prediction of the bubble size as further described in Section 5.2.1.2.

5.2.1.2 Bubble size

Bubble size was modelled with a population balance model using the discrete method as described in Section 4.5.1. The results comparing numerical predictions and experimental values of Sauter mean diameter at a gas flow-rate of 4.37 $lmin^{-1}$ are depicted in Figure 5.26.

From Figure 5.26 it can be observed that the experimental and predicted Sauter mean diameter are comparable over the range of impeller speeds investigated, with an average error of 4% and a maximum error of 12%. The result shows that the discrete model accurately predicts the bubble size distribution with 11 classes. It is believed that 11 classes were sufficient to accurately model the bubble size because of the small variation in the diameter of the bubbles, which was between 1 mm and 6.6 mm for the impeller speeds investigated. It can also be observed that there is an unusual increase in bubble size with increasing impeller speeds. The latter is believed to be due to a coalescence driven mixing process in the autoclave and is further discussed in Section 5.2.3.

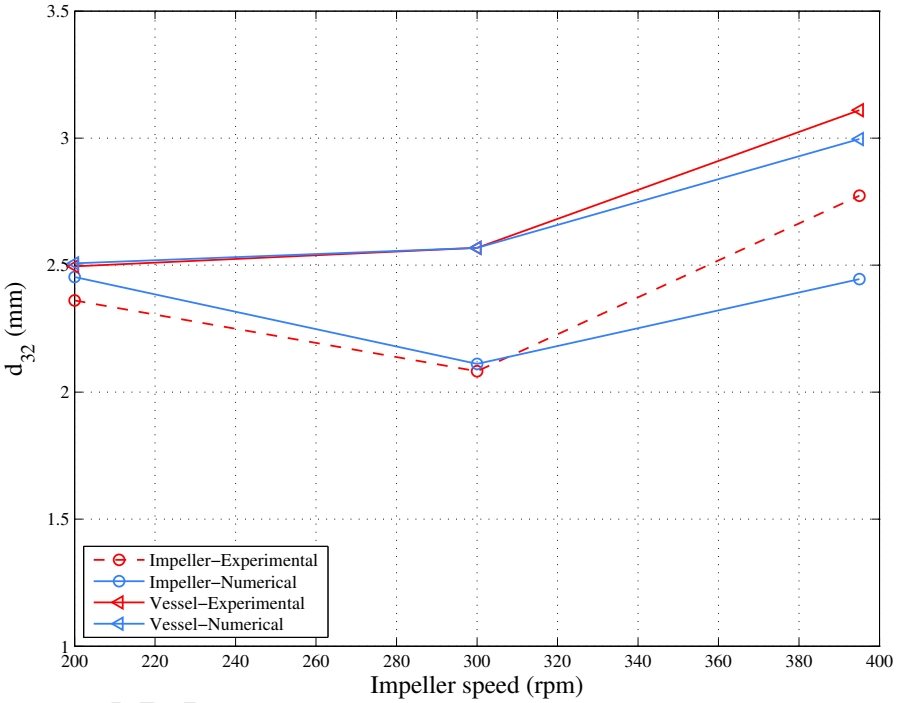

Figure 5.26: Sauter mean diameter (mm) at 4.37 lmin^{-1} - CFD and Experimental

Table 5.1: Sauter mean diameter (mm) at 7.8 lmin^{-1}- CFD and Experimental

N (rpm)	d_{32}**-Exp (mm)**	d_{32}**-CFD (mm)**
200	2.985	2.521
395	3.432	3.153

The model was further validated at a gas-flow rate of 7.8 lmin^{-1}. It can be seen that the model reasonably predicted bubble size in the vessel, with a maximum error of 20%. The relatively larger error at 7.8 lmin^{-1} is believed to be a result of the number of classes used, which could have been insufficient since the difference between the maximum and

minimum bubble size was larger at this flow-rate. This was also highlighted by Montante et al. (2008) where the Sauter mean diameter was under-estimated by about 50% and the discrepancy was attributed to the bubble size interval. From the findings it can be seen that the population model predicted the bubble size generally well, given that they were obtained based entirely on fundamental models with no fitted coefficients.

5.2.2 Effect of Geometry on Gas Dispersion

The geometry of the vessel as observed in Section 5.1.2 has an effect on hydrodynamics, particularly on the flow pattern. This is expected to reflect on gas dispersion since the motion of gas depends on the flow field of the liquid phase. Therefore, the effect of geometry on bubble size and gas dispersion was investigated and is presented in this section.

5.2.2.1 Bubble size

Local hydrodynamic properties, which varies throughout the tank, highly influences bubble size. For a stirred tank in the region below the impeller, bubble diameter as observed by Greaves and Barigou (1992) is expected to increase as a result of coalescence. Bubble size is also expected to increase in the region away from the impeller. Smaller bubbles are expected close to the impeller as a result of the high-shear in that region which increase in size, due to coalescence, as they leave the impeller region. The bubbles in the bulk region are relatively larger and increases to reach a 'bulk value' as reported by Greaves and Barigou (1992) and Alves et al. (2002).

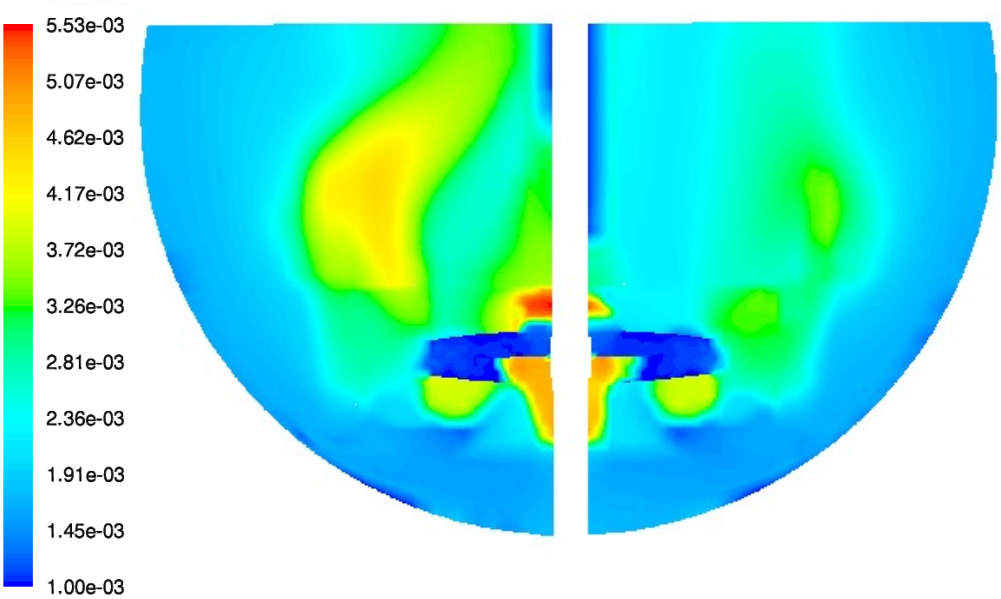

Figure 5.27: Local Sauter mean diapmeter (m) on a vertical plane at 395 rpm

For the autoclave investigated oxygen gas was sparged below the impeller and bubble diameter at the sparger was approximately 2 mm. The local Sauter mean diameter on a vertical plane in the center of the vessel is illustrated in Figure 5.27. Below the impeller it can be seen that the bubbles leave the sparger with a diameter of 2 mm and then increase in size, as a result of coalescence, as they move toward the impeller. In the region closer to the impeller where the turbulent kinetic energy is higher, which consequently results in a high breakage rate, the bubbles are smaller. Furthermore, in the bulk region bubbles of diameters larger than 2 mm are noticeable mainly as a result of coalescence. The latter is a consequence of the larger number of bubbles trapped in the recirculation loop. In addition, it can be observed that most bubbles are of diameters larger than 2 mm with small breakage in the impeller region. The CFD results supports the experimental findings, as illustrated in Figure 5.28, which shows that gas dispersion is coalescence controlled at high impeller speeds.

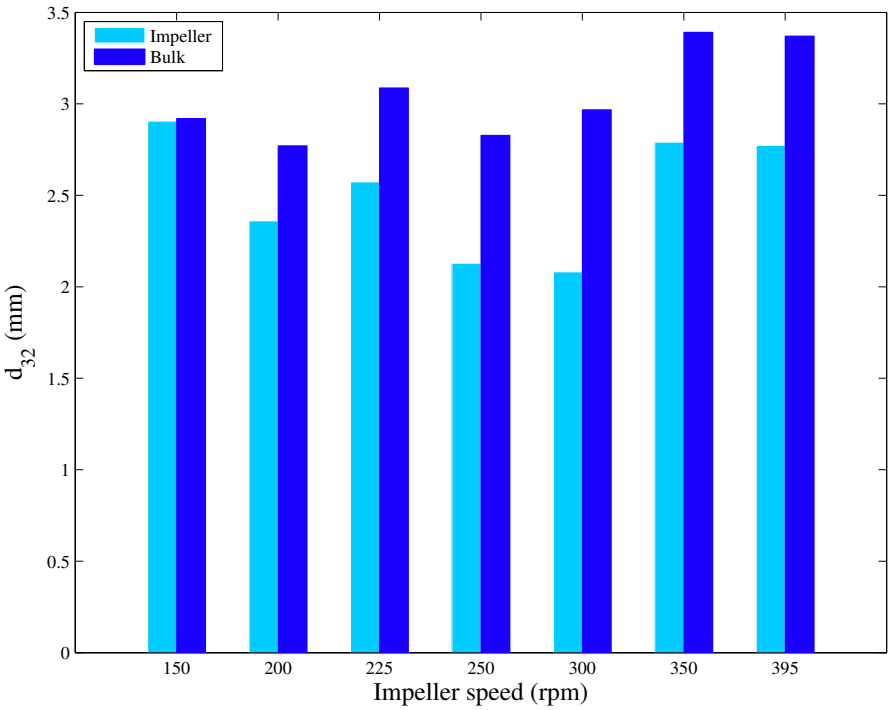

Figure 5.28: Sauter mean diameter in bulk and impeller region - Experimental

Figure 5.28 shows the Sauter mean diameter in two different regions in the tank; bulk and impeller region. It can be seen that bubble diameter in the impeller stream varies between 2 and 3.2 mm suggesting some coalescence has occurred in the region below the impeller.

It is clear that bubble size in the impeller region is smaller than in the bulk region, which is a result of the larger turbulent energy dissipation rate close to the impeller. The increase in bubble diameter in the bulk region is as a result of coalescence. When the

bubbles leave the outflow of the impeller they are carried by the fluid flow and the larger number of bubbles in the recirculation loops lead to a higher probability of coalescence. A similar trend, as seen when the entire tank is considered, is followed in both regions, with a slight decrease for the lower agitation speeds and an increase from 250 rpm onward. This suggest that at low impeller speeds gas dispersion is affected by breakage and at the higher impeller speed coalescence is dominant. This could be a result of a higher agitation and recirculation rate at higher impeller speeds.

5.2.2.2 Gas hold-up

Contour plots of instantaneous volume fraction of oxygen on a vertical plane in the centre of a tank are shown in Figures 5.29 and 5.30.

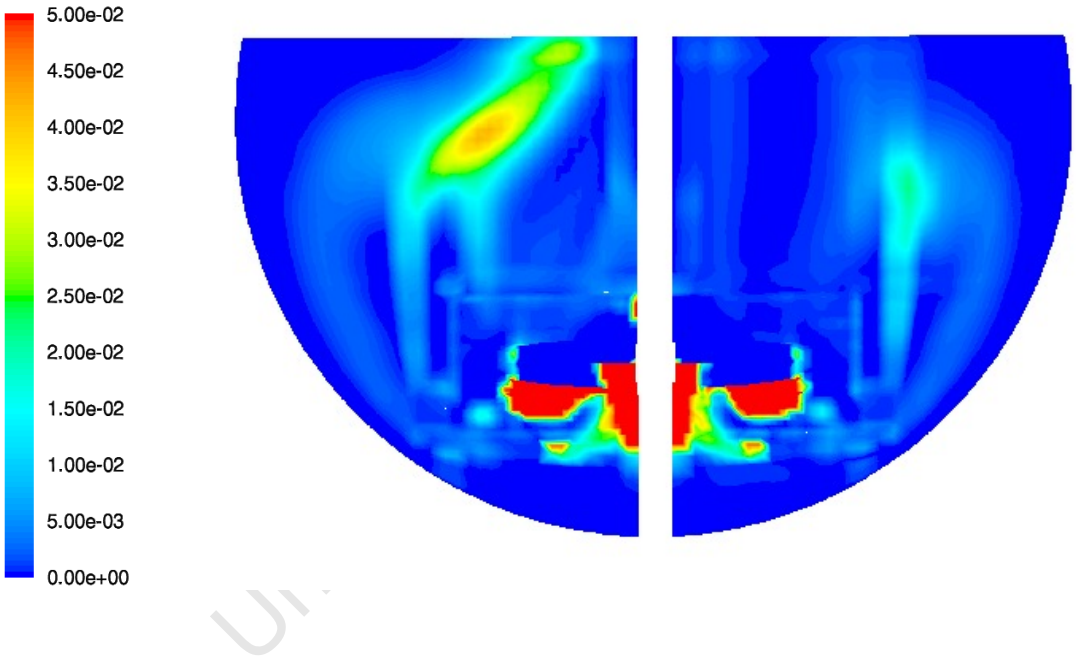

Figure 5.29: Gas hold-up on a vertical place at 395 rpm and flow-rate of 4.37 lmin^{-1}

Figure 5.29 is for a case where a gas flow-rate of 4.37 lmin^{-1} at an impeller speed of 395 rpm was used. For the different cases investigated the gas hold-up values were found to be relatively low, mostly below 1%, when compared to stirred tanks. This is mainly because of the low superficial gas velocity used. Gas hold-up is normally expected to increase with the presence of small bubbles, however since the system is coalescence controlled gas hold-up is expected to be adversely affected. The low gas hold-up can also be due to the poor gas dispersion. It can be observed that gas distribution is non-uniform, with most oxygen trapped under the impeller. This is thought to have been exacerbated as a result of the weakening of the lower recirculation loops, which if present would have helped bubbles move to the impeller blades more easily. The asymmetrical flow patterns also contributed

to a heterogeneous mixture. There are large regions of the autoclave where there is little or a negligible amount of gas.

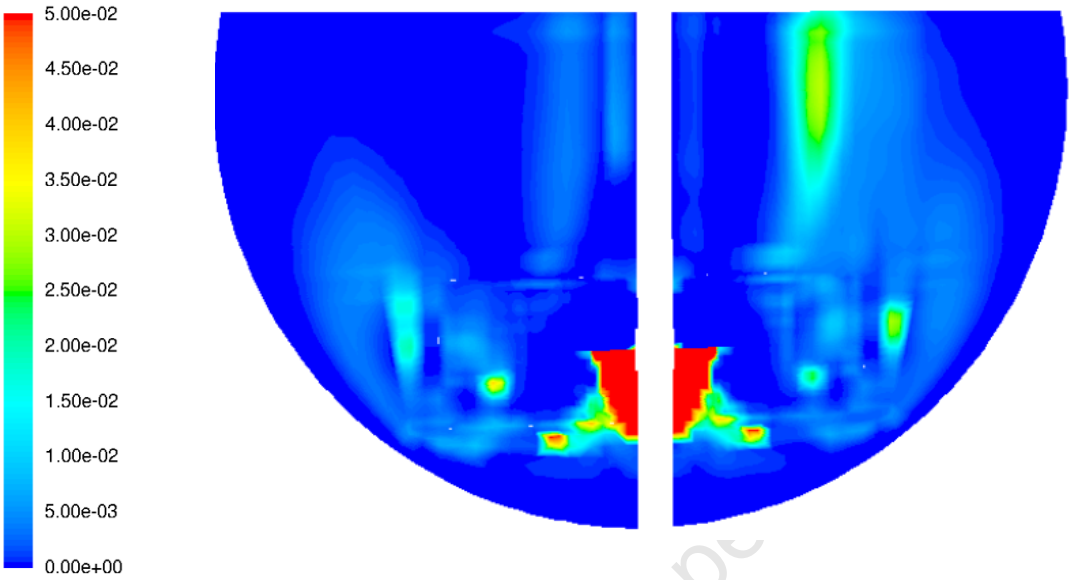

Figure 5.30: Gas hold-up on a vertical place at 395 rpm and flow-rate of 7.8 lmin^{-1}

Gas hold-up is normally expected to increase at high gas flow-rates. However, with the current system gas dispersion is expected to remain poor. From Figure 5.30, which shows the gas distribution at a gas flow-rate of 7.8 lmin^{-1} and at impeller speed of 395 rpm, it can be seen that no improvement in the dispersion was achieved. Most of the gas is trapped under the impeller disc, even more than observed at 4.37 lmin^{-1} for which the gas was mostly under both impeller blades and disc. In the other regions the gas distribution was generally the same. The poor distribution is not expected to improve at even higher impeller speeds since the flow pattern should not change drastically.

5.2.3 Effect of Impeller Speed on Gas Dispersion

In general bubble size is expected to decrease with increase in impeller speed as a result of a larger turbulent kinetic energy distribution, with promotes breakage and hence smaller bubbles. However, as observed by Greaves and Barigou (1992) as well as Laakkonen et al. (2005) the effect of impeller speed on bubble size is more complex. It is dependent on factors such as the location of the bubbles and the degree of homogeneity agitation promotes. Gas hold-up is expected to increase with impeller speed as a result of the formation of smaller bubbles at higher impeller speeds. The effect on impeller speed on gas dispersion in the autoclave is presented in this section.

5.2.3.1 Bubble size

Figure 5.31 shows the effect of impeller speed of bubble size in the vessel as well as the comparison between numerical and experimental results. The trends from Figure 5.31 have characteristics that are both expected and unexpected. For speeds varying between 150 and 250 rpm there is a general reduction in the Sauter mean diameter.

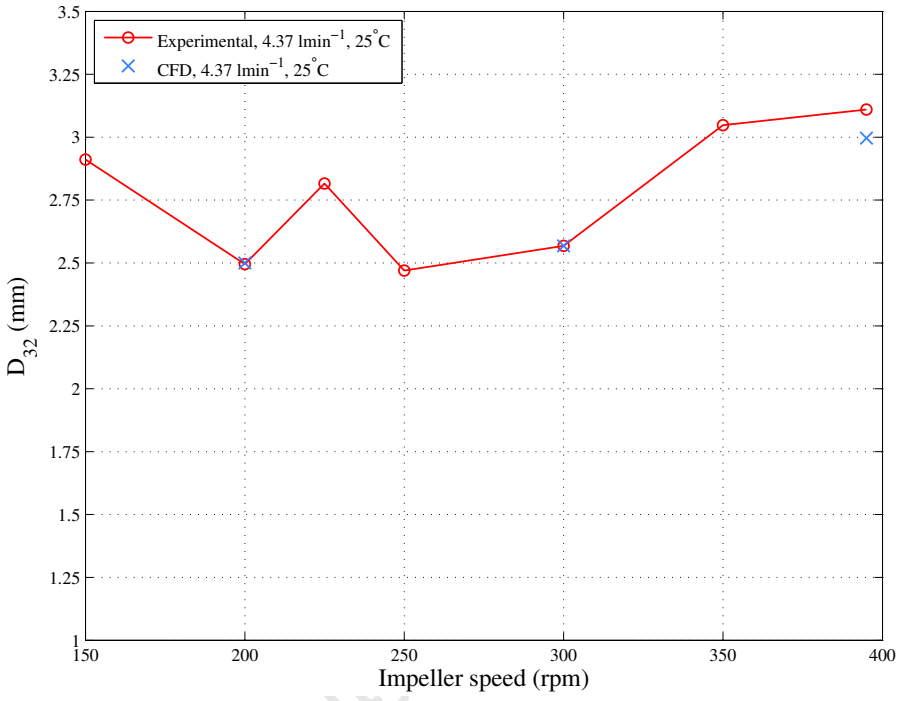

p

Figure 5.31: Effect of impeller speed on bubble size in tank - Experimental and Numerical

However, for the higher impeller speeds an increase in bubble size is noticed. This trend was similarly observed by Gorain et al. (1995) showing that the bubble size decreases with impeller speeds but with anomalies at high impeller speeds. This was attributed to the increase in internal recirculation at high impeller speed which increased coalescence. As seen in Figure 5.31 for speeds above 250 rpm, there is an increase in bubble size, showing that the higher speeds resulted in higher recirculation rates. This resulted in an increase in the probability of collision promoting coalescence and thus leading to the increase in Sauter mean diameter. However, overall bubble size remained between 2.5 and 3.25 mm and is not strongly affected by impeller speed.

5.2.3.2 Gas hold-up

Gas hold-up in mixing vessels as mentioned earlier is affected by various factors and is commonly represented by the following equation (Harnby et al., 1992):

$$\varepsilon_G \propto (P_g/V_L)^A (v_s)^B \tag{5.2}$$

According to equation 5.2 gas hold-up is proportional to the gassed power input and therefore impeller speed. Gas hold-up is expected to rise with impeller speed as a result of a decrease in bubble size.

Table 5.2: Gas hold-up (-) at 4.37 lmin^{-1} - CFD

N (rpm)	Gas hold-up (-) - CFD
200	0.0014
300	0.0027
395	0.0031

From Table 5.2 it can be seen that the gas hold-up values were all below 1%. This is due to the low superficial gas velocity used, as explained earlier. An increase in gas hold-up is observed with an increase in impeller speed. This is explained by the higher gas recirculation rate at higher impeller speeds.

5.2.4 Effect of Gas Flow-rate on Gas Dispersion

Bubble size is dependent on gas flow-rate, or superficial gas velocity. Authors such as O'Connor et al. (1989) and Dobby and Finch (1986) showed that the bubble size in laboratory columns is expected to increase at higher gas flow-rates. Similar effects were observed by Laakkonen et al. (2005) and Greaves and Barigou (1992).

5.2.4.1 Bubble size

The Sauter mean diameter, which is based on the surface area per unit volume of the bubbles, at two different gas flow rates, 4.37 lmin^{-1} and 7.8 lmin^{-1}, is shown in Figure 5.32.

It can be observed that bubble size was not greatly affected by the gas flow-rate. The average increase in Sauter mean diameter observed was between 10 and 20% for the impeller speeds investigated. A similar trend, not presented here, was observed in both the

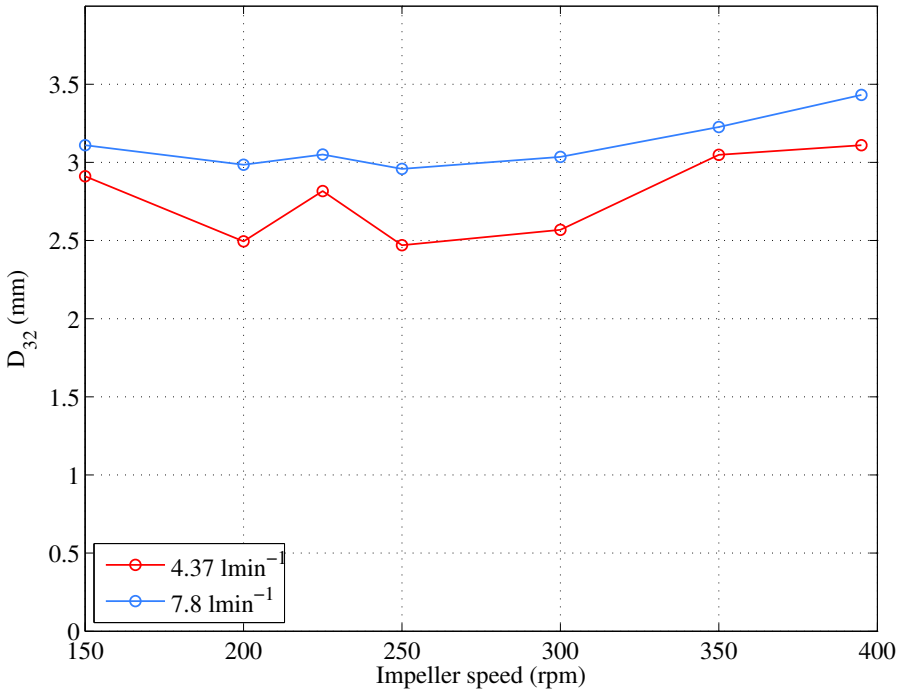

Figure 5.32: Effect of gas flow-rate on bubble size in tank - Experimental

bulk and impeller region. The results also show that coalescence is not negligible even with the relatively low gas flow-rates used for this study.

5.2.4.2 Gas hold-up

An increase in gas flow-rate and therefore in superficial gas velocity is expected to give rise to an increase in gas hold-up.

Table 5.3: Gas hold-up (-) - CFD

N (rpm)	Gas Hold-up (-) at	
	4.37 lmin^{-1}	7.8 lmin^{-1}
200	0.0014	0.0042
395	0.0031	0.0040

Table 5.3 shows the predicted gas hold-up values at two different flow-rates. It is clear that gas hold-up increased with gas flow-rates. At 7.8 lmin^{-1} the gas hold-up is expected to nearly double or be less than the value at 4.37 lmin^{-1}. This is observed at 395 rpm but at not 200 rpm. The higher than expected gas hold-up value at 200 rpm is suspected to be due to a larger accumulation of gas below the impeller at that speed.

5.2.5 Effect of Fluid Properties on Gas Dispersion

Gas dispersion is known to be affected by fluid properties. The effect of temperature and ions by using a synthetic leach liquor on bubble size were investigated and the results as well as discussion are presented in this section.

5.2.5.1 Bubble size

Bubble size is known to be influenced by temperature. This is usually due to a decrease in factors such as the surface tension and viscosity as temperature increases. The decrease in viscosity can lead to a faster rate of formation of the liquid film at the point of bubble formation, as mentioned by O'Connor et al. (1989), resulting in less oxygen being trapped in each bubble and therefore producing smaller bubbles.

Besides temperature are other factors that can affect bubble size, among which are changes in pH, viscosity and effect of ions. O'Connor et al. (1989) reported that an increase in pH led to an increase in bubble size and an increase in ionic effect resulted in a decrease in bubble size. Therefore, bubble size will be dependent in the dominant factor.

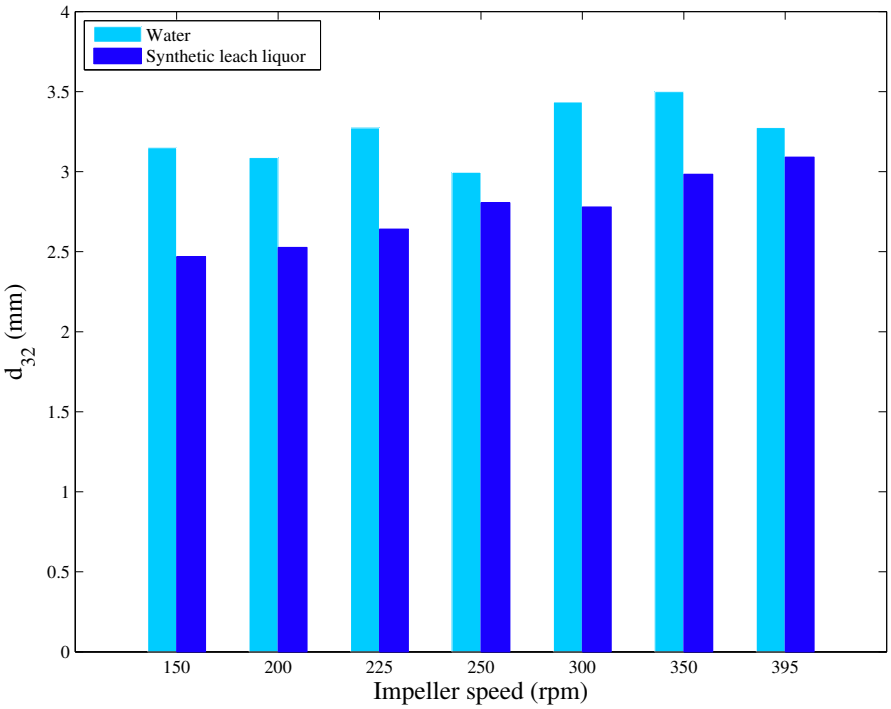

Figure 5.33: Effect of synthetic leach liquor on bubble size in bulk region - Experimental

Figure 5.33 shows the comparison between bubble size at 25°C for water and the synthetic leach liquor. The results are for bubbles obtained at a flow-rate of 7.8 lmin^{-1} in the bulk region. It can be seen that there is a general decrease in the bubble size for the synthetic

leach liquor as was similarly observed by Harnby et al. (1992). The drop in bubble size observed here is a result of the ions found in the solution, which was composed of 40 g/l Ni, 70 g/l Cu and 10 g/l H_2SO_4. The ions in the system inhibit coalescence in much the same way as surfactants such as chemical frothers. The viscosity of the synthetic leach liquor as determined from the OLI StreamAnalyser 3.0 software was 1.72×10^{-3} kgms^{-1} at 25°C, which is about twice the viscosity of water. Since an increase in viscosity is expected to lead to an increase in bubble size, the results further show that the effect of the ions was the dominant factor causing the drop in bubble size.

5.2.6 Implication of Gas Dispersion for Mass Transfer

Mass transfer is highly affected by gas dispersion, especially bubble size. A smaller bubble size is expected to result in a larger surface area and consequently larger gas-liquid mass transfer coefficient, k_La. Regions with high gas hold-ups will lead to higher k_La values. The implications of local bubble size and gas hold-up on mass transfer are described in Section 5.2.6.1 - 5.2.6.2.

5.2.6.1 Bubble size

Based on the findings it was found that bubble size was affected by factors such as geometry of the vessel, impeller speed, gas flow-rate and fluid properties. Since k_La is highly affected by the bubble size, the factors mentioned above will influence mass transfer. The system was found to be predominately controlled by coalescence with little breakage close to the impeller. Therefore, mass transfer is expected to be high in the region close to the impeller and decreases in the bulk region. Increase in impeller speed initially led to a decrease in bubble size and then was primarily dominated by coalescence after 300 rpm. This is expected to result in an increase in mass transfer and then a drop after 300 rpm.

An increase in flow-rate as observed led to an increase in bubble size and this is expected to result in a decrease in k_La. The latter is however also affected by gas hold-up which increases with gas flow-rate as a result of a bigger effect on a. Therefore, mass transfer will increase with gas flow-rate. Furthermore, both temperature and ionic effects were found to influence bubble size with a slight drop. These are expected to lead to an increase in k_La values.

5.2.6.2 Gas hold-up

Gas hold-up was found to be low, less than 1%, in most cases. The distribution of gas in the system was poor, with regions with practically no oxygen. Likewise, mass transfer is expected to be unevenly distributed and very small in some regions.

The other factors that affect gas hold-up are impeller speed, gas flow-rate and also the presence of electrolytes. An increase in either gas flow-rate or impeller speed would result in an increase in gas hold-up and consequently k_La. Gas hold-up is dependent on bubble size, a decrease in bubble size is expected to result in an increase in gas hold-up and vice versa. Bubble size, as explained in Section 5.2.5.1, is expected to decrease with temperature and consequently lead to an increase in gas hold-up. However, contradicting findings have been observed, with both increase and decrease in gas hold-ups, as temperature increases (Ribeiro-Jr and Mewes, 2006). For instance, gas hold-up decreased with

temperature for the studies carried out by Zhu and Wu (2004) and Shaper et al. (2002). Therefore, temperature can either lead to a decrease or an increase in k_La as far as gas hold-up is concerned. The presence of electrolytes is known to lead to an increase in gas hold-up as a result of a decrease in bubble size (Hassan and Robinson, 1977). Therefore, k_La is expected to increase in the presence of electrolytes.

5.3 Mass Transfer

This section deals with the results and discussion of gas-liquid mass transfer, k_La in the pilot scale autoclave. The validation of the CFD model predicting k_La is presented in Section 5.3.1. Various factors affect k_L and a, which in turn influence k_La. These factors were investigated and results as well as discussion are presented in Sections 5.3.4 - 5.3.5. Power law correlations are also commonly used to estimate k_La. The correlations are known to be affected by the geometry of both vessel and impeller as well as operating conditions. As a basis for future work an empirical correlation for the lab-scale autoclave was developed and the results are presented and discussed in Section 5.3.6. From the results presented in the different sections, it will be observed that the k_La values is relatively lower, with values varying between 0.003 and 0.024 s^{-1}, when compared to 0.01 and 0.35 s^{-1} as reported by Nicolle et al. (2009). The lower values is due to the low superficial gas velocities used. k_La would increase with gas flow-rate but the quality of gas dispersion, hence k_La, would remain poor.

5.3.1 CFD Model Validation

Numerical modelling of gas-liquid mass transfer coefficient, k_La, can generally be done in two ways; by either simulating gas-liquid systems with a constant bubble size or by using bubbles of various sizes with the aid of a population balance model. For validation purposes mass transfer was predicted using both methods.

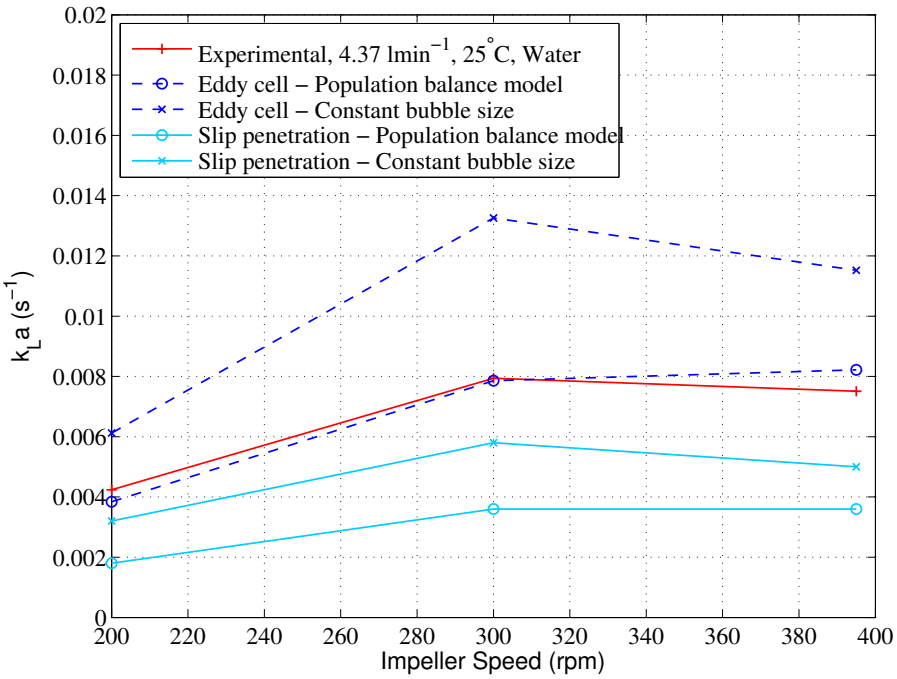

Figure 5.34: k_La at 4.37 lmin^{-1} - CFD and Experimental

Furthermore, as explained in Section 4.7.3, gas-liquid mass transfer was modelled by determining both a and k_L. The latter was calculated using either the slip penetration model or the eddy cell model. The models and constant used for the numerical predictions are explained in Section 4.7.3. Figure 5.34 shows the results comparing numerical predictions, which includes the different methods mentioned above, and experimental data for the gas-liquid mass transfer coefficient, k_La. It can be seen that there were some discrepancies, which were within a 67% error margin, between the predicted k_La and experimental data. However, the eddy cell model with the population balance model gave the best prediction of k_La. The model fitted the experimental data with an average error of 6.2%. These were considered more than acceptable overall given that the predicted k_La values were obtained using fundamental models. An over-prediction was observed when using the eddy cell model and a constant bubble size. On the other hand an under-prediction was obtained with the slip penetration model when either using a constant bubble size or the discrete method.

Table 5.4: k_La at 7.8 lmin^{-1}- CFD and Experimental

N (rpm)	$\boldsymbol{k_La}$**-Exp** ($\mathbf{s^{-1}}$)	$\boldsymbol{k_La}$**-CFD** ($\mathbf{s^{-1}}$)
200	0.0056	0.0058
395	0.0124	0.0110

The model was further validated at a gas flow-rate of 7.8 lmin^{-1} and at two impeller speeds. The results using the eddy cell model are shown in Table 5.4. It can be observed that the model satisfactorily predicted k_La at 7.8 lmin^{-1}, with an average error of about 7.5%.

From the set of results it can be seen that the eddy cell model with a full bubble size distribution was more appropriate to predict gas-liquid mass transfer in the autoclave. The full bubble size distribution is more appropriate as it accounts for bubbles of all sizes. The eddy cell model is more suitable that the slip penetration model because of the inherent turbulent flow in the vessel. The slip penetration model would be more convenient for a bubble column type system, where slip velocity is predominant.

5.3.2 Effect of Geometry on Mass Transfer

Gas-liquid mass transfer is affected by two main factors, hydrodynamics and gas dispersion. The two phenomena as observed are affected by the geometry of the vessel. In stirred tanks, k_La is high in regions with small bubbles, usually close to the impeller, and where gas hold-up is high as seen in the typical recirculation loops. These effects are mainly as a result of the flow pattern, generated by the geometry of the vessel, which also controls the motion of bubbles. The flow pattern as observed is asymmetric in the autoclave which resulted in a poor gas distribution and in a system with most of the gas trapped below the impeller.

Figures 5.35 and 5.36 show the prediction of local k_La using the eddy cell model and the slip penetration model respectively. The results are shown for a vertical plane at 395 rpm and a gas flow-rate of 4.37 lmin^{-1}.

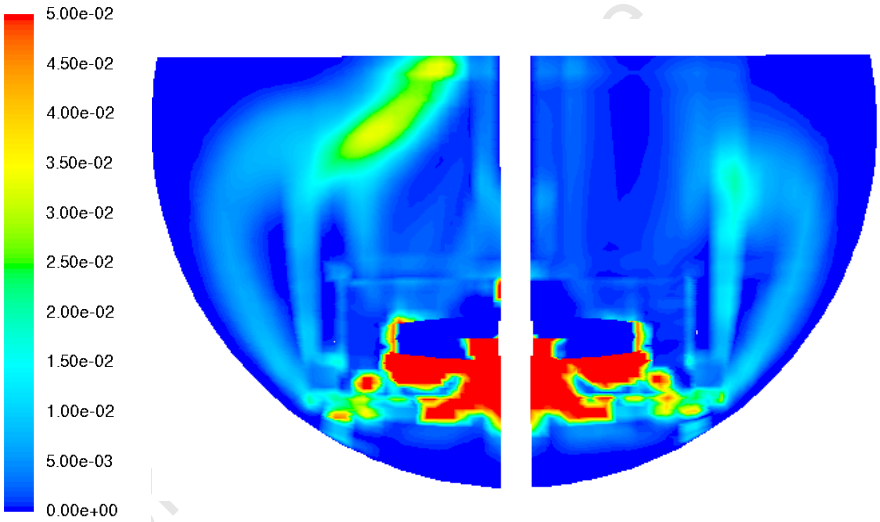

Figure 5.35: k_La with eddy cell model on a vertical plane at 395 rpm

It can be seen that k_La is qualitatively poor. The distribution of gas-liquid mass transfer is uneven, with the highest values under the impeller, where gas is trapped, and dissipates through the tank via the recirculation loops. It is also clear that there are large regions of near zero mass transfer. These are different to the distribution of gas-liquid mass transfer in stirred tanks, agitated with a radial impeller, which even though is normally heterogeneous is better distributed in the bulk region (Gimbun et al., 2009) than observed here. This poor distribution is a result of the flow field and gas dispersion in the autoclave.

At higher gas flow-rates, even though k_La is expected to increase with the higher superficial gas velocities, the distribution of k_La would still be poor because of the flow

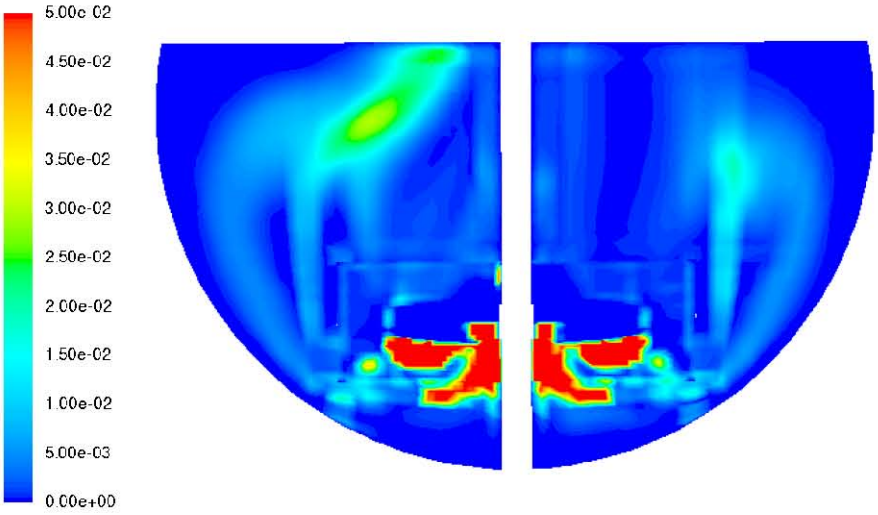

Figure 5.36: k_La with slip penetration model on a vertical plane at 395 rpm

pattern. Similarly, operating at different impeller speeds is not expected to improve the overall distribution since as observed the general flow field is more or less the same at the various impeller speeds investigated.

From Figures 5.35 and 5.36 it can also be seen that qualitatively there are no substantial differences in k_La for the two models used, showing that k_La is more dominated by a than k_L. The relatively low values and poor distribution of k_La in the vessel are expected to have an adverse effect on the efficiency of leaching processes, where k_La can be rate-limiting.

5.3.3 Effect of Impeller Speed on Mass Transfer

Gas-liquid mass transfer coefficient k_La is expected to increase with an increase in impeller speed. The latter results in smaller bubbles and consequently a larger a. The results for the effect of impeller speed on volumetric mass transfer coefficient, k_La, for a water-oxygen system are presented in Figure 5.37. It can be seen that k_La increases with increasing impeller speeds, with a maximum at 350 rpm and decreases at 395 rpm. This was observed for all gas flow-rates and temperature investigated. This also follows a similar trend to the one observed with effect of impeller speed on the Sauter mean diameter, as presented in Section 5.2.3. That is an initial decrease in bubble size followed by an increase at the higher impeller speed.

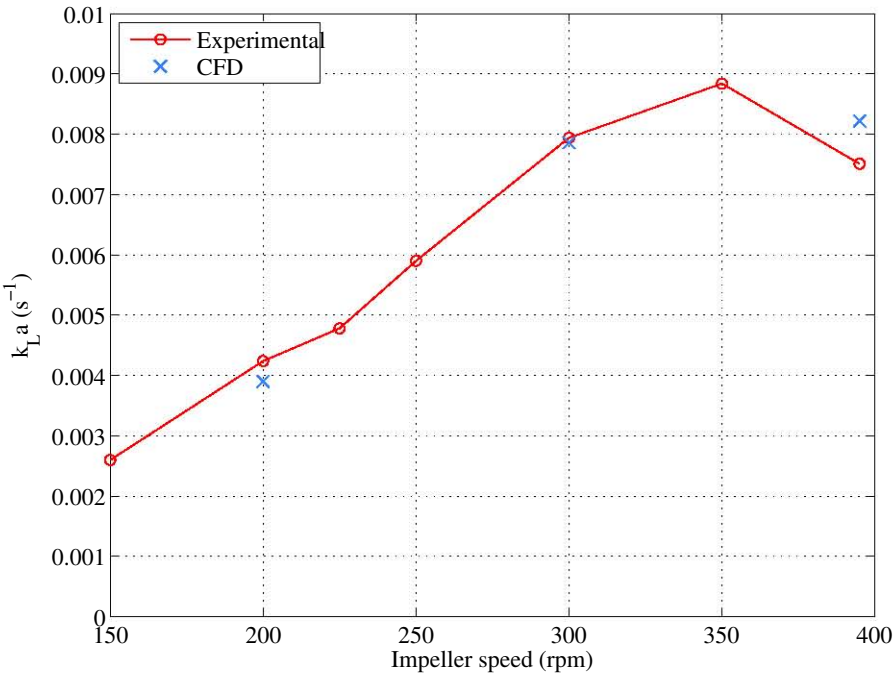

Figure 5.37: Effect of impeller speed on mass transfer - CFD and Experimental

5.3.4 Effect of Gas Flow-rate on Mass Transfer

Gas-liquid mass transfer coefficient, $k_L a$, is known to be affected by various factors. Theses mainly affect the mass transfer coefficient, k_L, and the inter-facial area per unit volume, a. Mass transfer coefficient is affected by the diffusion coefficient as well as the liquid film surrounding the bubble. Bubble size and gas hold-up affect a. A decrease in bubble size and/or increase in gas hold-up is expected to give rise to an increase in a. Bubble size and gas hold-up are in turn affected by various factors as outlined in Sections 5.2.3 - 5.2.5.

Figure 5.38 shows the effect of gas flow-rate on $k_L a$. It can be observed that there is a rise in $k_L a$ at the higher gas flow-rate. Since k_L is predominantly affected by the coefficient of diffusion and film thickness, which is not greatly affected by gas flow-rate, the increase in $k_L a$ is therefore mainly a result of the expected increase in gas hold-up at higher aeration rate (Özbek and Gayik, 2001).

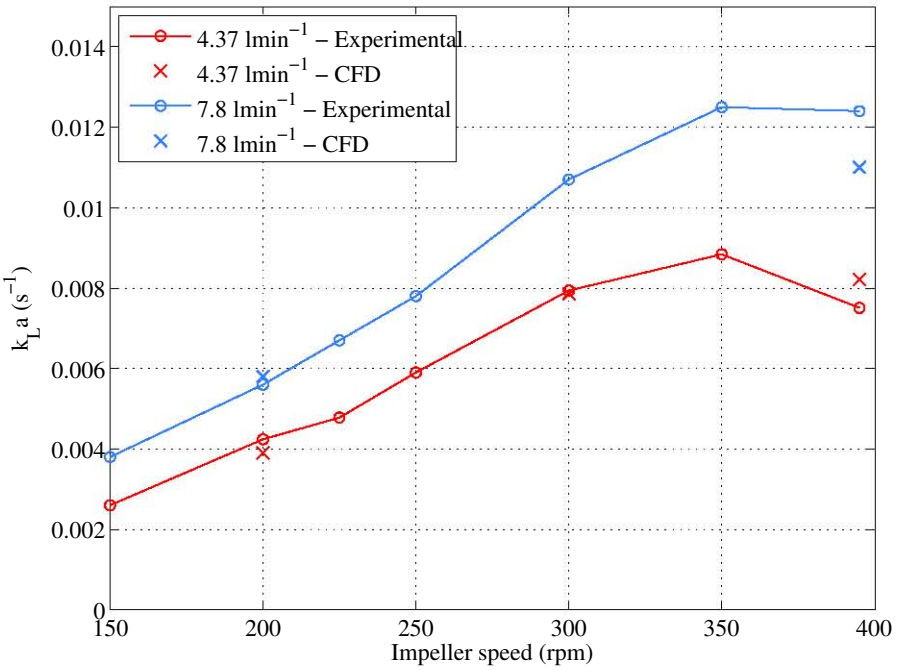

Figure 5.38: Effect of gas flow-rate on mass transfer - CFD and Experimental

5.3.5 Effect of Fluid Properties on Mass Transfer

Temperature is expected to affect both mass transfer coefficient, k_L, and a. The mass transfer coefficient is proportional to the diffusion constant and the latter is dependent on temperature. Therefore, increasing temperature will result in a higher k_L leading to a rise in $k_L a$. Similarly, an increase in temperature is expected to result in a decrease in bubble size as presented in Section 5.2.5.1 and consequently in a larger a.

Figure 5.39 shows the effect of temperature on the gas-liquid mass transfer coefficient over three temperatures; 25, 50 and 70°C. The $k_L a$ values were measured at a gas flow-rate of 4.37 lmin^{-1}. The expected trend is observed, with a rise in $k_L a$ when the temperature is raised, which is a consequence of the increase in k_L and a as explained above. Furthermore, the maximum value of $k_L a$ at 350 rpm is observed at all temperatures.

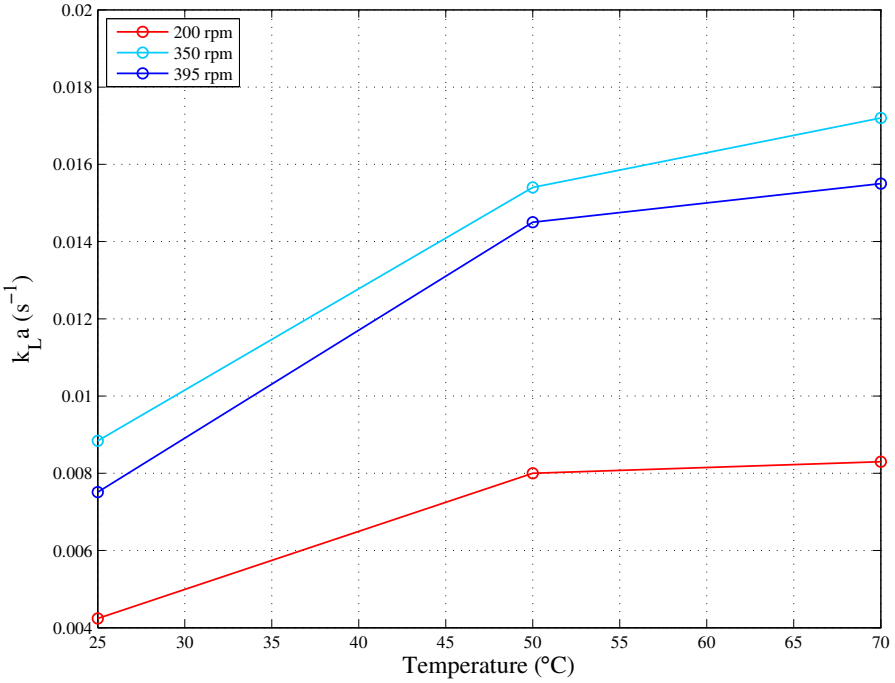

Figure 5.39: Effect of temperature on mass transfer - Experimental

Besides impeller speed, gas flow-rate and temperature gas-liquid mass transfer is known to be affected by electrolytes. From the previous sections, it can be observed that most tests were carried out using water and oxygen, mainly to facilitate PIV and bubble size measurements. Therefore, additional tests were carried out to check if a synthetic leach liquor would result in substantially different $k_L a$ values to the water-oxygen system. The influences of electrolytes is mainly because of the effect ions have on both a and k_L. The latter is expected to decrease with the addition of electrolytes as reported by Kaskiala (2006) and Harnby et al. (1992). The inter-facial area per unit volume is expected to rise to lead to an increase in gas hold-up (Harnby et al., 1992) due to a decrease in bubble size. The drop in bubble size is a result of a decrease in coalescence (Linek et al., 1987).

The accuracy of the $k_L a$ values in the synthetic leach liquor was better at 25°C than at higher temperature. When using the gassing-out dynamic method with a DO probe the solubility of oxygen in the solution is important. Since the solubility in lower in the synthetic leach liquor than in water and even lower at higher temperatures the accuracy of the measurements dropped. To this end, only the $k_L a$ values at 25°C are presented.

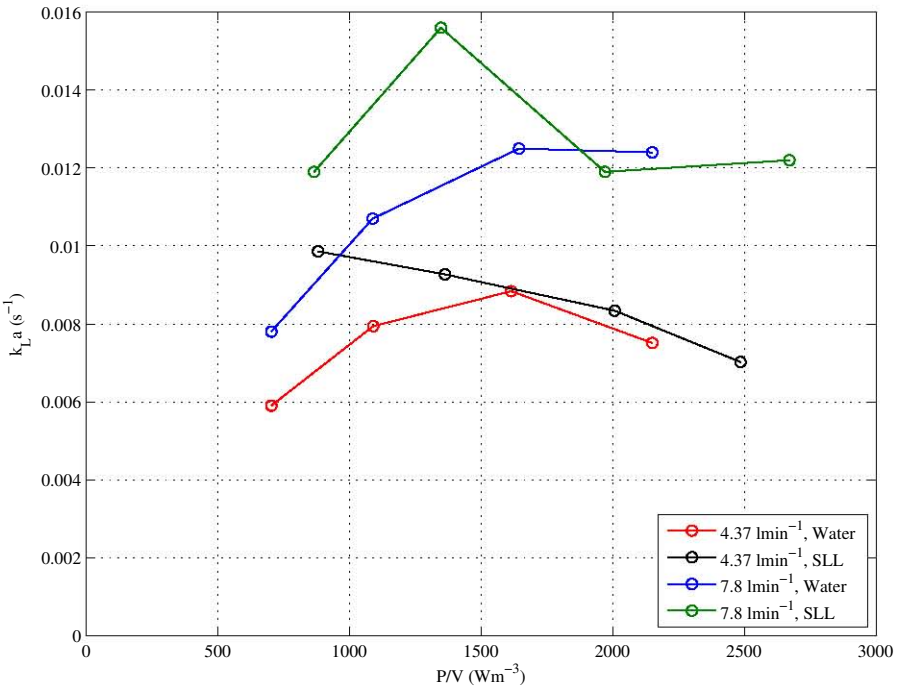

Figure 5.40: Effect of synthetic leach liquor on $k_L a$ at 25°C - Experimental

Figure 5.40 shows the changes in $k_L a$ when using the synthetic leach liquor (SLL) at impeller speeds varying between 250 and 395 rpm at 25°C. It can be observed that $k_L a$ values in the synthetic leach liquor are higher. Since k_L is expected to decrease, the higher $k_L a$ values under acidic conditions can therefore be explained by a larger a. This is most probably due to the smaller bubbles as outlined Section 5.2.5.1 at these impeller speeds. At impeller speeds of 300 and 395 rpm there is a drop in $k_L a$ for the SLL system resulting in a more or less similar $k_L a$ to the water-oxygen system. The decrease in $k_L a$ could be result of the increase in bubble size found in the synthetic leach liquor when impeller speed increases, as described in Section 5.2.5.1.

Even though there are differences in $k_L a$ between the synthetic leach liquor and water, they were not significant, with the order or magnitude being the same. In addition, the small difference observed is not expected to have any influence on the trends discussed in the previous sections.

5.3.6 Empirical Power Law k_La Correlation

One method used to describe mass transfer is by using an empirical power law k_La correlation. There are different variants of the correlation and the most commonly used ones for mixing vessels is given by:

$$k_La = a\,(U_g)^b \left(\frac{P_g}{V_L}\right)^c \tag{5.3}$$

It allows for the contribution of the effect of flow regimes on mass transfer, which is normally ignored, via the gassed power, P_g term (Tatterson, 1991). The correlation is widely used in the design of mixing vessels. However, it has been highlighted that the correlations are dependent on operation conditions and geometry of the vessel used as well the impeller.

Moreover, it can be seen that the expression does not include the effect that temperature would have had on k_La. Therefore, a power law correlation for the pilot-scale autoclave was developed for the water-oxygen with a diffusivity term added to equation 5.3 to account for the influence of temperature and viscosity on k_La. Moreover, two different approaches were used, one based on superficial gas velocity and the other based on the volume flow rate per unit volume. The latter was used since the Q/V term gives a better estimation of k_La when scaling-up (Schlüter and Deckwer, 1992). The two semi-empirical correlations used are given by:

$$k_La = a\,(U_g)^b \left(\frac{P_g}{V_L}\right)^c \left(\frac{D_l}{D_{l@25}}\right)^d \tag{5.4}$$

$$k_La = a \left(\frac{Q}{V_L}\right)^b \left(\frac{P_g}{V_L}\right)^c \left(\frac{D_l}{D_{l@25}}\right)^d \tag{5.5}$$

The correlation was then written into a linear polynomial, as similarly done by Mohamed et al. (2009), by expressing it in a logarithmic form. The latter being equivalent to the general first order response surface model as given below:

$$Y = \beta_0 + \sum \beta_i X_i \tag{5.6}$$

where Y is the estimate response
β_i is the i^{th} coefficient corresponding to X_i
i is the independent variable index
β_0 is the intercept

The constants were calculated by using a multi-linear regression and based on 42 experimental data points. The values for constants (a) and the exponents (b, c, d) are shown in Table 5.5 were obtained by using a linear regression.

Table 5.5: Empirical constants

Equation	a	b	c	d
$5.4^{\#1}$	0.031	0.533	0.406	0.925
$5.5^{\#2}$	0.015	0.533	0.406	0.925

#1 Valid for P_g (W), μ (Pa.s), U_g (ms^{-1}), V (m^3)
#2 Valid for P_g (W), μ (Pa.s), Q_g (ms^{-3}), V (m^3)

The accuracy of the values were assessed based on the coefficient of determination, (R^2), which gives measure of the global fit of the model. The R^2 values for the k_La models were found to be 0.93, meaning that only 7% of the total variations are not explained by the model. Moreover, it can be seen that the exponents are comparable to the ones found in literature, which also shows the importance of adding a diffusivity term to the correlations. In addition, the exponents are comparable to values reported for stirred tanks as seen in literature.

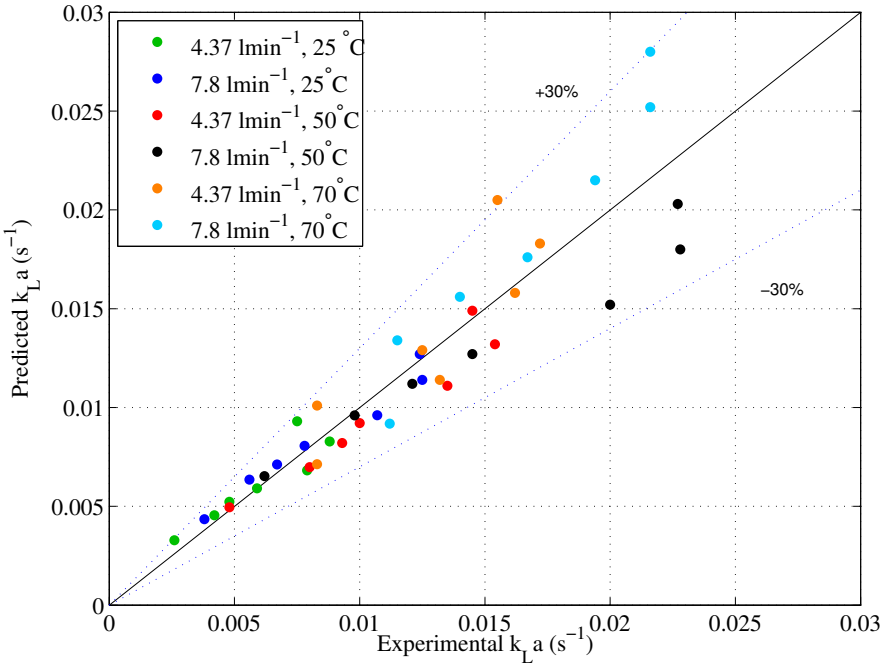

Figure 5.41: Graph of predicted k_La versus experimental k_La for water-oxygen system

Figure 5.41 compares the experimental k_La to the predicted k_La for the water-oxygen system. The models reasonably predicted k_La, showing the effect of power per unit volume, superficial gas velocity, gas flow-rate per unit velocity and temperature on k_La. The errors, which generally varied between 20 and 40% as observed in the previous studies, were below 30 %.

6 Conclusions and Recommendations

The objective of this thesis was to investigate hydrodynamics, gas dispersion and mass transfer in a pilot-scale autoclave. The thesis was initiated to gain a better understanding of mass transfer in autoclaves. But prior to mass transfer, an understanding of the underlying hydrodynamics and gas dispersion is necessary. These flow phenomena were investigated using CFD predictions, which were validated using experimental data. Furthermore, using both CFD predictions and experimental data trends in hydrodynamics, gas dispersion and mass transfer were described.

Initially a single phase CFD model was developed to predict the power draw, velocity flow fields and turbulence parameters over a range of impeller speeds. The models were validated in terms of experimentally measured power draw and velocity flow field. Then a gas-liquid model was developed to predict gas dispersion and mass transfer in the autoclave at various operating conditions. Gas dispersion was characterised in terms of bubble size and gas hold-up. The model was validated with experimentally measured bubble sizes. The two-phase model was further validated against the gas-liquid mass transfer coefficient, k_La, which was also determined from experimental measurements. The conclusions based on the findings are reviewed in Sections 6.1 to 6.3.

6.1 Hydrodynamics

6.1.1 Numerical

The single phase system was used to validate hydrodynamics. It was found that the same numerical methodology used for stirred tanks was appropriate to model fluid flow in the autoclave. The sliding mesh model and the k-ε turbulence model predicted the power draw and velocity flow field accurately. The model was also able to reproduce an atypical flow, for radial impellers, in the impeller region fairly well.

6.1.2 Power Draw

Power number for the Smith turbine used was between 4.1 and 5.6 with the lower numbers at the higher impeller speeds. These power numbers are higher than normally observed values, which vary between 2.8 and 3.2 for stirred tanks. The difference was attributed to

the flow field generated as a result of the geometry and the chosen Smith turbine.

6.1.3 Velocity Flow Field

The flow patterns normally observed in stirred tanks, with a radial impeller, were not reproduced. The jet leaving the impeller was at an angle to the horizontal. An increase in impeller speed had an effect on the angle of inflection of the jet. The unusual flow pattern is due to the geometry of the vessel and the impeller. The double-loop structure, one below and above the impeller, changes to a more or less single-loop structure with the disappearance of the lower loop as impeller speed is increased. The presence of gas had a marginal effect on the velocity flow field.

6.2 Gas Dispersion

6.2.1 Numerical

The gas-liquid system was simulated with the Euler-Euler model and the dispersed k-ε model was used to account for turbulence. It was found that when coupled with the population balance model, which was solved using the discrete method, the Sauter mean diameter was fairly well predicted. Using that approach the Sauter mean diameter was predicted with an average error of 4% and a maximum of 12% at a gas flow-rate of 4.37 lmin^{-1}. At 7.8 lmin^{-1} the predictions had a maximum error of 20%. These were considered acceptable given that they were obtained with no fitted parameters in the fundamental models.

6.2.2 Bubble Size

The local bubble size was found to vary across the autoclave, smaller in the impeller region and larger in the majority of the vessel. The system was mainly controlled by coalescence, with an average bubble size larger than 2 mm, the diameter of the bubbles at the sparger. This is atypical to what is normally observed in stirred tanks, where breakage is more dominant. Coalescence was more pronounced at higher impeller speeds due to the higher agitation rate. Bubble size increased with gas flow-rate but the fluid properties had a small effect on the size. A decrease was noticeable at higher temperature and in the synthetic leach liquor.

6.2.3 Gas Hold-up

The gas distribution was poor, mainly as a result of the flow pattern. Most of the gas was trapped under the impeller blades and disc. There were large regions of the vessel where

there was practically no oxygen. An increase in impeller speed and gas flow-rates led to an increase in gas hold-ups. The gas hold-ups were below 1% for the cases investigated. This is due to the low superficial gas velocities used. The poor gas distribution is not expected to improve at higher superficial velocities as a result of the inherent flow pattern. Increasing impeller speed is not expected to enhance gas dispersion.

6.3 Mass Transfer

6.3.1 Numerical

The CFD model accurately predicted the gas-liquid mass transfer coefficient, k_La. The predictions were more accurate with a full bubble size distribution, which was implemented with the discrete method, and the eddy cell model. The full bubble size distribution was more appropriate as it accounts for bubbles of all sizes. The eddy cell model, which was used to predict k_L, was more suitable than the slip penetration because of the highly agitated and turbulent flow regime in the autoclave.

6.3.2 Gas-liquid Mass Transfer Coefficient

The distribution of the gas-liquid mass transfer coefficient, k_La was mainly controlled by the flow field. The distribution was qualitatively poor, with large regions of practically no mass transfer. The highest values were in the impeller region and most below the impeller blade and disc, where most of the gas was trapped. k_La was found to increase with impeller speed, gas flow-rate and temperature but no major difference was observed in a synthetic leach liquor. k_La will increase in magnitude with increasing superficial gas velocity (or gas flow-rate) but the quality of gas dispersion as well as the distribution of k_La is unlikely to improve.

In conclusion, the methodology to predict hydrodynamics, gas dispersion and mass transfer in an autoclave was presented. The model, validated against experimental data, accurately predicted various fluid flow phenomena. The study has provided a better understanding of hydrodynamics, gas dispersion and mass transfer in an autoclave. The effect of operating conditions such as impeller speed, gas flow rate and fluid properties on the various flow phenomena are better understood. The study also provided the basis to develop better models and more accurate models to analyse full scale autoclaves.

6.4 Recommendations

Various research methodologies were used to develop a satisfactory model to predict hydrodynamics, gas dispersion and mass transfer in an autoclave. This section highlights future work that can be used to improve the models developed.

6.4.1 Hydrodynamics

The hydrodynamics was validated in terms of velocity flow field and power draw. However, the CFD model could be improved by validating the predicted turbulence parameters with experimental data. Therefore, experiments that are able to capture turbulence could be carried out.

6.4.2 Gas Dispersion

The gas-liquid system was validated with experimentally measured Sauter mean diameter and k_La. It would be ideal to validate the model with experimentally measured gas-hold up data. Experiments at higher gas flow-rates, where gas hold-up would be high enough to be measurable, could be performed. Moreover, to improve the prediction of the gas-liquid system, further numerical work could be done on the population balance model with regards to coalescence.

6.4.3 Mass Transfer

The mass transfer study was performed at a range of operating conditions, by varying gas flow-rate, temperature and using a synthetic leach liquor. However, further studies could be carried out at other operating conditions, at higher gas flow-rates and using a slurry. The CFD models, particularly the population balance model, could be improved by taking into account the effect of the change in bubble size due to mass transfer at different operating conditions.

References

R.J. Adrian. Twenty years of particle image velocimetry. *Experiments in Fluids*, 39: 159–169, 2005.

V. Alopaeus, J. Koskinen, and K.I. Keskinen. Simulation of the population balances for liquid-liquid systems in a nonideal stirred tank. Part 1 Description and qualitative validation of the model. *Chemical Engineering Science*, 54:5887–5899, 1999.

S.S. Alves, C.I. Maia, J.M.T. Vasconcelos, and A.J. Serralheiro. Bubble size in aerated tanks. *Chemical Engineering journal*, 89:119–117, 2002.

ANSYS. *Fluent 13*, 2010.

H. Appa. Multiphase CFD modeling of stirred tanks. Master's thesis, University Of Cape Town, 2007.

P.M. Armenante, C. Luo, C. Chou, I. Fort, and J. Medek. Velocity profiles in a closed, unbaffled vessel: comparison between experimental and LDV data and numerical CFD predictions. *Chemical Engineering Science*, 52(20):3483–3492, 1997.

G. Ascanio, B. Castro, and E. Galindo. Measurement of power consumption in stirred vessels - A review. *Chemical Engineering Research and Design*, 82(A9):1282–1290, 2004.

J. Aubin, P. Mavros, D.F. Fletcher, J. Bertrand, and C. Xuereb. Effect of axial agitator configuration (up-pumping, down pumping, reverse rotation) on flow patterns generated in stirred vessels. *Trans IChemE*, 79, Part A:431–445, 2001.

J. Aubin, D.F. Fletcher, and C. Xuereb. Modelling turbulent flow in stirred tanks with CFD: The influence of the modelling approach, turbulence model and numerical scheme. *Experimental Thermal And Fluid Science*, 28:431–445, 2004a.

J. Aubin, N. Le Sauze, J. Bertrand, D.F. Fletcher, and C. Xuereb. PIV measurements of flow in an aerated tank stirred by a down- and an up-pumping axial flow impeller. *Experimental Thermal and Fluids Science*, 28:447–456, 2004b.

F. Azizi and A.M. Al Taweel. Population balance simulation of gas-liquid contacting. *Chemical Engineering Science*, 62:7436–7445, 2007.

A. Bakker. *Hydrodynamics of stirred gas-liquid dispersions.* PhD thesis, Delft University of Technology, The Netherlands, 1992.

A. Bakker and H.E.A. Van Den Akker. A computational model for the gas-liquid flow in stirred reactors. *Institution of Chemical Engineers*, 72, Part A:594–606, 1994.

A. Bakker, K.J. Myers, R.W. Ward, and C.K. Lee. The laminar and turbulent flow pattern of a pitched blade turbine. *Trans IChemE*, 74, Part A:485–491, 1996.

C.W. Bakker. *Numerical modelling of non-Newtonian mineral slurry in a mechanical flotation cell.* PhD thesis, University Of Cape Town, 2009.

B. Basara, A. Alajbegovic, and D. Beader. Simulation of single- and two-phase flows on sliding unstructured meshes using finite volume method. *International Journal for Numerical Methods in Fluids*, 45:1137–1159, 2004.

K.J. Bittorf and S.M. Kresta. Active volume of mean circulation for stirred tanks agitated with axial impellers. *Chemical Engineering Science*, 55:1325–1335, 2000.

M. Blažej, M. Juraščík, J. Annus, and J. Markoš. Measurement of mass transfer coefficient in an airlift reactor with internal loop using coalescent and non-coalescent liquid media. *Journal of Chemical Technology and Biotechnology*, 79:1405–1411, 2004.

A. Brucato, M. Ciofalo, F. Grisafi, and G. Micale. Numerical prediction of flow fields in baffled stirred vessels: A comparison of alternative modelling approaches. *Chemical Engineering Science*, 53(21):3653–3684, 1998a.

A. Brucato, F. Grisafi, and G. Montante. Particle drag coefficients in turbulent fluids. *Chemical Engineering Science*, 53(18):3295–3314, 1998b.

A. Buffo, M. Vanni, and D.L. Marchisio. Multidimensional population balance model for the simulation of turbulent gasâĂŞliquid systems in stirred tank reactors. *Chemical Engineering Science*, 70:31–44, 2012.

M. Ciofalo, A. Brucato, F. Grisafi, and N. Torraca. Turbulent flow in closed and free-surface unbaffled tanks stirred by radial impellers. *Chemical Engineering Science*, 15 (14):3557–3573, 1996.

F.K. Crundwell. Progress in the mathematical modelling of leaching reactors. *Hydrometallurgy*, 39:321–335, 1995.

E.L. Cussler. *Diffusion, Mass transfer in fluid systems,* 2^{nd} *edition.* Cambridge University Press, 1997.

P.V. Danckwerts. Significance of liquid-film coefficients in gas absorption. *Ind Eng Chem*, 43:1460–1467, 1951.

N.G. Deen, T. Solberg, and B.H. Hjertager. Flow generated by an aerated Rushton impeller: Two-phase PIV experiments and numerical simulations. *The Canadian Journal of Chemical Engineering*, 80:638–652, 2002.

D.A. Deglon. *A hydrodynamic investigation of fine particle flotation in a batch flotation cell.* PhD thesis, University Of Cape Town, 1998.

D.A. Deglon and C.J Meyer. CFD modelling of stirred tanks: Numerical considerations. *Minerals Engineering*, 19:1059–1068, 2006.

D.A. Deglon, C.T. O'connor, and A.B. Pandit. Efficiency of a spinning disc as a bubble break-up device. *Chemical Engineering Science*, 53(1):59–70, 1998.

A. Delafosse, A. Line, J. Morchain, and P. Guiraud. LES and URANS simulations of hydrodynamics in mixing tank: Comparison to PIV experiments. *Chemical Engineering Research and Design*, 86:1322–1330, 2008.

J. Derksen and H.E.A. van Den Akker. Large eddy simulations on the flow driven by Rushton turbine. *AIChE*, 45(2):209–221, 1999.

K.M. Dhanasekharan, J. Sanyal, A. Jain, and A. Haidari. A generalized approach to model oxygen transfer in biorectors using population balances and computational fluid dynamics. *Chemical Engineering Science*, 60:213–218, 2005.

H. Dhaouadi, S. Poncin, J.M. Hornut, and N. Midoux. Gas-liquid mass transfer in bubble column reactor: Analytical solution and experimental confirmation. *Chemical Engineering and Processing*, 47:448–556, 2008.

G.S. Dobby and F.S. Finch. Particle collection in columns - Gas rate and bubble size effects. *Canadian Metallurgical Quarterly*, 25(1):9–13, 1986.

D.F. Engelbrecht. Development of a CFD model for stirred tank applications. Master's thesis, University Of Cape Town, 2006.

M.D. Fokema, S.M. Kresta, and P.E. Wood. Importance of using the correct impeller boundary conditions for CFD simulations of stirred tanks. *Canadian Journal of Chemical Engineering*, 72:177–183, 1994.

C. Galletti, S. Pintus, and E. Brunazzi. Effect of shaft eccentricity and impeller blade thickness on the vortices features in an unbaffled vessel. *Chemical Engineering Research and Design*, 87(4):391–400, 2009.

C. Gentric, D. Mignon, J. Bousquet, and P.A. Tanguy. Comparison of mixing in two gas-liquid reactors using CFD simulations. *Chemical Engineering Science*, 60:2253–2272, 2005.

D. Georgiou and V.G. Papangelakis. Characterization of limonitic laterite and solids during sulfuric acid pressure leaching using transmission electron microscopy. *Minerals Engineering*, 17:461–463, 2004.

J. Gimbun, C.D. Rielly, and Z.K. Nagy. Modelling of mass transfer in gas-liquid stirred tanks agitated by Rushton turbine and CD-6 impeller: A scale-up study. *Chemical Engineering Research and Design*, 87:437–451, 2009.

B.K. Gorain, J.-P. Franzidis, and E.V. Manlapig. Studies on impeller type, impeller speed and air flow rate in an industrial scale flotation cell- Part 1 : Effect on bubble size distribution. *Minerals Engineering*, 8(6):615–635, 1995.

A.D. Gosman, C. Lekakou, S. Politis, R.I. Issa, and M.K. Looney. Multidimensional modeling of turbulent two-phase flows in stirred vessels. *AIChE*, 38(12):1946–1956, 1992.

R.A. Grau and K. Heiskanen. Visual technique for measuring bubble size in flotation machines. *Minerals Engineering*, 15:507–513, 2002.

M. Greaves and M. Barigou. Estimation of gas hold-up and impeller power in a stirred vessel reactor. *Chem. Eng. Symp. Ser.*, 108:235–255, 1988.

M. Greaves and M. Barigou. Bubble size distributions in a mechanically agitated gas-liquid contactor. *Chemical Engineering Science*, 47(8):2009–2025, 1992.

S. Guet, S. Luther, and G. Ooms. Bubble shape and orientation determination with a four-point optical fibre probe. *Experimental Thermal and Fluid Science*, 29:803–812, 2005.

N. Harnby, M.F. Edwards, and A.W. Nienow. *Mixing in the Process Industries*. Oxford: Butterworth-Heinemann, 1992.

H. Hartmann, J.J. Derksen, C. Montavon, J. Pearson, I.S. Hamill, and H.E.A. van den Akker. Assessment of large eddy and RANS stirred tank simulation by mean of LDA. *Chemical Engineering Science*, 59:2419–2432, 2004.

P.S. Harvey and M. Greaves. Turbulent flow in agitated vessel. *Trans. IChemE*, 60: 195–210, 1982.

I.T.M. Hassan and C.W. Robinson. Stirred-tank mechanical power requirement and gas holdup in aerated aqueous phases. *AIChE*, 23(1):48–56, 1977.

J.R. Hernandez-Aguilar, R.G. Coleman, C.O. Gomez, and J.A. Finch. A comparison between capillary and imaging techniques for sizing bubbles in flotation systems. *Minerals Engineering*, 17:53–61, 2004.

R. Higbie. The rate of absorbtion of a pure gas into a still liquid during short periods of exposure. *Transactions of the American Institute of Chemical Engineers*, 31:365–389, 1935.

D.M Himmelblau and K.B Bischoff. *Process analysis and simulation: Deterministic Systems.* John Wiley and Sons, Inc., New York, 1968.

J.O. Hinze. Fundamentals of the hydrodynamic mechanism of splitting in dispersion processes. *AIChE Journal*, 3(1):289–295, 1955.

Y. Hu, W. Wang, T. Shao, J. Yang, and Yi Cheng. Visualization of reactive and non-reactive mixing processes in a stirred tank using planar laser induced fluorescence (PLIF) technique. *Chemical Engineering Research and Design*, 90:524–533, 2012.

H.M. Hulburt and S. Katz. Some problems in particle technology. a statistical mechanical formulation. *Chemical Engineering Science*, 19:555–574, 1964.

M. Ishii and N. Zuber. Drag coefficient and relative velocity in bubbly, droplet or particulate flows. *AIChE*, 25(5):843–855, 1979.

H.A. Jakobsen. *Chemical Reactor Modeling: Multiphase Reactive Flows.* Springer, 2008.

K.H. Javed, T. Mahmud, and J.M. Zhu. Numerical simulation of turbulent batch mixing in a vessel agitated by a Rushton turbine. *Chemical Engineering and Processing*, 45: 99–112, 2006.

Z. Jaworski and B. Zakrzewska. Modelling of the turbulent wall jet generated by a pitched blade turbine impeller: The effect of turbulence model. *Transactions of the Institution of Chemical Engineers*, 80 Part A:846–854, 2002.

T. Kaskiala. *Studies on gas-liquid mass transfer in atmospheric leaching of sulphidic zinc concentrates.* PhD thesis, Helsinky University Of Technology, 2006.

Y. Kawase and M. Moo-Young. Mathematical models for the design of bioreactors: application of kolmogoroff's theory of isotropic turbulence. *Chemical Engineering Journal*, 43:B19–B41, 1990.

F. Kerdouss, A. Bannari, and P. Proulx. CFD modeling of gas dispersion and bubble size in a double turbine stirred tank. *Chemical Engineering Science*, 61:3313–3322, 2006.

F. Kerdouss, A. Bannari, P. Proulx, R. Bannari, M. Skrga, and Y.Labreque. Two-phase mass transfer coefficient prediction in stirred vessel with a CFD model. *Computers & Chemical Engineering*, 32:1943–1955, 2008.

A.R. Khopkar and V.V. Ranade. CFD simulation of gas-liquid stirred vessel: VC, S33, and L33 flow regimes. *AIChE Journal*, 52(5):2215–2229, 2006.

A.R. Khopkar, J. Aubin, C. Xuereb, N. Le Sauze, J. Bertrand, and V.V. Ranade. Gas-liquid flow generated by a pitched-blade turbine: Particle image velocimetry measurements and computational fluid dynamics simulations. *Industrial and Engineering Chemistry and Research*, 42:5318–5332, 2003.

A.R. Khopkar, A.R. Ramnohan, V.V. Ranade, and M.P. Dudukovic. Gas-liquid flow generated by a Rushton turbine in stirred vessel:CARPT/CT measurements and CFD simulations. *Chemical Engineering Science*, 60:2215–2229, 2005.

R. Klepper. Optimising gas mass transfer in autoclaves. *The minerals, metals & materials society*, pages 549–559, 2000.

P.T.L. Koh and F. Xantidis. CFD modelling in the scale-up of a stirred reactor for the production of resin beads. *Second International Conference on CFD in the Minerals and Process Industries*, pages 369–374, 1999.

A.A. Kulkarni. Mass transfer in bubble column reactors: Effect of bubble size distribution. *Industrial and Engineering Chemistry Research*, 46:2205–2211, 2007.

A.A. Kulkarni and J.B. Joshi. Simultaneous measurement of flow pattern and mass transfer coefficient in bubble columns. *Chemical Engineering Journal*, 59:271–281, 2004.

M. Laakkonen. *Development and validation of mass transfer models for the design of agitated gas-liquid reactors*. PhD thesis, Helsinky University Of Technology, 2006.

M. Laakkonen, P. Moilanen, T. Miettinen, K. Saari, M. Honkanen, P. Saarerinne, and J. Aittamaa. Local bubble size distributions in agitated vessel: Comparison of three experimental techniques. *Chemical Engineering Research and Design*, 83(A1):50–58, 2005.

M. Laakkonen, V. Alopaeus, and J. Aittamaa. Validation of bubble breakage, coalescence and mass transfer models for gas-liquid dispersion in agitated vessel. *Chemical Engineering Science*, 61:218–228, 2006a.

M. Laakkonen, P. Moilanen, V. Alopaeus, and J. Aittamaa. Dynamic modeling of local reaction conditions in an agitated aerobic fermenter. *AIChE*, 52(5):1673–1689, 2006b.

M. Laakkonen, V. Alopaeus, and J. Aittamaa. Modelling local bubble size distributions in agitated vessels. *Chemical Engineering Science*, 62:721–740, 2007.

J.C. Lamont and D.S Scott. An eddy cell model of mass transfer into the surface of a turbulent liquid. *AIChE*, 16:513–519, 1970.

R.M. Lamya. *A fundamental evaluation of the atmospheric pre-leaching section of the nickel-copper matte treatment process.* PhD thesis, University of Stellenbosch, 2007.

G.L. Lane, M.P. Schwarz, and G.M Evans. Predicting gas-liquid flow in a mechanically stirred tank. *Applied Mathematical Modelling*, 26:223–235, 2002.

B.E. Launder and D.B Spalding. The numerical computation of turbulent flows. *Computer Methods in Applied Mechanics and Engineering*, 3(1974):269–289, 1974.

K.C. Lee and M. Yianneskis. The extent of periodicity of the flow in vessels stirred by Rushton impellers. *AIChE Symp Series*, 90:5–18, 1994.

F. Lehr, M. Millies, and D. Mewes. Bubble-size distributions and flow fields in bubble columns. *Fluid Mechanics and Transport Phenomena*, 48(11):2426–2240, 2002.

V. Linek, V. Vacek, and P. Beneš. A critical review and experimental verification of the correct use of the dynamic method for the determination of oxygen transfer in aerated agitated vessels to water, electrolyte solutions and viscous liquids. *The Chemical Engineering Journal*, 34:11–34, 1987.

V. Linek, M. Kordač, M. Fujasoá, and T. Moucha. Gas-liquid mass transfer coefficient in stirred tanks interpreted through models of idealized eddy structure of turbulence in the bubble vicinity. *Chemical Engineering and Processing*, 43:1511–1517, 2004.

J.D. Lister, D.J. Smit, and M.J. Hounslow. Adjustable discretized population balance for growth and aggregation. *AIChE*, 41(3):591–603, 1995.

H. Luo. *Coalescence, Breakup and Liquid Circulation in Bubble Column Reactors.* PhD thesis, The University of Trondheim, 1993.

H. Luo and H.F. Svendsen. Theoretical model for drop and bubble breakup in turbulent dispersions. *AIChE*, 1(5):1225–1233, 1996.

J.Y. Luo, A.D Gosman, R.I. Issa, J.C. Middleton, and M.K. Fitzgerald. Full flow field computation of mixing in baffled stirred vessels. *Transactions of the Institution of Chemical Engineers*, 71:342–344, 1993.

D.L. Marchisio, R.D. Vigil, and R.O. Fox. Quadrature method of moments for aggregation-breakage process. *Journal of Colloid and Interface Science*, 258:322–334, 2003.

P. Mavros. Flow visualisation in stirred vessels: A review of experimental techniques. *Transactions of the Institution of Chemical Engineers*, 79, Part A:113–127, 2001.

R. McGraw. Description of aerosol dynamics by the quadrature method of moments. *Aerosol Science and Technology*, 27:255–265, 1997.

METSOC. Schematic of a horizontal acid leach autoclave, October 2011. URL `http://www.metsoc.org/virtualtour/processes/acid-leech/autoclave.asp`.

J.C. Middelton, F. Pierce, and P.M. Lynch. Computation of flow flow fields and complex reaction yield in turbulent stirred reactors and comparison with experimental data. *Chem. Eng. Res. Des*, 64:18–22, 1986.

M.S. Mohamed, R. Mohamad, R.N. Ramanan, M.A. Manan, and A.B Ariff. Modelling of oxygen transfer correlations for stirred tank bioreactor agitated with atypical helical ribbon impeller. *American Journal of Applied Sciences*, 6(5):848–856, 2009.

P. Moilanen, M. Laakkonen, O. Visuri, V. Alopeus, and J. Aittamaa. Modelling mass transfer in an aerated 0.2 m^3 vessel agitated by Rushton, Phasejet and Combijet impellers. *Chemical Engineering Journal*, 142:95–108, 2008.

G. Montante, K.C. Lee, A. Brucato, and M. Yianneskis. Experiments and predictions of the transitions of the flow pattern with impeller clearance in stirred tanks. *Computers and Chemical Engineering*, 25:729–735, 2001.

G. Montante, D. Horn, and A. Paglianti. Gas-liquid flow and bubble size distribution in stirred tanks. *Chemical Engineering Science*, 63:2107–2118, 2008.

M. Moo-Young and H.W Blanch. Design of biochemical reactors: Mass transfer criteria for simple and complex systems. *Advances in Biochemical Engineering*, 19:1–69, 1981.

K.E. Morud and B.H. Hjertager. LDA measurements and CFD modeling of gas-liquid flow in stirred tanks. *Chemical Engineering Science*, 51:233–249, 1996.

R. Newell. *Hydrodynamics and Scale-up in Rushton turbine flotation cells*. PhD thesis, University of South Australia, 2006.

K. Ng, N.J Fentiman, K.C. Lee, and M. Yianneskis. Assessment of sliding mesh CFD predictions and LDA measurements of the flow in a tank stirred by a Rushton impeller. *Transactions of the Institution of Chemical Engineers*, 76:737–747, 1998.

M. Nicolle, G. Nel, T. Plikas, U. Shah, L. Zunti, M.Bellino, and H.J.H. Pieterse. Mixing system design for the tati activox® autoclave. *The Journal of The Southern African Institute of Mining and Metallurgy*, 109:357–364, 2009.

A.W. Nienow. Suspension of solid particles in turbine agitated baffled vessels. *Chemical Engineering Science*, 23:1453–1459, 1968.

C.T O'Connor, E.W. Randall, and Gondall C.M. Measurement of the effects of physical and chemical variables on bubble size. *Int. J. Miner. Process*, 28:139–149, 1989.

K. Okamoto, S. Nishio, T. Saga, and T. Kobayashi. Standard images for particle-image velocimetry. *Measurement Science and Technology*, 11:685–691, 2000.

B. Özbek and S. Gayik. The studies on the mass transfer coefficient in a bioreactor. *Process Biochemistry*, 36:729–741, 2001.

A.W. Pacek and A.W. Nienow. Measurement of drop size distribution in concentrated liquid-liquid dispersions: Video and capillary technique. *Chemical Engineering Research and Design*, 73(5):512–518, 1995.

E.L Paul, V.A. Atiemo-Obeng, and S.M. Kresta. *Handbook of Industrial Mixing: Science and Practice*. Wiley Interscience, 2003.

C.Y. Perng and J.Y. Murthy. A moving-deforming mesh technique for simulation of flow in mixing tanks. *AIChE. Symp. Ser.*, 89(293):37–41, 1993.

J. Petersen. *Introduction to hydrometallurgy and hydrometallurgical operations at Anglo Platinum*, 2007. Short Course 16-18 April 2007.

M. Petitti, A. Nasuti1, D.L. Marchisio, M. Vanni, G. Baldi1, N. Mancini, and F. Podenzani. Bubble size distribution modeling in stirred gas-liquid reactors with QMOM augmented by a new correction algorithm. *AIChE Journal*, 56(1):36–53, 2010.

N. Qi, H. Zhang, K. Zhang, G. Xu, and Y. Yang. CFD simulation of particle suspension in a stirred tank. *Particuology*, 2012.

D. Ramakrishna. *Population Balances: Theory and Applications to Particulate Systems in Engineering*. Academic Press, 2000.

V.V. Ranade. An efficient computational model for simulating flow in stirred vessels: A case of Rushton turbine. *Chemical Engineering Science*, 52(24):4473–4484, 1997.

V.V. Ranade and V.R Deshpande. Gas-liquid flow in stirred reactors: Trailing vortices and gas accumulation behind impeller blades. *Chemical Engineering Science*, 54:2305–2315, 1999.

V.V. Ranade and H.E.A. Van Den Akker. A computational snapshot of gas-liquid flow in baffled stirred reactors. *Chemical Engineering Science*, 49(24B):5175–5192, 1994.

V.V. Ranade, J.B. Joshi, and A.G. Marathe. Flow generated by pitched blade turbines II: Simulation using the k-ε model. *Chemical Engineering Communications*, 81:225–248, 1989.

V.V. Ranade, M. Perrard, N. Le Sauze, C. Xuereb, and J. Bertrand. Trailing vortices of Rushton turbine: PIV measurement and CFD simulations with snapshot approach. *Trans IChemE*, 79, Part A:3–12, 2001a.

V.V. Ranade, M. Perrard, C. Xuereb, and N. Le Sauzeand J. Bertrand. Influence of gas flow rate on the structure of trailing vortices of a Rushton turbine: PIV measurements and CFD simulations. *Trans IChemE*, 79, Part A:957–964, 2001b.

E.W. Randall, C.M. Goodall, P.M. Fairlamb, P.L. Dold, and C.T O'Connor. A method for measuring the sizes of bubbles in two- and three-phase system. *Journal of Physics E: Scientific Instruments*, 22:827–833, 1989.

A.D. Randolph and M.R. Larson. *Theory of Particulate Processes: Analysis and Techniques of Continuous Crystallization.* Academic Press, Inc, 1988.

C.P. Ribeiro-Jr and D. Mewes. On the effect of liquid upon bubble coalescence. *Chemical Engineering Science*, 61:5704–5716, 2006.

K. Van Riet and J.M. Smith. The behaviour of gas-liquid mixtures near Rushton turbine blades. *Chemical Engineering Science*, 28:1031–1037, 1973.

J.O. Roux, M. Du Toit, and D. Shklaz. Novel redesign of a pressure leach autoclave by a south african platinum producer. *The Southern African Institute of Mining and Metallurgy, Base Metals Conference 2009*, 2009.

S. Roy, S. Acharya, and M.D. Cloeter. Flow structure and the effect of macro-instabilities in a pitched-blade stirred tank. *Chemical Engineering Science*, 65:3009âĂŞ3024, 2010.

J.H. Rushton, E.W. Costich, and H.J. Everett. Power characteristics of mixing impellers, part 1. *Chemical Engineering Progress*, 46(8):395–404, 1994.

K. Rutherford, S.M. Mahmoudi, K.S. Lee, and M. Yianneskis. The influence of Rushton impeller blade and disc thickness on the mixing characteristics of stirred vessels. *Trans IChemE*, 74:369–378, 1996.

F. Scargiali, A. D'Orazio, F. Grisafi, and A. Brucato. Modelling and simulation of gas-liquid hydrodynamics in mechanically stirred tanks. *Chemical Engineering Research and Design*, 85:637–646, 2007.

L. Schiller and A. Naumann. A drag coefficient correlation. *VDI Zeits*, 77:318–320, 1933.

V. Schlüter and W.D. Deckwer. Gas-liquid mass transfer in stirred vessels. *Chemical Engineering Science*, 47(9):2357–2362, 1992.

B. Selma, R. Bannari, and P.Proulx. Simulation of bubbly flows: Comparison between direct quadrature method of moments (DQMOM) and method of classes (CM). *Chemical Engineering Science*, 65:1925–1941, 2010.

M. Shäfer, M. Höfken, and F.Durst. Detailed LDV measurement for visualisation of the flow field with a stirred-tank reactor equipped with a Rushton turbine. *Institution of Chemical Engineers*, 75 Part A:729–736, 1997.

R. Shaper, A. B. De Haan, and J.M. Smith. Temperature effects on the gas hold-ups in agitated vessels. *Institution of Chemical Engineers*, 80 Part A:887–892, 2002.

J. Sheng, H. Meng, and R.O. Fox. Validation of CFD simulations of a stirred tank using particle image velocimetry data. *The Canadian Journal of Chemical Engineering*, 76: 611–625, 1998.

H. Singh, D.F. Fletcher, and J.J. Nijdam. An assessment of different turbulence models for predicting flow in a baffled tank stirred with a Rushton turbine. *Chemical Engineering Science*, 66(23):5976–5988, 2011.

P. Spicka, M.M. Dias, and J.C.B. Lopes. Gas-liquid flow in 2D column: Comparison between experimental data and CFD modelling. *Chemical Engineering Science*, 56: 6367–6383, 2001.

H. Sun, Z. Mao, and G. Yu. Experimental and numerical study of gas hold-up in surface aerated stirred tanks. *Chemical Engineering Science*, 61:4098–4110, 2006.

F.J.E Svensson and A. Rasmuson. PIV measurements in a liquid-liquid system at volume percentages up to 10% dispersed phase. *Exp Fluids*, 41:917–931, 2006.

C. Tang and T.J. Heindel. Estimating gas holdup via pressure difference measurements in a cocurrent bubble column. *International journal of Multiphase Flow*, 32:850–863, 2006.

G.B. Tatterson. *Fluid mixing and gas dispersion in agitated tanks.* McGraw Hill, Inc., 1991.

J.J. Taute. *Anglo Platinum bubble sizer user manual*, 2006. Divisional Metallurgical Laboratory, February 2006.

K. Terasaka, D. Hullmann, and A. Schumpe. Mass transfer in bubble columns stuided with an oxygen optode. *Chemical Engineering Science*, 53(17):3181–3184, 2008.

R.E. Treybal. *Mass-transfer operations.* McGraw-Hill Book Company, 1968.

K. van't Riet. Review of measuring methods and results in mass transfer in stirred vessels. *Ind. Eng. Chem. Process Des. Dev.*, 18(3):357–364, 1979.

J.M.T. Vasconcelos, S.C.P. Orvalho, A.M. RodriTguez, and S.S Alves. Effect of blade shape on the performance of six blade disk turbine impellers. *Industrial Engineering Chem. Research*, 39:203–208, 2000.

H.K Versteeg and W Malalasekera. *An Introduction to Computational Fluid Dynamics.* Pearson Prentice Hall, 1995.

G.B. Wallis. *One-dimensional two-phase flow.* McGraw-Hill Book Company, New York, 1969.

T. Wang and J. Wang. Numerical simulations of gas-liquid mass transfer in bubble columns with a CFD-PBM coupled model. *Chemical Engineering Science*, 62:7107–7118, 2007.

K. Wechsler, M. Breuer, and F. Durst. Steady and unsteady computations of turbulent flows induced by a 4/45° pitched-blade impeller. *Journal of Fluid Engineering*, 121: 318–329, 1999.

C.R. Wilke and P. Chang. Correlation of diffusion coefficients in dilute solutions. *AIChE*, 1:264–270, 1955.

K. Yapici, B. Karasozen, M. Schäfer, and Y. Uludag. Numerical investigation of the effect of the Rushton type turbine design factors on agitated tank flow characteristics. *Chemical Engineering and Processing: Process Intensification*, 47:1340–1349, 2008.

Y. Zhu and J. Wu. Gas/liquid mass transfer in hot sparged systems. *Developments in Chemical Engineering and Mineral Processing*, 12:323–332, 2004.

Y. Zhu, J. Wu, and R. Manasseh. Rapid measurement of bubble size in gas-liquid flows using a bubble detection technique. 14^{th} *Australasian Fluid Mechanics Conference*, pages 541–544, 2001.

N. Zuber and J. A. Findlay. Average volumetric concentration in two-phase flow systems. *J Heat Transfer*, 87:453–468, 1965.

A Hydrodynamics

A.1 Power Input

Table A.1: Power (W) for water at 25°C and synthetic leach liquor (SLL) at 30°C

N (rpm)	4.37 l/min		7.8 l/min	
	Water	SLL	Water	SLL
150	9.86	12.40	9.25	12.02
200	22.09	27.84	23.53	27.74
225	31.20	39.29	31.20	39.76
250	42.25	52.91	42.25	52.01
300	65.49	81.82	65.34	80.90
350	96.90	120.45	98.70	118.29
395	129.04	149.13	129.04	160.28

Table A.2: Power (W) at 50°C water and synthetic leach liquor (SLL)

N (rpm)	4.37 l/min		7.8 l/min	
	Water	SLL	Water	SLL
150	8.32	13.79	7.70	13.79
200	19.42	30.82	19.93	30.20
225	28.89	44.15	29.24	44.73
250	38.52	56.50	39.81	57.14
300	61.64	89.22	62.25	89.22
350	93.48	131.96	93.48	126.02
395	125.79	167.99	125.79	169.01

Table A.3: Power (W) at 70°C water and synthetic leach liquor (SLL)

N (rpm)	4.37 l/min		7.8 l/min	
	Water	SLL	Water	SLL
150	9.71	13.79	8.48	12.17
200	23.22	31.44	21.57	32.05
225	31.20	43.80	31.20	41.14
250	41.86	57.66	41.86	52.91
300	69.34	90.92	69.34	89.22
350	98.88	117.75	102.47	117.75
395	131.88	162.72	131.88	165.76

B Gas Dispersion

B.1 Bubble Size

Table B.1: Bubble size: Flow-rate = 4.37 lmin^{-1}, Temperature = 25 °C

N (rpm)	**Region**	$\mathbf{d}_{max}$ **(mm)**	$\mathbf{d}_{min}$ **(mm)**	$\mathbf{d}_{b}$ **(mm)**	$\mathbf{d}_{32}$ **(mm)**
150	Bulk	5.330	1.001	1.971	2.920
	Impeller	7.251	1.001	1.723	2.906
	Tank	7.251	1.001	1.804	2.911
200	Bulk	4.859	1.001	2.063	2.771
	Impeller	6.583	1.001	1.515	2.361
	Tank	6.583	1.001	1.632	2.495
225	Bulk	6.298	1.001	2.264	3.087
	Impeller	5.994	1.001	1.923	2.574
	Tank	6.298	1.001	2.054	2.816
250	Bulk	5.221	1.001	2.067	2.828
	Impeller	5.196	1.001	1.483	2.129
	Tank	5.221	1.001	1.674	2.470
300	Bulk	5.702	1.003	2.435	2.968
	Impeller	4.778	1.001	1.502	2.082
	Tank	5.702	1.001	1.807	2.568
350	Bulk	7.341	1.001	2.534	3.391
	Impeller	6.818	1.003	2.091	2.791
	Tank	7.341	1.001	2.239	3.048
395	Bulk	5.923	1.001	2.731	3.370
	Impeller	6.153	1.001	1.792	2.773
	Tank	6.153	1.001	2.152	3.110

Table B.2: Bubble size: Flow-rate = 7.8 lmin^{-1}, Temperature = 25°C

N (rpm)	**Region**	$\mathbf{d}_{max}$ **(mm)**	$\mathbf{d}_{min}$ **(mm)**	$\mathbf{d}_b$ **(mm)**	$\mathbf{d}_{32}$ **(mm)**
150	Bulk	6.429	1.001	2.278	3.150
	Impeller	6.777	1.001	2.598	3.094
	Tank	6.777	1.001	2.495	3.110
200	Bulk	6.974	1.003	2.297	3.088
	Impeller	6.513	1.001	2.337	2.927
	Tank	6.974	1.001	2.323	2.985
225	Bulk	7.532	1.001	2.371	3.274
	Impeller	7.386	1.003	2.230	2.840
	Tank	7.532	1.001	2.292	3.050
250	Bulk	7.914	1.001	2.108	2.996
	Impeller	5.947	1.001	2.271	2.935
	Tank	7.914	1.001	2.207	2.958
300	Bulk	8.613	1.003	2.415	3.435
	Impeller	6.531	1.003	2.179	2.759
	Tank	8.613	1.003	2.260	3.035
350	Bulk	8.073	1.003	2.688	3.500
	Impeller	5.895	1.003	2.177	2.874
	Tank	8.073	1.003	2.411	3.226
395	Bulk	12.459	1.007	2.892	3.917
	Impeller	8.096	1.001	2.351	3.114
	Tank	12.459	1.001	2.515	3.432

Table B.3: Bubble size: Flow-rate = 7.8 lmin^{-1}, Temperature = 25°C, SLL, Bulk region

N (rpm)	$\mathbf{d}_{max}$ **(mm)**	$\mathbf{d}_{min}$ **(mm)**	$\mathbf{d}_{b}$ **(mm)**	$\mathbf{d}_{32}$ **(mm)**
150	5.273	1.001	1.752	2.469
200	6.228	1.001	1.842	2.527
225	5.570	1.001	1.972	2.641
250	7.244	1.001	2.210	2.806
300	5.794	1.001	2.232	2.779
350	6.612	1.001	2.472	2.984
395	5.260	1.003	2.477	3.091

C Mass Transfer

C.1 Gas-liquid Mass Transfer, k_La

Table C.1: k_La (s^{-1}) at different points in vessel

Position	1	2	3	4	5
$\boldsymbol{k_La}$	0.00417	0.00424	0.00427	0.00421	0.00417

Table C.2: k_La (s^{-1}) for water

N	**25°C**		**50°C**		**70°C**	
(rpm)	**4.37 l/min**	**7.8 l/min**	**4.37 l/min**	**7.8 l/min**	**4.37 l/min**	**7.8 l/min**
150	0.00260	0.0038	0.0048	0.0062	0.0083	0.0112
200	0.00424	0.0056	0.0080	0.0098	0.0083	0.0115
225	0.00478	0.0067	0.0093	0.0121	0.0132	0.0140
250	0.00590	0.0078	0.0100	0.0145	0.0125	0.0167
300	0.00794	0.0107	0.0135	0.0200	0.0162	0.0194
350	0.00884	0.0125	0.0154	0.0228	0.0172	0.0216
395	0.00751	0.0124	0.0145	0.0227	0.0155	0.0216

Table C.3: k_La (s^{-1}) for synthetic leach liquor (SLL) at 25°C

N (rpm)	**4.37 l/min**	**7.8 l/min**
250	0.00986	0.0119
300	0.00927	0.0156
350	0.00834	0.0119
395	0.00702	0.0122